

# CLAS12 Forward Tagger (FT) Technical Design Report

The CLAS12 Collaboration

# Participating Institutions

CEA-Saclay, Gif-sur-Yvette, France

Istituto Nazionale di Fisica Nucleare - Sezione di Genova, Genova, Italy

Istituto Nazionale di Fisica Nucleare - Sezione di Tor Vergata, Roma, Italy

James Madison University, Athens, OH

Norfolk State University, Norfolk, VA

Ohio University, Athens, OH

Thomas Jefferson National Accelerator Facility, Newport News, VA

University of Edinburgh, Edinburgh, UK

University of Glasgow, Glasgow, UK

# Editors

M. Battaglieri, INFN-GE, email: [battaglieri@ge.infn.it](mailto:battaglieri@ge.infn.it)

R. De Vita, INFN-GE, email: [devita@ge.infn.it](mailto:devita@ge.infn.it)

D. Watts, U. Edinburgh, email: [daniel.watts@ph.ed.ac.uk](mailto:daniel.watts@ph.ed.ac.uk)

D. Glazier, U. Edinburgh, email: [dglazier@ph.ed.ac.uk](mailto:dglazier@ph.ed.ac.uk)

K. Hicks, Ohio U., email: [hicks@ohio.edu](mailto:hicks@ohio.edu)

S. Procureur, CEA, email: [sebastien.procureur@cea.fr](mailto:sebastien.procureur@cea.fr)

F. Sabatié, CEA, email: [franck.sabatie@cea.fr](mailto:franck.sabatie@cea.fr)

C. Salgado, NSU, email: [salgado@jlab.org](mailto:salgado@jlab.org)

S. Stepanyan, JLab, email: [stepanya@jlab.org](mailto:stepanya@jlab.org)

# MesonEx Collaboration

M. Battaglieri, A. Bersani, A. Casale, A. Celentano, R. Cereseto, F. Cipro, R. De Vita,  
S. Fegan, V. Kulikovskiy, G. Mini, P. Musico, M. Osipenko, G. Ottonello, F. Parodi,

F. Pratolongo, R. Puppo, M. Ripani, M. Taiuti  
*Istituto Nazionale di Fisica Nucleare, Sezione di Genova*  
*e Dipartimento di Fisica dell'Università, 16146 Genova, Italy*

V. D. Burkert, L. Elouadrhiri, V. Kubarovsky,  
P. Nadel-Turonski, E. Pasyuk, S. Stepanyan, M. Ungaro, D. Weygand

*Jefferson Lab, Newport News, VA 23606, USA*

J. Fleming, D. I. Glazier, S. Hughes, D. P. Watts  
*Edinburgh University, Edinburgh EH9 3JZ, United Kingdom*

C. Salgado, M. Khandaker  
*Norfolk State University, Norfolk VA 23504, USA*

A. Szczepaniak

*Physics Department and Nuclear Theory Center, Indiana University, Bloomington, Indiana 47405*

S. Aune, J. Ball, G. Charles, M. Garçon, I. Mandjavidze, B. Moreno, H. Moutarde, S.  
Procureur, F.Sabatié<sup>†</sup>

*CEA-Saclay, Service de Physique Nucleaire, F91191 Gif-sur-Yvette, France*

A. Fradi, B. Guegan, M. Guidal, S. Niccolai, S. Pisano, D. Sokhan  
*Institut de Physique Nucleaire d'Orsay, IN2P3, BP 1, 91406 Orsay, France*

K. Hicks

*Ohio University, Department of Physics, Athens, OH 45701, USA*

K. Giovanetti, G. Niculescu, I. Niculescu  
*James Madison University, Harrisonburg, Virginia 22807*

K. Joo

*University of Connecticut, Storrs, Connecticut 06269*

M. Anderson, D. Ireland, K. Livingston, D. MacGregor, B. McKinnon,  
D. Protopopescu, G. Rosner, B. Seitz

*University of Glasgow, Glasgow G12 8QQ, United Kingdom*

A. Afanasev, W. J. Briscoe, H. Habertzettl, A. Micherdzinska, M. Paris, I. I. Strakovsky  
*The George Washington University, Washington, D.C., 20052*

A. Kubarovsky, P. Stoler

*Rensselaer Polytechnic Institute, Department of Physics, Troy, NY 12181, USA*

L. Guo

*Florida International University, Miami, Florida 33199*

W. Brooks, H. Hakobyan, S. Mancilla, R. Oyarzun  
*Universidad Técnica Federico Santa María, Valparaíso, Chile*

B.Nefkens, A. Starostin  
*University of California at Los Angeles, Department of Physics and Astronomy, Los Angeles, CA  
90095-1547, USA*

A. D'Angelo, C. Shaerf, I. Zonta  
*Istituto Nazionale di Fisica Nucleare, Sezione di Roma 2 e Dipartimento di Fisica dell'Università di Roma  
Tor Vergata, Roma, Italy*

M. Aghasyan, S. Anefalos Pereira, E. De Sanctis, D. Hasch, V. Lucherini, M. Mirazita,  
S. Pisano, P. Rossi  
*Istituto Nazionale di Fisica Nucleare, Laboratori Nazionali di Frascati, P.O. 13, 00044 Frascati, Italy*

M. Capogni, D.M. Castelluccio, E. Cisbani, S. Frullani, F. Garibaldi, F. Meddi, G. M.  
Urciuoli  
*Istituto Nazionale di Fisica Nucleare, Sezione di Roma e Gruppo Collegato Sanità, e Università La  
Sapienza, Italy*

R. De Leo  
*Istituto Nazionale di Fisica Nucleare, Sezione di Bari e Dipartimento di Fisica dell'Università, Bari, Italy*

R. Perrino  
*Istituto Nazionale di Fisica Nucleare, Sezione di Lecce 73100 Lecce, Italy*

V. Bellini, A. Giusa, F. Mammoliti, G. Russo, M. L. Sperduto, C. M. Sutura  
*Istituto Nazionale di Fisica Nucleare, Sezione di Catania e Dipartimento di Fisica dell'Università, Catania,  
Italy*

L. Barion, G. Ciullo, M. Contalbrigo, P. Lenisa, L. Pappalardo  
*Istituto Nazionale di Fisica Nucleare, Sezione di Ferrara e Dipartimento di Fisica dell'Università, Ferrara,  
Italy*

J. Dumas, C. Maieron, Y. Perrin, E.Voutier  
*Laboratoire de Physique et de Cosmologie, CNRS/IN2P3, 38026 Grenoble, France*

*and the CLAS Collaboration*

## **Abstract**

This document presents the technical layout and the envisaged performance of the CLAS12 Forward Tagger (FT). The FT, composed by an electromagnetic calorimeter (FT-Cal) a hodoscope (FT-Hodo) and two layers of Micromegas trackers (FT-Trck), has been designed to meet the physics goals of the meson spectroscopy program and other experiments running in Hall-B.

# Contents

<b>1</b>	<b>Executive Summary</b>	<b>10</b>
1.1	The MesonEx experiment	10
1.2	Electroproduction at very small $Q^2$	10
1.3	The CLAS12 detector	11
1.3.1	CLAS12 components	13
1.3.2	Particle Identification	14
1.4	The Forward Tagger	16
1.4.1	The em calorimeter (FT-Cal)	17
1.4.2	The hodoscope (FT-Hodo)	18
1.4.3	The tracker (FT-Trck)	18
1.4.4	Kinematic, rates and background	19
1.4.5	Other requirements	20
1.5	Conclusion	20
<b>2</b>	<b>FT-Cal</b>	<b>22</b>
2.1	PbWO <sub>4</sub> crystals	22
2.1.1	Crystal geometry	23
2.1.2	Crystal properties: ACCOS	23
2.1.3	Absolute Light Yield $LY_A$	26
2.1.4	Decay time	27
2.1.5	Quality requirements and control	30
2.2	Photo-detectors	30
2.2.1	APD	30
2.2.2	SiPM	36
2.3	FE & RO electronics	39
2.3.1	The Orsay preamplifier: FT-Orsay	39
2.3.2	FT-Cal motherboard	42
2.3.3	Readout electronics	43
2.4	Slow controls	45
2.4.1	APD bias system	45
2.4.2	Low voltages	45
2.4.3	Chiller and T control	45
2.4.4	LED monitor system.	46
2.5	Mechanical design	46
2.5.1	Single crystal assembly	46
2.5.2	Module design	47
2.5.3	Cooling	47
2.6	Light Monitoring System	48
2.6.1	INFN-LEDMON prototype	50
2.6.2	INFN-LEDMON final design	52
2.7	FT-Cal simulations	53
2.7.1	Geometry	54
2.7.2	Digitization	55
2.7.3	Shower reconstruction algorithm	56

2.7.4	Leakage corrections . . . . .	57
2.7.5	Energy Resolution . . . . .	57
2.7.6	Spatial resolution . . . . .	59
2.7.7	Electromagnetic background rates . . . . .	60
2.7.8	Radiation dose . . . . .	61
2.8	Prototype tests . . . . .	61
2.8.1	The Proto-9 . . . . .	62
2.8.2	The Proto-16 . . . . .	64
2.9	Planning, costs and funding . . . . .	69
2.9.1	Planning . . . . .	69
2.9.2	Costs . . . . .	70
2.9.3	Fundings . . . . .	70
<b>3</b>	<b>FT-Hodo</b>	<b>71</b>
3.1	Design Requirements . . . . .	71
3.1.1	Design . . . . .	71
3.1.2	Detector Element design . . . . .	72
3.1.3	Mechanical structure and readout . . . . .	73
3.1.4	Resistance of hodoscope and readout to radiation . . . . .	75
3.2	Data Acquisition . . . . .	76
3.2.1	Front End and Readout electronics . . . . .	76
3.2.2	Slow controls . . . . .	78
3.3	Simulations . . . . .	78
3.3.1	Optical Photon Tracking in single Element . . . . .	79
3.3.2	Combined simulation of Hodoscope array and FT-Cal . . . . .	81
3.4	Frascati Beam tests . . . . .	82
3.5	FTHodo summary . . . . .	83
<b>4</b>	<b>FT-Trck</b>	<b>85</b>
4.1	Tracker design . . . . .	85
4.1.1	Micromegas geometry . . . . .	85
4.2	Electronics and DAQ . . . . .	85
4.2.1	Channel count . . . . .	86
4.2.2	Front-End electronics . . . . .	86
4.2.3	Backend electronics . . . . .	87
4.2.4	Clock/trigger distribution and data and control flow . . . . .	87
4.2.5	Frontend Units . . . . .	88
4.2.6	FT-Trck data volume . . . . .	88
4.2.7	Services . . . . .	89
4.3	High voltage and gas system . . . . .	89
4.3.1	High voltage distribution system . . . . .	89
4.3.2	Gas system . . . . .	89
4.4	Expected performance . . . . .	90
4.4.1	Event generation . . . . .	90
4.4.2	Clustering, point association and first cuts . . . . .	90
4.4.3	Matching with the calorimeter . . . . .	91

4.4.4	Backward extrapolation . . . . .	91
4.4.5	Results . . . . .	92
4.5	Costs and planning . . . . .	93
4.5.1	Electronics . . . . .	93
4.5.2	Detectors . . . . .	93
<b>5</b>	<b>Integration and Installation</b>	<b>94</b>
5.1	Introduction . . . . .	94
5.2	Constraints from other sub-detectors . . . . .	94
5.3	FT mounting procedure . . . . .	95
5.4	Installation in CLAS12 . . . . .	95
5.5	Cabling and services routing . . . . .	97
<b>6</b>	<b>FT Commissioning and Calibration</b>	<b>99</b>
6.1	Quality assurance and system checks . . . . .	99
6.1.1	FT-Cal, PBWO Crystals . . . . .	99
6.1.2	FT-Cal, APD . . . . .	99
6.1.3	FT-Cal, Front-End electronics . . . . .	99
6.1.4	FT-Cal, cooling system . . . . .	99
6.1.5	FT-Cal, Read-Out Electronics . . . . .	100
6.1.6	FT-Cal, Slow controls . . . . .	100
6.1.7	FT-Cal, LED monitoring system . . . . .	100
6.1.8	FT-Cal, Cables . . . . .	100
6.1.9	FT-Hodo, Prototyping . . . . .	100
6.1.10	FT-Trck, Micromegas . . . . .	101
6.1.11	FT-Cal, Checks . . . . .	101
6.1.12	FT-Cal, Checks with cosmic rays . . . . .	101
6.2	System checkout . . . . .	101
6.2.1	FT-Cal, Checkout with LED system . . . . .	102
6.2.2	FT-Hodo, Checkout with cosmic rays . . . . .	102
6.2.3	FT-Trck, Checkout . . . . .	102
6.2.4	FT-CAL, LED monitoring . . . . .	102
6.3	Calibration with cosmic rays . . . . .	102
6.4	Commissioning with beam . . . . .	103
6.4.1	Beam run - FT $e^-$ calibration . . . . .	103
6.4.2	Beam run - FT $\pi^0$ calibration . . . . .	103
<b>7</b>	<b>FT DAQ and trigger</b>	<b>104</b>
7.1	Trigger requirements . . . . .	104
7.1.1	Electroproduction trigger rate . . . . .	105
7.1.2	Quasi-real photoproduction trigger rate . . . . .	106
7.2	Front-End for Fast Detectors . . . . .	107
7.3	CLAS12 Trigger . . . . .	107
7.3.1	Trigger System Timing and Layout . . . . .	107
7.3.2	Level 1 Trigger . . . . .	108
7.3.3	Level 1 Timing . . . . .	109
7.4	Readout Controllers . . . . .	109

7.5	Computing and Network . . . . .	110
7.6	Forward Tagger Trigger . . . . .	110
7.6.1	Level 1 FT Trigger . . . . .	111
7.6.2	Level 2 FT Trigger . . . . .	112
7.7	FT fADC channel distribution . . . . .	113
<b>8</b>	<b>FT Performance</b>	<b>114</b>
8.1	GEANT4 simulations . . . . .	114
8.1.1	Acceptance . . . . .	114
8.1.2	Energy resolution . . . . .	115
8.1.3	Spacial resolution . . . . .	115
8.2	Count-rate and occupancy . . . . .	115
8.2.1	CLAS12 DC occupancy . . . . .	115
8.3	Benchmark studies . . . . .	116
8.3.1	The reaction $\gamma p \rightarrow n\pi^+\pi^+\pi^-$ . . . . .	117
8.3.2	The reactions $\gamma p \rightarrow pK^+K^-\pi^0$ and $\gamma p \rightarrow nK^+K^-\pi^+$ . . . . .	119
8.4	GEANT4 simualtions of the reaction $\gamma p \rightarrow nX \rightarrow n\pi^+\pi^+\pi^-$ . . . . .	120
8.4.1	Conclusions . . . . .	121

# 1 Executive Summary

## 1.1 The MesonEx experiment

The phenomenology of hadrons and in particular the study of their spectrum led more than forty years ago to the development of the quark model, where baryons and mesons are described as bound systems of three quarks and of a quark-antiquark pair, respectively. While this picture still holds and has been proved to reproduce many features of the hadron spectrum, now we know that the hadron mass cannot be explained only in terms of the quark masses, but it is mainly due to the dynamics of the gluons that bind them. Measuring the spectrum of hadrons, studying their properties and inner structure is therefore crucial to achieve a deep knowledge of the strong force.

Mesons, being made by a quark and an anti-quark, are the simplest quark bound system and therefore the ideal benchmark to study the interaction between quarks, understand what the role of gluons is and investigate the origin of confinement. The quark model predicts the existence of multiplets of mesons with similar properties, that are classified according to their total angular momentum  $J$ , the parity  $P$ , and charge conjugation  $C$ . While most of the lowest mass states have been clearly identified and studied [1], several open issues related to the mass hierarchy and decays of excited states remain and still await for a thorough experimental investigation. In addition phenomenological models [2, 3, 4, 5, 6, 7] and lattice QCD calculations [8, 9] suggest that states beyond the simple  $q\bar{q}$  configuration, as hybrids ( $qqg$ ), tetraquarks ( $qq\bar{q}\bar{q}$ ) and glueballs, should also exist. If so, we should expect to find a much richer spectrum than that predicted by the quark model and, in particular, we should be able to observe new meson multiplets corresponding to these unconventional configurations. Hybrid mesons are of particular interest as they are the cleanest experimental signature for the presence of

gluons in the dynamical mass generation process. A precise determination of their spectrum and properties can provide a unique opportunity to study the role of the glue and to understand the phenomenon of confinement. An unambiguous identification of these states can in general be rather difficult, since they can mix with ordinary mesons having the same quantum numbers ( $J^{PC}$ ). However, the additional degrees of freedom present in these states can also lead to *exotic* quantum numbers that are not allowed in  $q\bar{q}$  systems and therefore provide a unique signature of their unusual structure.

MesonEx (JLab Exp-11-005 [10]) is an experimental program to study meson spectroscopy via quasi-real photoproduction in Hall B, using the CLAS12 detector and a new Forward Tagger facility (FT).

The 12 GeV electron beam available after the upgrade of Jefferson Lab, the excellent characteristics of the CLAS12 detector and of the new FT facility will give the possibility of exploring a broad mass range accumulating data of unprecedented accuracy and statistics.

## 1.2 Electroproduction at very small $Q^2$

Phenomenological models, like the flux-tube model, indicate that the photon may be more effective in producing exotics hybrids than, for example, the pion. The rationale for this lies in the fact that the photon spin is 1 and it can fluctuate into a  $q\bar{q}$  pair with spins aligned. When a  $q\bar{q}$  pair with  $\vec{S} = 1$  is excited into an hybrid, the production of exotic quantum numbers is expected to be favored. On the contrary, when in the initial state there is a  $q\bar{q}$  pair with  $\vec{S} = 0$ , like for pion beams, the resulting hybrid mesons are more likely to be non-exotic. Phenomenological studies also indicate that exotic mesons can be produced with photon probes with cross sections that are comparable to ordinary mesons [11, 12]. Finally, the linear polarization of the quasi-

real photons is expected to be a very powerful tool for high precision amplitude analysis, since it can provide information on the production mechanism and act as a filter on background from other processes.

The current photoproduction setup of the CLAS experiment, producing real bremsstrahlung photons tagged by a magnetic spectrometer, can not be operated at 11 GeV energies because of the limitation of the existing magnet. Instead, we are planning to use quasi-real photons produced when electrons are scattered at very small angles (small  $Q^2$ ).

Electron detection at very small angles, ( $Q^2$  values of about  $10^{-1}$  GeV<sup>2</sup> or lower) with the coincidence detection of the hadronic final states in CLAS12, is a very attractive alternative to pure photoproduction experiments [13]. This technique was used in the past to produce high energy ( $\sim 100$  GeV) photon beams at CERN ( $\Omega$  [14] and COMPASS [15] Collaborations) and DESY (ZEUS [16] and H1 [17] experiments). First tests were performed with CLAS, by looking for hadronic events where the electron was undetected. Final states where the hadron four-momenta were compatible with an electron scattered at  $\sim 0^\circ$  were selected. The reconstructed mass spectra of  $\pi^0\pi^0$  and  $\pi^0\eta$  show clear evidence of low cross section mesons expected in these channels ( $f_0(980)$ ,  $f_2(1270)$ ,  $a_0(980)$ ) demonstrating the potential of this technique (see Fig. 1).

At very low values of  $Q^2$  the virtual photon beam becomes, for all practical purposes, almost a real photon beam, since

$$\epsilon_L = \frac{Q^2}{\nu^2}\epsilon = 10^{-3}\epsilon \approx 0.$$

Via these relations, the photon polarization can be defined on an event-by-event basis, simply measuring the electron three momentum. The polarization plane coincides with the electron scattering plane and the degree of polarization mainly depends on the energy. The associated systematic uncertainty

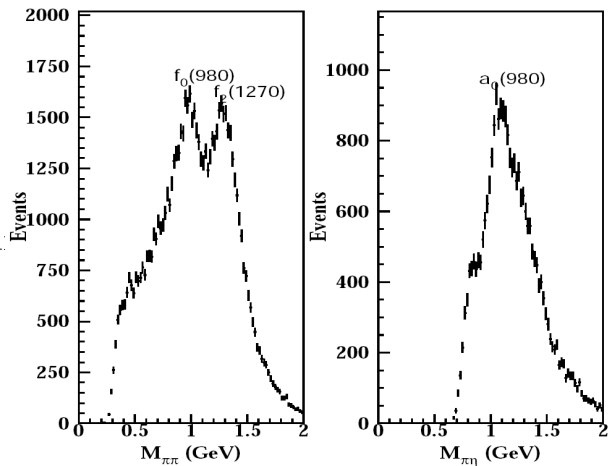


Figure 1: Invariant mass distribution for  $\pi^0\pi^0$  (left) and  $\pi^0\eta$  (right) for the reactions  $ep \rightarrow p\pi^0\pi^0(e)$  and  $ep \rightarrow p\pi^0\eta(e)$ , respectively. In both cases, the protons and 4 photons from the meson decays were detected while the final state electron was unmeasured, being emitted at  $0^\circ$ .

is only affected by the electron detection resolution. These are significant advantages with respect to coherent bremsstrahlung beams, where only the average polarization can be determined and its value is based on model calculations (or parallel measurement of reactions with known linear polarization asymmetries). Among other advantages of low  $Q^2$  electroproduction is the possibility of running on thin targets and the better control on the absolute photon flux normalization. Since electrons are tagged after their target interactions, this technique allows the use of high electron currents, permitting to achieve high luminosity on thin (gas) targets not operable with photon bremsstrahlung beams. With no need for dedicated normalization equipment and procedures [19], the number of photons can be directly calculated from the measured electron beam current.

### 1.3 The CLAS12 detector

The 12-GeV upgrade of the Continuous Electron Beam Accelerator Facility (CEBAF) at Jefferson Lab includes the upgrade of ma-

chine energy to 12 GeV and equipment in the experimental Halls. The detector in Hall B, CLAS [19], will be upgraded to CLAS12 [20]. The CLAS12 detector, see Figure 2, is designed to carry out experiments using high energy electron beams incident on polarized and unpolarized targets at luminosities up to  $L = 10^{35} \text{ cm}^{-2} \text{ sec}^{-1}$ . CLAS12 will carry out the core program for the study of the internal dynamics and 3D imaging of the nucleon, quark hadronization processes, and hadron spectroscopy in multi-particle, exclusive and semi-inclusive final states. CLAS12 consists of two parts, a forward detector (FD) and a central detector (CD).

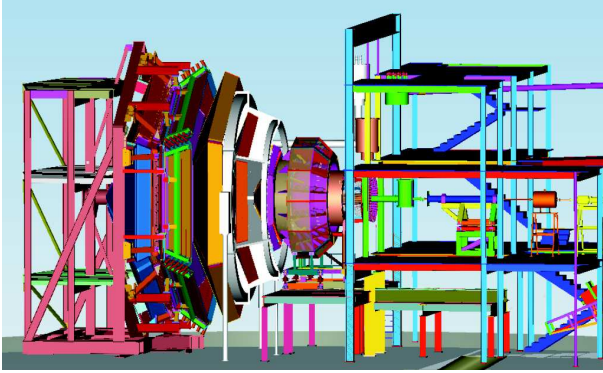


Figure 2: The CLAS12 detector in Hall-B.

The FD makes use of some of existing detector components of CLAS and the Hall B infrastructure. Major new components include the superconducting torus coils, now only covering the forward angles, a new gas Cerenkov counter for electron/pion separation, a new forward vertex tracker and forward drift chambers, some additions to the electromagnetic calorimeters and to the time-of-flight system.

The CD is based on a 5T superconducting solenoid magnet and consists of barrel tracker and time-of-flight scintillators. The solenoid field will also be used to shield Möller electrons for the FD. CLAS12 target system will be located at the center of CD. Planned targets for CLAS12 range from liquid hydrogen to tin. CLAS12 will have longitudinally

and transversely polarized hydrogen and deuterium targets as well. There are ongoing efforts in the collaboration to supplement the base equipment in Hall B with detector components that will improve the overall CLAS12 capabilities (e.g. neutral detection in CD, high energy kaon identification in FD).

Parameters	Forward Detector
Charged tracks:	
polar angular range ( $\theta$ )	$5^\circ$ to $35^\circ$
polar angular resolution ( $\delta\theta$ )	$< 1 \text{ mr}$
azimuthal angular resolution ( $\delta\phi$ )	$< 4 \text{ mr}$
momentum resolution ( $\delta p/p$ )	$< 1\%$ at 5 GeV/c
Neutral particles:	
polar angular range ( $\theta$ )	$5^\circ$ to $40^\circ$
polar angular resolution ( $\delta\theta$ )	$< 4 \text{ mr}$
Energy/momentum resolution	$< 0.1/\sqrt{E}$
Particle identification:	
e/ $\pi$	in full momentum range
$\pi/p$	in full momentum range
K/ $\pi$	$< 3 \text{ GeV}/c$
K/p	$< 4 \text{ GeV}/c$
Parameters	Central Detector
Charged tracks:	
polar angular range ( $\theta$ )	$35^\circ$ to $125^\circ$
polar angular resolution ( $\delta\theta$ )	$< 10 \text{ mr}$ to $20 \text{ mr}$
azimuthal angular resolution ( $\delta\phi$ )	$< 5 \text{ mr}$
momentum resolution ( $\delta p/p$ )	$< 5\%$ at 1.5 GeV/c
Neutral particles:	
polar angular range ( $\theta$ )	$40^\circ$ to $125^\circ$ (neutrons)
polar angular resolution ( $\delta\theta$ )	$< 10 \text{ mr}$
Energy/momentum resolution	$< 5\%$
Particle identification:	
e/ $\pi$	NA
$\pi/p$	$< 1.25 \text{ GeV}/c$
K/ $\pi$	$< 0.65 \text{ GeV}/c$
K/p	$< 1 \text{ GeV}/c$

Table 1: CLAS12 design characteristics.

### 1.3.1 CLAS12 components

The design characteristics of CLAS12 are presented in Table 1. Particles in CLAS12 will be detected and identified by measuring their momenta, time-of-flights, number of photons produced in threshold Cherenkov counters, and energy losses in the calorimeters and scintillator counters.

The forward detector will detect and identify charged and neutral particles scattered between  $5^\circ$  and  $40^\circ$ , in the full momentum range. Particles will be detected in six identical magnetic spectrometers based on six coils, superconducting toroidal magnet. Each spectrometer, corresponding to each sector of the FD, will be equipped with a forward vertex tracker (FVT), high threshold Cherenkov counter (HTCC), a set of drift chambers (FDC), low threshold Cherenkov counter (LTCC), scintillation counters (FTOF), and electromagnetic calorimeters (FEC), see Figure 3. Trajectories of charged particles, and hence their momenta and path lengths will be measured using FDC. FDC has three regions. Each region consists of two stereo superlayers ( $\pm 6^\circ$  stereo angles). The FDC first region will be located in front of the torus coils, outside of the torus field region, the second region will be positioned between the coils, inside the high field region, and the third region will be placed outside the torus coils. Each superlayer will consist of six layers of hexagonal drift cells where wires are strong perpendicular to the mid-plane of the given sector. The FVT will be based on Si-strip detectors and will be mounted  $\sim 25$  cm downstream of the solenoid center (target center). Vertex tracker will give an accurate reconstruction of the track parameters at the production vertex in presence of a high longitudinal magnetic field of the solenoid. Three planes of scintillator counters, with  $\sim 80$  ps time resolution form the forward time-of-flight system, FTOF. The time measured in FTOF will be used together with the path length and momentum measured in FDC for charged

hadron identification. Two threshold Cherenkov counters, HTCC with  $\text{CO}_2$  radiator and pion momentum threshold of  $4.9 \text{ GeV}/c$ , and LTCC with  $\text{C}_4\text{F}_{10}$  radiator and pion momentum threshold of  $2.7 \text{ GeV}/c$ , will be used to identify electrons and high momentum charged pions. The forward electromagnetic calorimeters will be used to measure energy of em showering particles ( $e^-$ ,  $\gamma$ ) and hit time. Calorimeters have stereo readout system in the transverse plane (transverse to the mid-plane of the sector) and are segmented in the longitudinal direction. Stereo readout system with fine transverse segmentation will allow to determine hit position with  $\sim 1 \text{ cm}$  accuracy and separate close lying showers (e.g. from high energy  $\pi^0 \rightarrow \gamma\gamma$  decay). The longitudinal segmentation will help in identification of electromagnetic showers for  $e/\pi$  separation. FEC is the main detector in forward region of the CLAS12 for neutron detection. Identification of neutrons and determination of their momenta will be done by timing measurements in FEC.

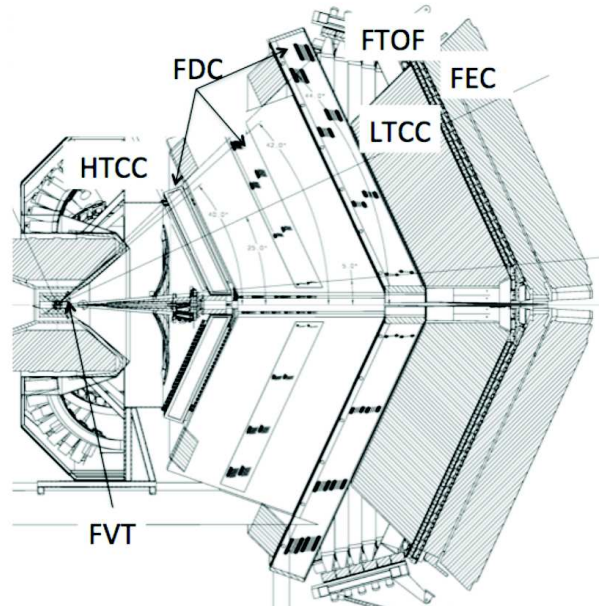


Figure 3: Midplane view of the CLAS12 forward detector.

The central detector is meant to measure

charged hadrons and neutrons in an angular range from  $35^\circ$  to  $125^\circ$  and momenta  $< 1.5$  GeV/c. Charged particles will be detected by two barrel shaped detectors, Si-tracker (BST) and time-of-flight counters (CTOF), see Figure 4. Both detectors are positioned inside the solenoid magnet and cover the full azimuthal angular range. BST will measure momentum of charged tracks with a resolution better than 5%. CTOF will measure charged particles time-of-flight with 60 ps resolution. BST consists of four two layer silicon planes. CTOF consists of 50 scintillation counters. As was previously mentioned, there will be a neutron detector positioned between CTOF and the cryostat of the solenoid, see Figure 5. Neutrons will be detected with 10% efficiency and with momentum resolution of  $\sim 5\%$ .

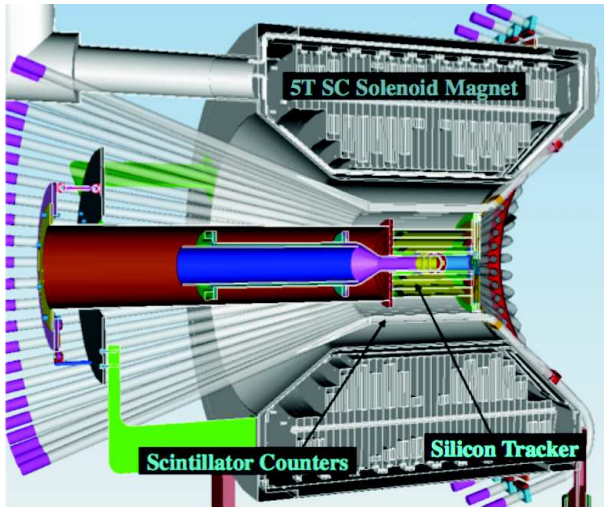


Figure 4: CLAS12 central detector.

CLAS12 will have free running DAQ system. ADCs and TDCs will collect data in pipeline mode. Readout of data will be performed after trigger decision is made. The expected event readout rate is of the order of 10kHz.

### 1.3.2 Particle Identification

CLAS12 particle identification (PID) sys-

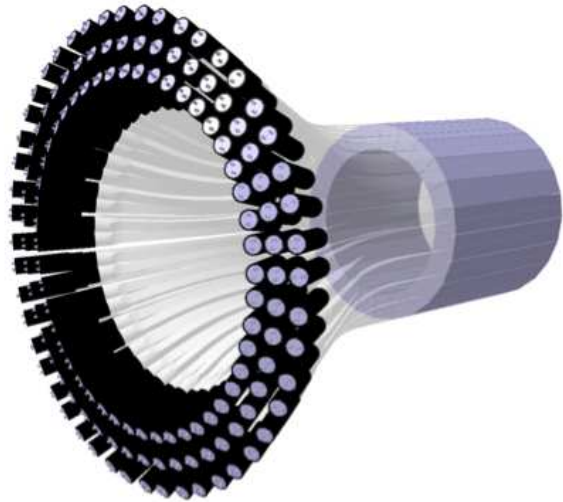


Figure 5: Neutron detector of CD.

tem has three main components; electron identification, charged hadron identification ( $p$ ,  $\pi^\pm$ ,  $K^\pm$ ), and neutral particle identification ( $n$ ,  $\gamma$ ). Electrons and photons will be detected and identified in FD, while charged hadrons and neutrons in both FD and CD.

Electron identification is the most important component of PID and will be used for each CLAS12 experiment. A reliable electron ID is required not only for the off-line analysis but also at trigger level. To keep the trigger rate at a manageable level, a charged pion suppression at level of few  $\times 10^3$  is required. Electrons with  $P < 4.7$  GeV/c will be identified using photoelectron statistics in HTCC and fractional energy deposition in FEC. Above 4.7 GeV/c only energy deposited in FEC will be used for electron identification. In Fig. 6 the electron identification scheme is presented. On the left graph, rates of negative pions and electrons are shown as a function of momentum. By requiring the coincidence of HTCC and FEC, pions will be suppressed by three orders of magnitude (shown by the red line distribution on the graph). In order to make HTCCxFEC coincidence, the tracking information is needed at the trigger level to connect HTCC segment with a cluster in FEC. In off-

line analysis, using transverse and longitudinal distributions of the shower in FEC, pion reduction can be improved by another factor of 10-100, depending on the momentum of the track.

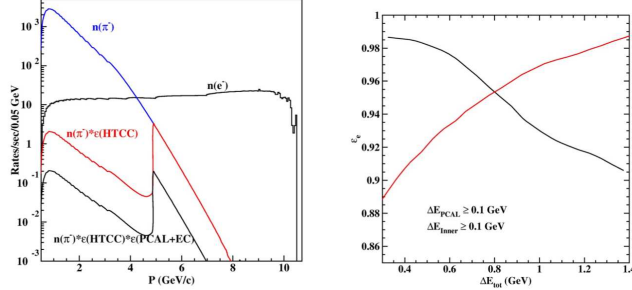


Figure 6: Electron identification in FD. On the left expected rates of electrons (black line) and  $\pi^-$ s (blue line) at beam energy of 11 GeV and at luminosity of  $10^{35} \text{ cm}^{-2} \text{ sec}^{-1}$ . The red line shows pion suppression at the trigger level. The lower black line is pion suppression available in off-line analysis. On the right graph electron efficiency vs. pion suppression factor for momenta 4.7 GeV/c where for electron ID only fractional energy deposited in FEC will be used.

Charged hadron identification in both FD and CD will rely on momentum and time measurements. Time difference as a function of momentum between different particle species is presented in Figure 7. FTOF, with a time resolution of 80 ps and an average path length of  $\sim 650$  cm from the target to the plane, will allow  $5\sigma$  K/ $\pi$  separation with momenta  $P < 2.6$  GeV/c, p/K separation with  $P < 4$  GeV, and p/ $\pi$  separation with  $P < 5$  GeV/c (see left graph of the figure). CTOF time resolution will be 60 ps. This will allow K/ $\pi$  separation for up to 0.6–0.7 GeV/c and p/K separation for up to 1.2 GeV as shown by solid and dashed lines on right graph of Figure 7, respectively. In some cases, exploiting the exclusive kinematics of the final state, the above momentum ranges can be extended larger values. In addition to time-of-flight method, Cherenkov counters in the FD can

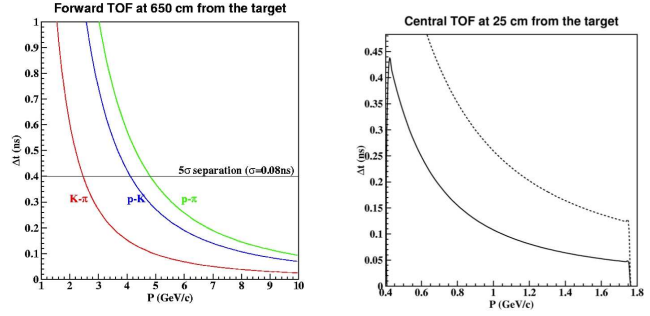


Figure 7: Charged hadron ID. On the left graph time difference vs. momentum of a track is shown for kaons and pions (red), protons and kaons (blue), and protons and pions (green). On the right graph the same dependence is shown for kaons and pions (solid line) and protons and kaons (dashed line).

be used for pion identification, e.g. LTCC for pions with momenta  $> 2.7$  GeV/c and HTCC for momenta  $> 4.9$  GeV. As was mentioned above, there are plans to improve particle ID, in particular for high energy charged kaons. A possible option is to replace LTCC with ring imaging Cherenkov counter (RICH).

Neutrons and photons in forward detector will be detected and identified using isolated clusters in FEC (not correlated with any track in FDC). Time resolution of FEC will be  $\sim 300$  ps. Distance from the target to FEC is  $\sim 700$  cm. This will allow to separate neutrons and photons with momenta up to 2.5 GeV/c at  $5\sigma$  level. The neutron detector of CD will be made by 10 cm thick scintillator bars. Low rate of photons at large angles and low detection efficiency for photons in the scintillator will make neutron detection in CD less challenging. A neutron in the neutron detector will be identified by a signal above a fixed threshold without a corresponding track in BST. The threshold value strongly affects the detection efficiency.

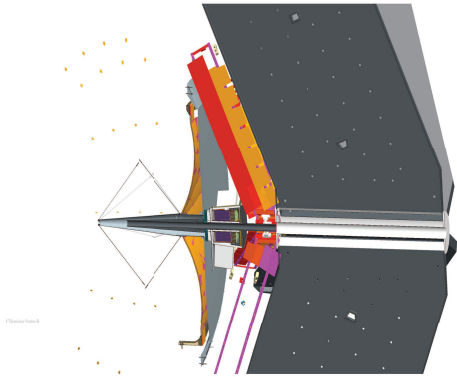


Figure 8: CAD drawing showing the integration of the FT in CLAS12. The FT is located in the free space between the HTCC and the first DC layer. The FT calorimeter shown in blue is located at about 190 cm from the interaction point, shown by the green cross, and is enclosed in a Rohacell case to provide thermal insulation. The scintillation counter (green) and first tracker layer (red) are located in front of the calorimeter. A tungsten cone in black shield the FT from Møller electrons and electromagnetic background created by the beam.

#### 1.4 The Forward Tagger

An experimental program focused on search for exotics and the study of rare mesons requires measurements of a broad scope of final states in order to consolidate the possible evidence of a resonance by looking at different decay modes and explore poorly-studied reaction channels. The characteristics of the detector and the trigger conditions foreseen for the experiment - 11 GeV electron beam scattering on a 5 cm long  $\text{LH}_2$  target with three prongs in the final state - will allow measurements of many final states simultaneously. While the hadrons will be detected in CLAS12, the electron scattered at very small angles (low  $Q^2$ ) will be detected in the Forward Tagger (FT). The FT specifications were thus defined to have the optimal electron detection at low angles compatible with the high rate of electromagnetic background.

To reconstruct the quasi-real photon variables is necessary to measure the scattered electron three momentum. The relevant quantities are:

- the energy  $E_{e'}$ : since the photon energy is given by  $E_\gamma = \nu = E_{Beam} - E_{e'}$  and its linear polarization by  $P_\gamma = \epsilon^{-1} = 1 + \frac{\nu^2}{2E_{Beam}E_{e'}}$
- the polar angle  $\phi_{e'}$  to determine the polarization plane
- the azimuthal angle  $\theta_{e'}$ : since  $Q^2 = 4E_{Beam}E_{e'} \sin^2 \theta/2$

The Forward Tagger will be made of: an electromagnetic calorimeter (FT-Cal), to identify the electron, measure the electromagnetic shower energy and provide a fast trigger signal, a tracker (FT-Trck), to measure the scattering angles ( $\theta_{e'}$  and  $\phi_{e'}$ ) with the required accuracy and a scintillation counter (FT-Hodo) to provide  $e/\gamma$  separation. A dedicated trigger system will be develop to provide a fast signal to trigger the data acquisition in coincidence with signals from CLAS12.

The calorimeter, the scintillation counter and the tracker will be placed between the High Threshold Cerenkov Counter (HTCC) and the torus support, at about 190 cm downstream of the target (nominal) position. The close proximity to the beam line ( $2.5^\circ$  corresponds to  $\sim 8$  cm) and the limited space available (at most  $\sim 40$  cm along the beam axis), requires a compact calorimeter with small radiation length and with very good radiation hardness. Figure 1.4 shows a CAD drawing of the FT integrated in CLAS12. The scintillation counter, placed in front of the calorimeter, will be made of plastic scintillator tiles read-out by silicon photomultipliers via wavelength shifting fibers. The tracking detector will be located in front of the scintillation counter to extend the CLAS12 forward tracker down to 2.5 degrees. All these components will be designed to fit within a  $5^\circ$  cone around the beam axis to have no impact on

the operation and acceptance of the CLAS12 equipment.

In the following requirements on the different FT components and possible technical solutions are discussed in more detail.

#### 1.4.1 The em calorimeter (FT-Cal)

The FT-Cal has to fulfill demanding requirements in terms of:

- high radiation hardness,
- high light yield,
- small radiation length and Moliere radius,
- fast recovery time,
- good energy and timing resolution.

As will be discussed in Sec. 8.3, the electron energy resolution is a crucial factor to determine precisely the photon energy and ensure the exclusivity of the measured reaction via missing mass technique. However, since we are interested in low energy electrons and high energy photons, the energy resolution on the latter will be significantly better than the resolution on the electron. For example, an electron energy resolution of 2% (at 1 GeV) would result in an energy resolution of  $\sim 0.2\%$  for the corresponding 10 GeV photon and would allow the use the missing mass technique for the most part of the studied reactions.

The FT should also have a fast recovery time ( $\tau \sim 10$  ns) to sustain high rates with small pile-up effects and provide the scattered electron interaction time with good accuracy ( $<1$  ns) to reject background and identify the signals via coincidence with CLAS12.

Due to the expected high rate from electromagnetic background, the calorimeter should be highly segmented in the transverse direction in order to maintain each channel at a sustainable readout-rate. The size of each pixel should be comparable with the characteristic transverse size of the electromagnetic

shower or Moliere radius to contain the signal induced by incident electrons to few pixels, thus minimizing pixel rates and pile-up.

Finally, the photodetectors for the light read-out will be placed in a sizable magnetic field and will have to be small in size to fit within the available space. The standard photomultiplier readout seems to be excluded while photodetectors based on semiconductors, e.g. Avalanche Photo Diode (APD) have been shown to meet the required criteria. Silicon Photo Multipliers (SiPM) can also be a valuable option but radiation hardness has to be tested.

To obtain the best performance we focused on a calorimeter based on homogeneous crystals. In fact, if the shower is longitudinally and transversely contained, the photoelectron fluctuations are the only sizable contribution to the energy and time resolution. In the recent years materials such as  $\text{PbWO}_4$  have been extensively studied and shown to be very resistant to radiation damage. They are now used in large scale detectors involving up to hundreds of thousands of crystals, such as CMS-ECal [21], ALICE-PHOS [22]), PANDA-EMC [23] and CLAS-IC [24]. Against a very fast scintillation decay time (6.5 ns), a very small radiation length (0.9 cm) and one of the smaller Moliere radii (2.1 cm), the main disadvantage of the  $\text{PbWO}_4$  is the poor light yield (only 0.3% of  $\text{NaI(Tl)}$ ). A 5% energy resolution, at 1 GeV, has already been achieved by the existing CLAS-IC with an APD-based readout. According to the PANDA-EMC study, new crystal manufacturing procedures ( $\text{PbWO}_4$  from BTCP) and the operation at temperature below  $0^\circ$  C should ensure a better performance, with a gain of a factor of 3-4 in light [23]\*.

With this design an energy resolution of  $(2\%/\sqrt{E(\text{GeV})} \oplus 1\%)$  is expected. Other crystals as LSO/LYSO (or the very recent LaBr) share almost all the good specifications

---

\*Due to the improvement in the crystal production, the  $\text{PbWO}_4$  Type-II LY is about two times of what quoted by CMS, resulting in a total gain of a factor of 6-8.

of the  $\text{PbWO}_4$  with a light yield more than 100 times bigger. However, the lack of extensive studies on radiation hardness and limited experience in the manufacturing procedures prevent them to be considered as an alternative.

*PbWO<sub>4</sub> is the choosed option for the Forward Tagger electromagnetic calorimeter FT-Cal.*

#### 1.4.2 The hodoscope (FT-Hodo)

The primary aim of the FT-Hodo is to discriminate between photons and electrons that produce electromagnetic shower in the calorimeter. In the design, the scintillation hodoscope will comprise of an array of plastic scintillators tiles covering individual or groupings of calorimeter elements. It should be possible to use larger tiles covering multiple calorimeter elements at the largest distance from the beam axis to reduce the level of instrumentation and readout required.

The high segmentation and restrictive geometry of the forward tagger precludes the use of light readout from the scintillator elements using standard light guides. Light readout with wavelength shifting (WLS) scintillating fibers embedded into the scintillator tile appears the most viable option and offers flexibility in routing away from the device. For effective operation the timing resolution of the hodoscope should be sufficient to select hodoscope-calorimeter coincident hits with a sufficiently low rate of accidentals. The timing resolution of the forward tagger calorimeter elements is expected to be better than 1 ns so the hodoscope timing should be comparable with this as not to compromise the achievable coincidence time resolution. Similar systems [25, 26, 27] have employed successful scintillator tile arrays achieving timing resolutions at the level of ns, using combination of WLS fiber coupled to optical fiber.

Measuring the energy deposits in the hodoscope elements with good energy resolution is not critical for our purpose. The vast ma-

jority of incident charged particles on the forward tagger will be highly relativistic resulting in a fixed minimum ionizing energy deposit regardless of particle type. The main requirements on the light collection are that sufficient photoelectrons are incident on the photon detection device considering the achievable light coupling in the scintillator and propagation in the fibres. Previous systems using WLS and optical fiber readout have sufficient photoelectrons per minimum ionizing interaction to achieve efficiencies for charged particle detection above 99.7% [26]. Readout sensors compatible with the high magnetic field present in the FT region are silicon photomultipliers (SiPM) that have already been used in this kind of detector. The scintillator hodoscope developed for the CLAS-IC produced 15 photoelectrons per minimum ionizing event from 1cm thick scintillator tiles with WLS fibers and  $1 \times 1\text{-mm}^2$  SiPM readout [27].

#### 1.4.3 The tracker (FT-Trck)

The role of the FT-Trck is to reconstruct the vertex angles of charged particles, essentially electrons, with polar angles between  $2.5^\circ$  and  $4.5^\circ$ . This is achieved by measuring the particle hit position with a dedicated tracking device, located in front of the FT calorimeter at few centimeters from the front face of the crystals. The reconstructed position will be used to evaluate the vertex angle, after correcting for the rotation induced by the 5 T solenoid field. The size of this rotation directly depends on the particle momentum and can be estimated based on a precise knowledge of the magnetic field map and the energy reconstructed by the FT-Cal. With a tracker spatial resolution of  $\pm 200\mu\text{m}$  a  $\sim 1.7\%$  and  $2.8^\circ$  resolution on  $\theta$  and  $\phi$  electron angles respectively, are expected.

The tracking device will consist of two double-layer Micromegas, each providing an independent measurement of the (X,Y) coordinates of a track. Double-faced Micromegas disks, bulked on a common PCB, will be used. Each

	<i>Range</i>
$E_{e'}$	0.5 - 4.5 GeV
$\theta_{e'}$	$2.5^\circ$ - $4.5^\circ$
$\phi_{e'}$	$0^\circ$ - $360^\circ$
$E_\gamma$	6.5 - 10.5 GeV
$P_\gamma$	70 - 10 %
$Q^2$	0.01 - 0.3 GeV <sup>2</sup> ( $< Q^2 > 0.1$ GeV <sup>2</sup> )
W	3.6 - 4.5 GeV

Table 2: Kinematic range of the FT.

side of the PCB displays strips with 500  $\mu\text{m}$  pitch, the downstream ones being perpendicularly oriented to the upstream ones. The hits reconstructed in both trackers will be matched, allowing to determine the trajectory parameters and to suppress noise. The reconstructed trajectory will be correlated with hits in the scintillator hodoscope and calorimeter to reduce backgrounds and improve resolution.

#### 1.4.4 Kinematic, rates and background

The kinematic range covered by the FT is shown in Tab. 2 for an incoming electron beam of 11 GeV. The energy range for electron detection was chosen to tag large energy photons and the angular range is the maximum allowed compatibly with the electromagnetic background.

The total electron scattering cross section contains contributions from one-photon exchange (Born process), from QED vacuum polarization loops, and from the emission of additional real photons (radiative corrections). The importance of the internal radiative corrections in relation to the Born process depends on the kinematics. Radiative corrections increase with decreasing  $Q^2$  and increasing  $E_\gamma$ . We used the program RADGEN 1.0 [28] to calculate the contributions of internal radiative corrections to the total inclusive cross section. Including such effects, the total

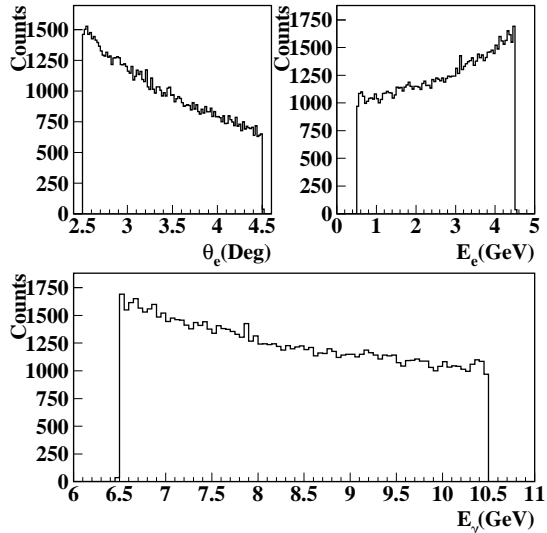


Figure 9: Angular and energy distribution of scattered electrons (top) and virtual photon energy distribution (bottom) within the geometrical and momentum acceptance of the FT.

inclusive electron rate within the geometrical and momentum acceptance of the forward tagger will be of about 130 kHz ( $\Delta E_{e'}=0.3$ - $10.8$  GeV and  $\Delta\theta_{e'}=2.5^\circ$ - $4.5^\circ$ ). Inelastic processes represent about 45% of the total cross section in our kinematic range. The remaining 55% is due to elastic events where at most one proton will go in the active area of CLAS12. It is, therefore, beneficial for our measurements to require a tight time coincidence between the forward tagger and the detection of multi-particle final states in the CLAS detector as discussed in Sec. 7.

The total rate of inelastic events in the forward tagger acceptance with  $E_\gamma=6.5$ - $10.5$  GeV, is expected to be about 6.5 kHz (while the radiative rate in the same energy range is about 40 kHz). The energy and the angular distributions of inelastic events are reported in Fig. 9. Figure 10 shows the  $Q^2$  and the linear polarization for the same events.

Electromagnetic backgrounds in the FT include bremsstrahlung and Møller processes. Bremsstrahlung photon production peaks at

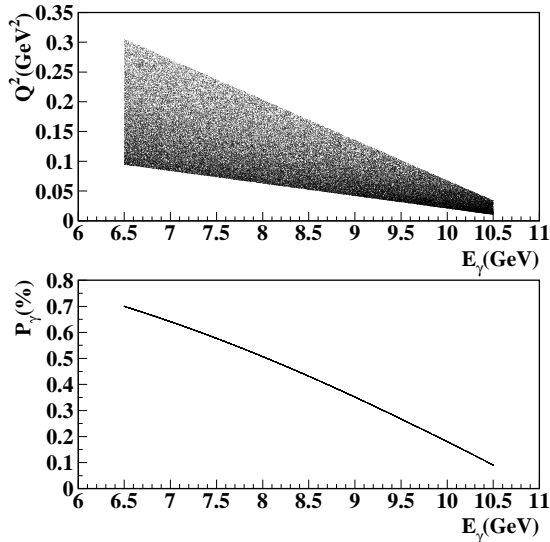


Figure 10:  $Q^2$  and linear polarization of inelastic events within the geometrical and momentum acceptance of the FT.

very forward angles (about  $\delta\theta \approx m_e/E_{Beam}$ ), therefore their contribution at angles  $\theta > 0.5^\circ$  is very small. Møller electrons and their secondaries are the dominant contribution to the expected FT rate. The Møller cross section is almost flat within the FT acceptance with a sizable value of about  $d\sigma/d\theta \sim 10\text{-}20$  mb/rad. However, the Møller kinematics is highly constrained and, for angles above  $2.5^\circ$ , the Møller electron energy is less than 0.5 GeV, i.e. outside the kinematic range of interest. These low energy electrons are bent in the 5T solenoidal field of CLAS12 and focused towards the beam line. Here they enter into a tungsten cone that shields CLAS12 and the FT from this background and from other secondaries produced along the beam line (low energy photons, X-rays, beam halo ...). These backgrounds have been studied using GEANT4 simulations. All details are reported in Sec. 2.7.7. The total expected electromagnetic rate is about 50 MHz, dominated by low energy ( $< 100$  MeV) secondaries that will be further suppressed by optimization of the shield. Suppression at the level of the on-line trigger is

discussed in Sec. 7. This contribution can be almost totally rejected in the off-line analysis when a time coincidence of a few nanoseconds with the rest of CLAS12 will be required, since there are no hadrons associated with such events to reach the CLAS12 detector.

#### 1.4.5 Other requirements

The FT will be designed as a part of the CLAS12 standard equipment and in particular, the tagger operations will be possible in parallel to the detection of the electron at larger angles ( $\theta_e > 5^\circ$ ) as required in the standard CLAS12 runs. In that respect, the FT facility can be viewed as an extension of the CLAS12 Electromagnetic Calorimeter (EC) allowing not only the measurement of electrons scattered at small angles but also providing an excellent coverage for  $\pi^0$  and  $\gamma$  emitted in the forward direction. In particular the leading *DVCS* experimental program in CLAS12 will benefit by the detection of the low-angle/high energy photon produced in the reaction. The FT coverage leads to a significant extension of the minimum momentum transfer allowing a precise mapping of this kinematic regime. For this reason the FT maximum energy detection should go up to 8 GeV keeping the good resolution necessary for gamma identification.

### 1.5 Conclusion

The MesonEx experiment (JLab Exp-11-005 [10]) aims at the study of meson spectroscopy using quasi-real photoproduction with CLAS12. The combination of CLAS12 and of the new FT system presents unique properties as:

- high intensity photon beams with energies up to 10.5 GeV,
- large degree of linear polarization determined on an event-by-event basis with small systematic uncertainty,
- full determination of the initial state and final state four-momenta,

	<i>Required performance</i>
Energy range $E_{min} - E_{max}$	0.5-8.0 GeV
Energy resolution $\sigma_E/E$	$\leq 2\%/\sqrt{E(\text{GeV})} \oplus 1\%$
Energy threshold (single crystal) $E_{thr}$	10 MeV
RMS noise (energy equiv.) $E_{noise}$	3 MeV
Angular resolution $\sigma_\theta/\theta$	1.5%
Angular resolution $\sigma_\phi$	$2^\circ$
Time resolution $\sigma_T/T$	$\leq 300$ ps
Recovery time	$\leq 10$ ns
Maximum rate (per crystal)	10MHz
Maximum dose rate (per crystal)	10 rad/h
Maximum integrated dose (per crystal)	5000 rad (before annealing)

Table 3: FT specifications.

- large acceptance and good resolution for the measurement of the decay products,
- kaon identification to study strangeness production.

The expected performance of the FT are summarized in Tab. 3.

In this TDR we'll demonstrate that a detector based on a PbWO calorimeter, a scintillating hodoscope and Micromegas tracker satisfies these requirements.

## 2 FT-Cal

### 2.1 PbWO<sub>4</sub> crystals

The use of the lead-tungstate (PbWO<sub>4</sub>) crystal for electromagnetic calorimetry has been extensively studied in recent years. The electromagnetic calorimeters built for leading experiments at CERN as CMS (EM-Cal) [21]) and ALICE (PHOS) [22]) were based on this technology. Against a high density, a small radiation length a very fast decay time and a very high radiation hardness, the lead tungstate light yield is quite poor (only a fraction of % of the NaI light yield). This can be a problem for precise spectroscopy of low energy showers (in the range of 10-100 MeV). In the last years the PANDA Collaboration devoted great efforts to increase the lead tungstate performance in terms of light emission [23]. The *R&D* performed in collaboration with the Bogoriditsk Technical Chemical Plant (BTC - Russia), lead to an improved version of PbWO<sub>4</sub> called Type-II, now commercially available from the same and other producers. Table 4 reports the main characteristics of the standard and improved lead tungstate.

As shown in Fig. 11 the temperature coefficient is  $dLY/dT \sim -3.0 \text{ \%}^\circ\text{C}$  in a wide temperature range. This would require a temperature stability of the whole volume of the FT-Cal at level of 0.1-0.2 °C. A dedicated active cooling system and an appropriate thermal design will provide the required stability. An additional increase in light yield, up to a factor of three-four compared to the room temperature operation (RT=+20 °C), is obtained cooling the PbWO (up to -25 °C). On the other hand low temperature operation would complicate the mechanical design requiring a thicker thermal insulation and a more sophisticated cooling system.

Other disadvantages related to the crystal low T operation are:

- reduced radiation hardness shown by cooled

Parameter	PbWO <sub>4</sub>	PbWO <sub>4</sub> -II
$\rho$ (g/cm <sup>3</sup> )		8.28
$X_0$ (cm)		0.89
$R_M$ (cm)		2.00
$\tau_{short}$ (ns)		6.5 (97%)
$\tau_{long}$ (ns)		30.4 (3%)
$\lambda_{max}$ (nm)		420
$nat\lambda_{max}$		2.24/2.17
LY <sub>RT</sub> (% <sub>RT</sub> NaI)	0.3	0.6
LY <sub>-25°C</sub> (% NaI)	0.8	2.5
dLY/dT <sub>RT</sub> (%°C)	-2.7	-3.0
dE/dx (MeV/cm)		10.2

Table 4: Properties of standard and improved (Type-II) lead tungstate.

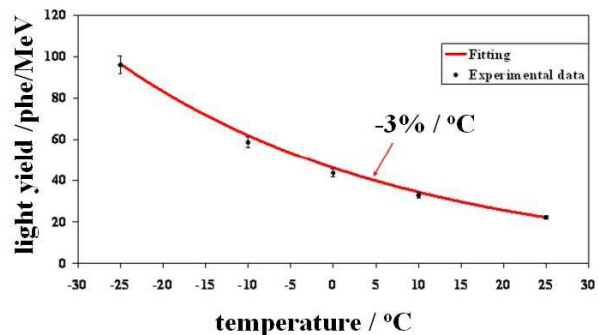


Figure 11: Temperature depends of the light yield of PBWO-II in the T range -25 °C +25 °C [23].

lead tungstate crystals. Figure 12 clearly shows this effect;

- longer decay time: according to the measurement reported in Ref. [29], at first order, the time constant changes from 15 ns at RT to 23 ns at -20 °C. This implies that to collect 90% of the signal the integration gate has to change from 35 ns to 50 ns.

For these reasons we are considering operating the FT-Cal at room temperature as main option, but the whole design will allow us to run it at 0 °C.

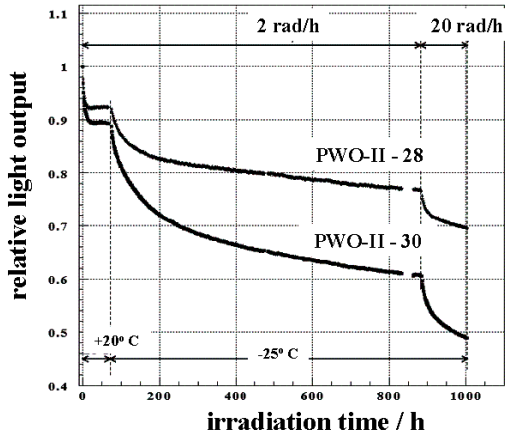


Figure 12: Relative change of light yield of two PbWO samples as a function of radiation dose (irradiation dose) at two temperatures [23].

### 2.1.1 Crystal geometry

Different geometries and sizes were tested by means of realistic simulations (see Par. 2.7.5). The length of the crystal was chosen according to the longitudinal propagation of the electromagnetic shower and the available space in CLAS12. The response of the calorimeter with crystal sizes of 18 cm, 20 cm, 22 cm has been simulated for electron/photons up to energies of 5 GeV. Results are reported in Fig. 71. For length longer than 18 cm there is not a significant loss of resolution and therefore we fixed the crystal size to 20 cm. As a thumb rule, the crystal cross section should be small enough to distribute the incoming rates on different crystals (high pixelization) and optimize the optical matching with the light sensor. On the other hand, due to the intrinsic radial dispersion of the electromagnetic shower, the minimum size has to be comparable with the Molier radius. We run simulations for different Crystal shapes: - parallelepiped, - truncated pyramid (with focused geometry towards CLAS12 target position), - parallelepiped with hexagonal faces. Since we did not find a clear advantage adopting a specific geometry, we decided to use the simplest one: parallelepiped shape with square

faces. The size of the face, 15x15 mm, was chosen taking into account the maximum possible coverage with the commercial LAAPDs produced by the Hamamatsu.

### 2.1.2 Crystal properties: ACCOS

To define a crystal characterization procedure, size, decay time, light yield, and light transmission have been measured on a sample of 9 BTCP PANDA-like crystals by using the ACCOS (Automatic Crystal quality Control System) facility at CERN [30]. ACCOS was built to measure properties of the CMS/EMC PbWO crystals and is now extensively used to test part of the PANDA/EC PbWO-II crystals. Properties are measured at room temperature and relative to a reference sample whose absolute properties are known. Since our crystals differ from PANDA only for geometrical size, the machine was calibrated in absolute value using a PANDA crystal.

**Geometrical dimensions** A 3D machine is used to measure crystal dimensions: fifteen points are measured on each lateral face of the crystals and nine points on the two end faces, allowing precise reconstruction of the six planes. The analysis algorithm reconstructs the shape of the crystal, performing a *best-fit* to each set of points belonging to a face with a plane. In this way, the *best-solid* matching the crystal is found. The *minimum-solid* and the *maximum-solid* are also reconstructed:

- the *minimum-solid* is formed by 6 planes, parallel to those of the *best-solid*, each passing through the most inner point of the corresponding face;
- the *maximum-solid* is formed by 6 planes, parallel to those of the *best-solid*, each passing through the most outer point of the corresponding face.

As an example Fig. 13 shows the longitudinal and transverse dimensions of the 9 crystals; the quoted error, asymmetrical, is calculated considering the difference between the

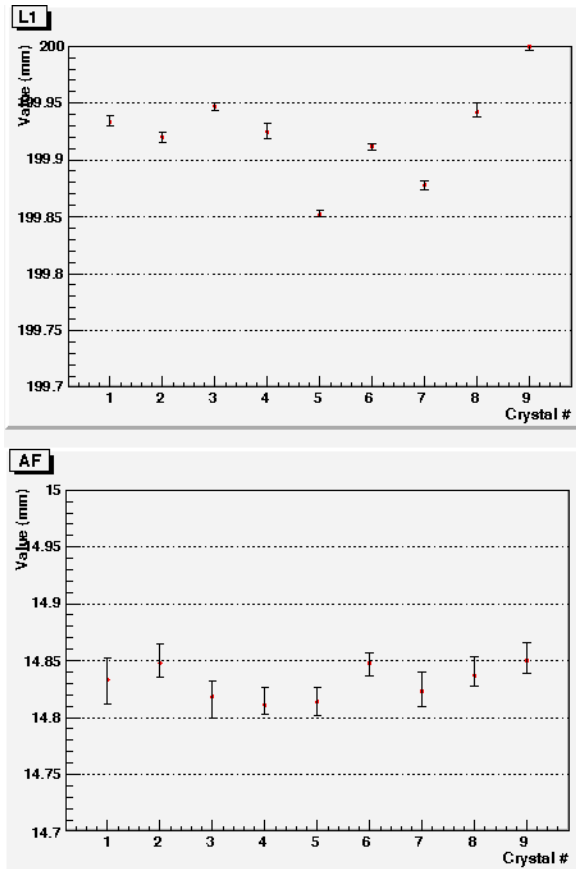


Figure 13: Longitudinal (top) and transverse (bottom) dimension of the 9 crystals tested with the ACCOS machine.

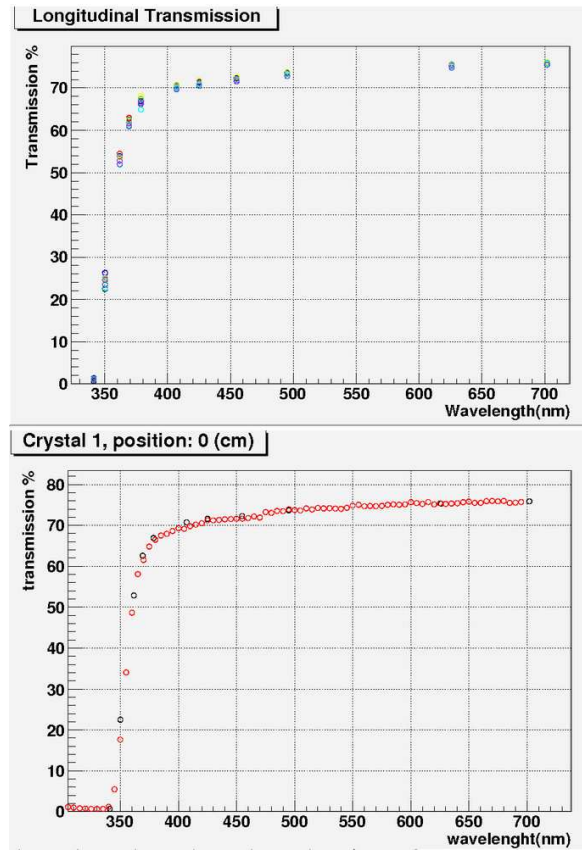


Figure 14: Longitudinal transmission (top) as measured with the ACCOS machine. In the bottom part of the figure, the ACCOS measurement (black) has been compared to a more precise spectrophotometer (in red).

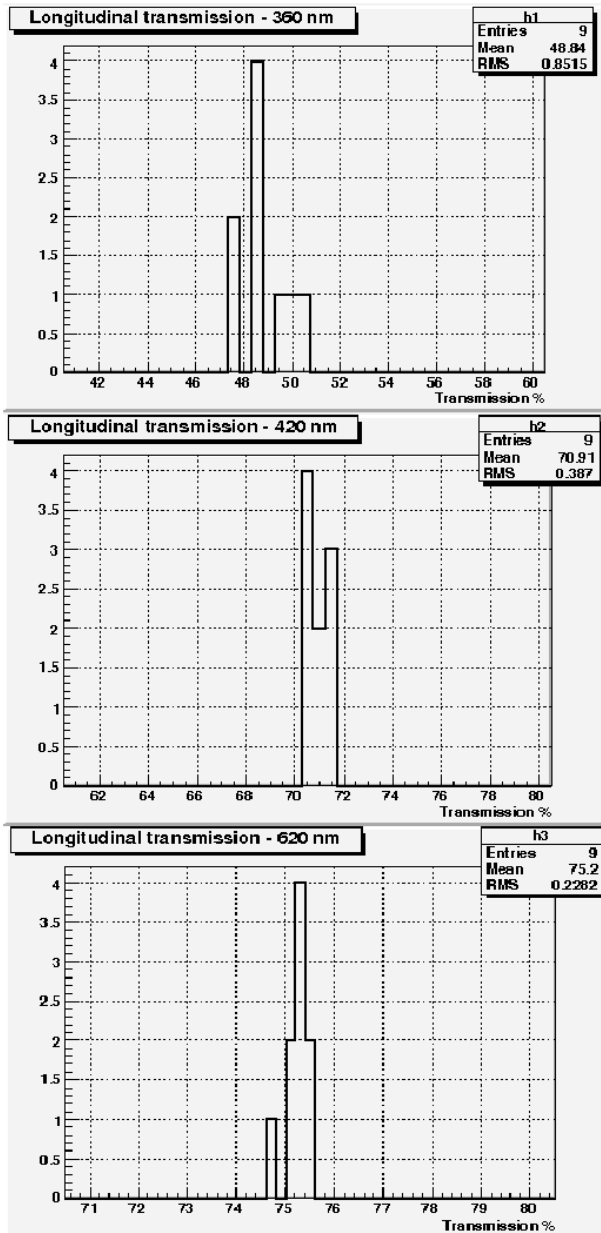


Figure 15: Distribution of the longitudinal transmission values for fixed wavelength values:  $\lambda=360$  nm, 420nm and 620 nm.

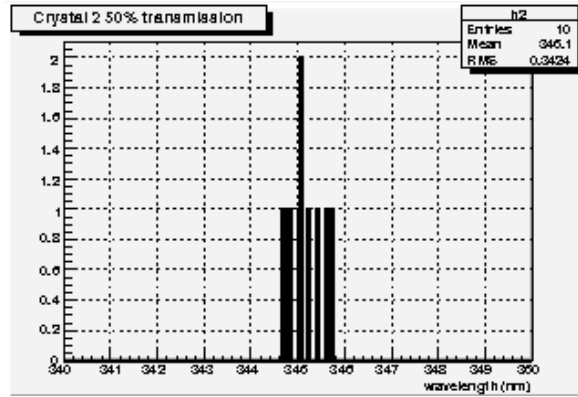


Figure 16: Wavelength distribution for a fixed value of transverse transmission  $T=50\%$ .

measured values (i.e. the dimensions of the *best-crystal*) and those of the "minimum" and "maximum" crystal. The dimensions of crystal 2 are different from those of the other crystal highlighting a damage, evident also by an eye survey, near the corners of both bases. All crystals are slightly smaller than the "nominal" ones (15 x 15 x 200 mm), reflecting the procedure used to cut and polish crystals at BTCP factory.

### Longitudinal transmission $T_L$

Figure 14-top shows the measured light transmission along the longitudinal axis as a function of the incident wavelength. All the 9 crystals show the same value of the optical transmission in the "plateau" region ( $T_L \sim 75\%$ ). The results obtained with ACCOS were cross-checked with a spectrophotometer with higher sensitivity ( $\delta\lambda = 5$  nm). Figure 14-bottom shows the comparison of the two measurement for one crystal: spectrophotometer in red and ACCOS in black. Results are the same on the "plateau" while a small difference in the region around 350 nm indicates a slight miscalibration of the ACCOS system in that region. Interpolating the previous measurement Fig. 15 show the distribution of the longitudinal transmission for a fixed wavelength  $\lambda=360$  nm, 420nm and 620 nm for the whole sample.

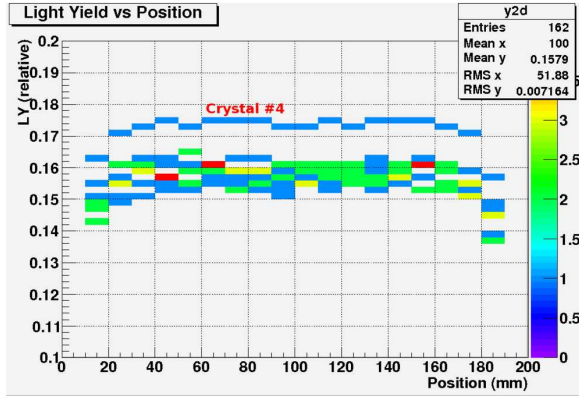


Figure 17: Relative light yield measured along the crystal n.4 longitudinal size.

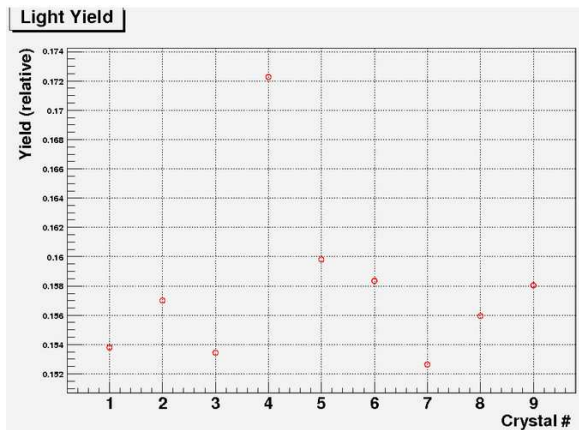


Figure 18: Average value of the relative LY for the 9 crystals in the sample.

**Transverse transmission  $T_T$**  To evaluate the uniformity of the transverse light transmission, Fig. 16 shows the wavelength distribution for a fixed value of  $T_T=50\%$ . The requirement of  $RMS \leq 3$  nm is fulfilled by every crystal in the sample. No requirements are placed on the absolute value of  $T_T$ .

**Light Yield  $LY_R$**  : The relative light yield has been measured, for each crystal in 12 points along the longitudinal size. As an example, Fig. 17 shows the results for crystal number 4. The mean value, for all crystals in the sample, is reported in Fig. 18. The relative  $LY_R$  is useful to check any significant difference between crystals.

### 2.1.3 Absolute Light Yield $LY_A$

The absolute light yield have been measured at room temperature using the CERN facility Bench 3 (B3). Measurement at different temperatures ( $T=+20$  °C and  $T=-20$  °C) with both radioactive sources and cosmic rays have been performed in our Lab.

**B3 measurement** A  $^{60}\text{Co}$  source was moved along the crystal longitudinal axis by means of a stepping motor The back face of the crystal was optically coupled to a PMT (Photonis XP2262B,  $QE \sim 25\%$ ) via a layer of optical glue ( $n=1.5$ ). The size of the PMT exceeded the size of the crystal to collect all the emitted light. A thermostat integrated in the bench kept the crystal temperature constant at 18 °C during the scan. The PMT signal, over a certain threshold, generated a 150 ns gate used to integrate the charge by a QVT unit working in Q-mode. The QVT analog output, was then converted to a 1024 bits digital value by a analog to digital converter and then transferred to a PC and shown as a multichannel spectrum. Pedestal in the spectrum was generated by a random pulse generator.

**Genova Lab measurement** The response of the crystals at different temperatures has been measured in Genova. The  $LY_A$  for one crystals was derived by using radioactive sources ( $^{60}\text{Co}$  and  $^{22}\text{Na}$ ) and cosmic muons. The crystal was read by different light sensors: a Photonis XP2262B tube and a Large Area APD Hamamatsu S8664-1010. During the measurement the temperature was kept constant at  $\pm 0.5^\circ\text{C}$ . The PMT was coupled by using a silicon optical pad and optical grease finding consistent results. The APD was glued to the crystal by optical cement. In all measurements, the crystal was wrapped by VM2000 on the free 5 faces. A test performed by using a different wrapping foil showed a  $LY_A$  deterioration of about 30%. The number of photo-electrons per MeV using the PMT set-

up with radioactive sources, was found to be:

- $N_{pe}/MeV=37\pm 4$  at  $-23^{\circ}C$ ;
- $N_{pe}/MeV=11\pm 1$  at  $+18^{\circ}C$ .

The response to cosmic rays of the PbWO-II crystal was measured as a function of the temperature from  $+18^{\circ}C$  to  $-25^{\circ}C$ . The DAQ was triggered using two plastic scintillators located above and below the crystal. The PMT signal was acquired with a QDC. For each temperature setting, the pedestal subtracted QDC spectrum was normalized to the single photoelectron charge to extract the number of photoelectrons; this was then divided by the most probable energy deposition for cosmic rays evaluated with GEANT4 simulations (16 MeV) to extract the light yield. The PMT single photoelectron signal was measured with the same DAQ system and QDC for each temperature to ensure the gain of the PM was not affected by the temperature variation. The distributions were fitted with a Landau function to extract the peak position. Results of the measurement are shown in Fig. 19. The LY extracted at  $+18^{\circ}C$  is about 20% higher than the one evaluated from the source measurements while the LY measured at  $-25^{\circ}C$  is consistent with the source measurement. The LY gain from  $+18^{\circ}C$  to  $-25^{\circ}C$  appears to be of the order of 2.5. The measurement with cosmic ray was repeated coupling the crystal to a LAAPD. The APD gain was kept constant at 150 changing the HV from 365V at  $+18^{\circ}C$  to 355.4 at  $-25^{\circ}C$ . The gain in LY from  $+18^{\circ}C$  to  $-25^{\circ}C$  appears to be of the order of 2.7, 10% higher than what found for PMT measurement. The number of photons emitted by the crystal were found to be:

- $N_{photons}/MeV = 121 \pm 10$  at  $+18^{\circ}C$   
( $N_{photons}/MeV/mm^2 = 0.54$ );
- $N_{photons}/MeV = 325 \pm 30$  at  $-25^{\circ}C$   
( $N_{photons}/MeV/mm^2 = 1.45$ );

to be compared to 0.7 photons/MeV/mm<sup>2</sup> obtained by our and PANDA measurement

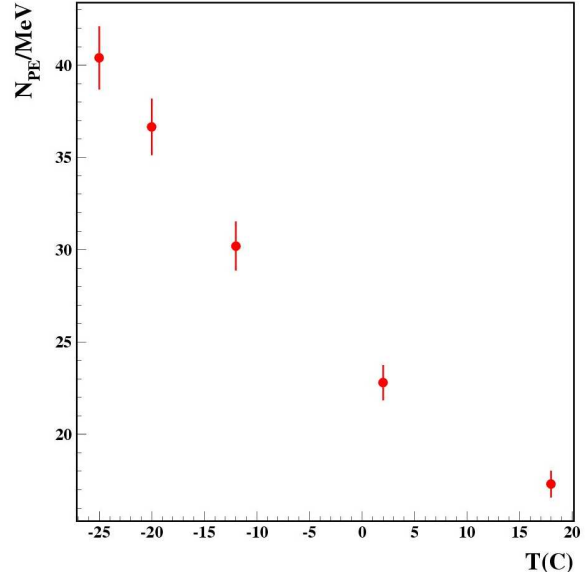


Figure 19: Light yield, in arbitrary unit, as a function of the operation temperature. Results when the LAAPD is glued to the crystal face are shown in black. The same but with an optical pad coupling are shown in green while results with PMT readout are shown in red.

at  $T=-25^{\circ}C$  using a PMT (see Ref. [23]).

These values were derived assuming the following parameters:

- APD Gain = 150;
- Preamp Gain = 1800;
- Deposited energy (from GEANT4 simulation) = 16 MeV;
- Measured charge = 26 pC at  $+18^{\circ}C$  and 70 pC at  $-25^{\circ}C$ ;
- APD QE = 70%;
- Area ratio =  $(10 \times 10)mm^2 / (15 \times 15)mm^2$ .

A summary of the different measurements performed in Genova is reported in Fig. 20.

#### 2.1.4 Decay time

Due to the expected high rate the crystals have to sustain, a fast response is mandatory to avoid pile-up effects or a degradation of the resolution for a partial light collection. The recent study of the kinetics of the

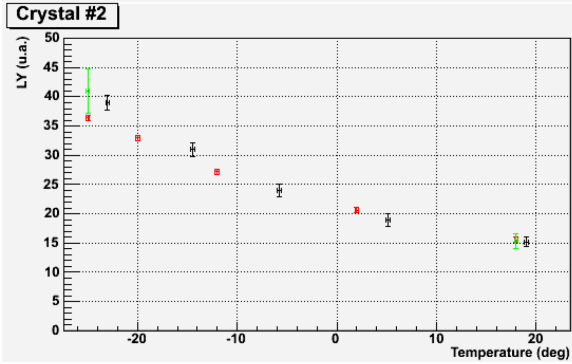


Figure 20: Light yield, in arbitrary unit, as a function of the operation temperature. Results when the LAAPD is glued to the crystal face are shown in black. The same but with an optical pad coupling are shown in green while results with PMT readout are shown in red.

PbWO revealed some rather complicated features of the luminescence decay. The process is non exponential and can be conventionally divided into three characteristic time intervals [29]. During the first 5-10 ns after the excitation, the luminescent intensity rapidly decreases by two orders of magnitude. The subsequent decay is slower, however, after 50 ns only a very small fraction of the total luminescence is still observable. The characteristic decay time of this superslow component has been reported to be between 500 ns and several microseconds.

We used two different methods to measure the decay time distribution of a SICCAS PbWO Type-II crystal:

1. Direct method. If a scintillation event is energetic enough and a significant number of photons are detected by the PMT, the PMT anode signal corresponds to the time distribution of the scintillation signal. It is a simple and direct method. The source of ionizing radiation can be a cosmic muon so that no radioactive sources are needed.
2. *Start-stop* or *delayed coincidence* method. The optical output of the scintillator is attenuated down to only record single

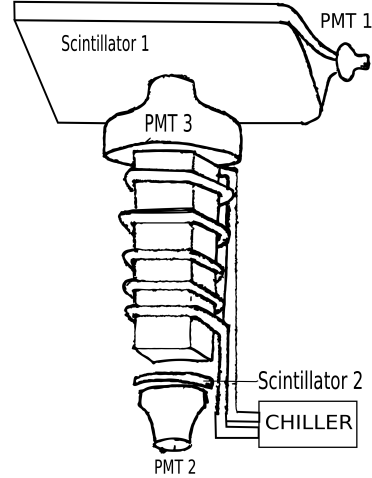


Figure 21: Experimental setup for direct measurement.

photon events. With this method, an additional *start* trigger is needed e.g. a fast scintillator. The trigger should be fast enough to provide the precise start time of the incoming muon. Since the rate of cosmic radiation is low, one may also use a  $\beta$  emitter with energy high enough to cross the trigger counter and reach the specimen scintillator. In this case the trigger counter is placed between the source the crystal. An alternative way is to use a radioactive source which emits one electron together with another electron or gamma ray in the opposite direction. In this case the source is placed between the trigger counter and the crystal. The advantage of using this second method relies on the fact that each photon arrival time is measured with high precision.

Measurements were performed at  $+23^{\circ}\text{C}$ ,  $0^{\circ}\text{C}$ . and  $-25^{\circ}\text{C}$ . We only report details of the direct method since results obtained with the *Start-stop* technique were found to be consistent. The measurement was performed with the crystal in a vertical position to obtain the maximum energy release. To control the geometry of the passing muons and to re-

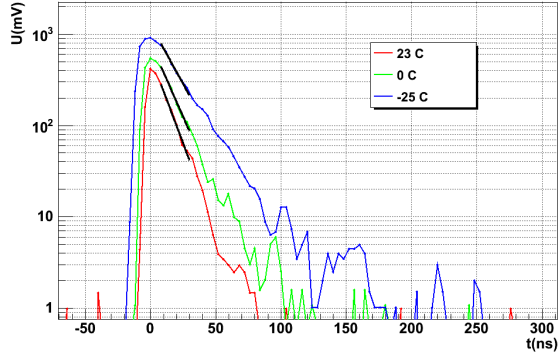


Figure 22: Three examples of PMT signals for a muon crossing. Signals are presented for three temperatures together with the one decay component fit (black lines).

duce the background two additional scintillator counters were placed on top and bottom of the crystal.

To maintain the desired temperature a 5 mm diameter tube with a coolant was wrapped around the crystal. The assembly was inserted in a plastic tube and sandwiched with two plastic scintillator counters. The scheme is presented in Fig. 21.

The three signals, one from the PbWO crystal and two from the scintillator counters were put in coincidence. This allows to detect vertical cosmic muons passing through the setup and releasing energy in the PbWO crystal and producing a sufficient amount of light to measure the arrival photon time distribution. All PMT signals were split into two equal parts: one was used to set the trigger while the other was fed to a CAEN digitizer V1720: 8 channels, 250 MHz sampling rate, 2 V range and precision better than 0.5 mV. Thresholds for the discriminators were set to be about half of the typical signal induced by a muon crossing. The discriminator outputs were connected to a logic board where the three signals were *AND*ed.

For a vertically crossing muon, a deposited energy in the crystal of about 200 MeV is expected. Considering the SICCAS crystal's

T ( $^{\circ}$ C)	$\tau_{fit}(ns)$	$\tau_{int}^1(ns)$	$\tau_{int}^3(ns)$
23	$10.5 \pm 1.2$	$8.4 \pm 1.5$	$11.3 \pm 0.2$
0	$13.5 \pm 0.6$	$11.6 \pm 0.5$	$13.0 \pm 0.2$
-25	$19.8 \pm 0.6$	$14.5 \pm 0.5$	$20.2 \pm 0.3$

Table 5: Results of the measurements for the three different temperatures using the one decay component fit and the two integral methods - for  $\tau$  and  $3\tau$ .

LY, one should expect from 4000 to 20000 photons for temperatures ranging from  $+23^{\circ}$  C to  $-25^{\circ}$  C. An additional attenuation factor should be considered to account for the light collection geometry. A threshold of about 500 p.e. was set to the PMT together with a rather high threshold for PMTs attached to the plastic scintillators to suppress background. A check on the time difference between the three peak positions was also implemented to further reduce the background. The measurements were performed for three different temperatures:  $+23^{\circ}$  C,  $0^{\circ}$  C and  $-25^{\circ}$  C. The temperature was measured by a thermocouple attached to the crystal. As crosscheck the T of the cooling liquid was also measured. The number of accepted events was greater than 10 for every temperature corresponding to one day of data acquisition. Three examples of digitized signals are reported in Fig. 22. The fit were performed with the hypothesis of one and two decay components. Results were consistent with a single component. As a crosscheck, the decay time  $\tau$  for a pure exponential decay was also extracted from the area of the signal, calculated from 0 to  $\tau$   $A(0 \div \tau) = (1 - e^{-3})A_{tot}$ .

Results are summarized in table 5. One can see that the value of  $\tau$  derived with the two methods are consistent within the error. However  $\tau$  from the  $A(0 \div \tau)$  area is systematically smaller. This can be ascribed to the distribution shape that differs from an exponential function. The delay time increases by a factor of two when T changes

from  $+23^{\circ}\text{C}$  to  $-25^{\circ}\text{C}$ , remaining within a reasonable window. In all cases the requirement  $LY(100\text{ns})/LY(1000\mu\text{s}) > 90\%$  is fulfilled.

### 2.1.5 Quality requirements and control

The FT-Cal requires 332 PbWO-II crystals (+ 10% spares) for a total of 370 crystals. The envisaged high performance of the detector imposes strict requirements on the crystal parameters, such as sufficient and uniform light yield, short decay time, very limited light yield loss under irradiation and finally precise geometrical dimensions. A detailed list of specifications is reported below.

#### General properties

- Crystal dimensions: all crystals are identical with a parallelepiped shape  $200 \times 15 \times 15 \text{ mm}^3$  (tolerance  $+0/-0.15 \text{ mm}$ )
- All faces are polished with a roughness of  $R_a \leq 0.02 \mu\text{m}$

#### Optical properties

- Longitudinal transmission (absolute values):
  - $\geq 35\%$  at  $360 \text{ nm}$
  - $\geq 60\%$  at  $420 \text{ nm}$
  - $\geq 70\%$  at  $620 \text{ nm}$ ;
- The non-uniformity of the transverse transmission  $Tr$  at the transmission value of  $Tr = 50\%$  has to be  $\delta\lambda \leq 3 \text{ nm}$  for 4 measurement every 4 cm. The first one is at 1.5 cm from the front face.
- Light Yield  $LY \geq 13 \text{ phe/MeV}$  at  $T=18^{\circ}\text{C}$ ;
- Light Yield when cooled:  $LY (T=-25^{\circ}\text{C}) \geq 3.0 \text{ LY} (T=+18^{\circ}\text{C})$ ;
- Decay Time  $LY(100\text{ns})/LY(1000\text{ns}) > 90\%$  at  $T=18^{\circ}\text{C}$  and  $T=-25^{\circ}\text{C}$ .

**Radiation Hardness** Radiation hardness is evaluated by measuring the induced optical absorption in crystal along its axis after irradiation with a predefined dose and dose rate.

- The crystal is kept at  $T=(20\pm 5)^{\circ}\text{C}$  between irradiation and completion of the measurements;
- Irradiation will be performed placing a  $^{60}\text{Co}$  source on the side of the crystal. The total accumulated dose should be of  $3 \text{ kRad}$ , at a dose rate of  $5\text{-}50 \text{ kRad/h}$ .
- The Induced absorption of the crystal should not exceed  $\Delta k \leq 1.0 \text{ m}^{-1}$  at  $\lambda=420 \text{ nm}$ .
- The mean value of the  $\Delta k$  distribution of each lot and based on the measurement of not less than 50% of the lot should be  $\Delta k_{Average} \leq 0.75 \text{ m}^{-1}$ .

**Certification** General properties, optical properties, and radiation hardness of all crystals will be tested by the manufacturer. A certification of specification-compliance will be released and sent with the crystals. After delivery, we will carry out an independent certification concerning general and optical properties of crystals using the ACCOS facility at CERN and will run radiation hardness tests.

## 2.2 Photo-detectors

### 2.2.1 APD

Avalanche Photodiodes (APD) are reverse-biased diodes with an internal high electric field used to multiply the charge carriers through an avalanche mechanism. In past years, a lot of studies have been done by Hamamatsu Photonics to build an APDs suitable for PbWO<sub>4</sub> crystal, leading CMS and PANDA experiments to chose these APD as the optical sensors in their electromagnetic calorimeters [23], [31].

There are many advantages in using APDs: small sizes, high quantum efficiency ( $\simeq 70\%$  in the region of the PbWO<sub>4</sub> emission) and,



Figure 23: The Hamamatsu Photonics s8664-1010 Large Area APD.

most important, unsensitivity to magnetic fields. The main disadvantage is that, due to the low gain, the output signal is too small to be directly acquired, and needs to be amplified by a suitable circuit. APDs also need to be operated at controlled temperature to avoid variations in gain and noise.

Hamamatsu Photonics made commercially available a large-area APD (Fig. 23), with an active area of  $10 \times 10 \text{ mm}^2$  (model S8664-1010) that could fit the requirements of the FT-Cal.

**The APD layout** Figure 24 shows the working principle of an APD: the incident photons enters crossing a N layer and moves across the P layer, producing electron-hole pairs into the depletion region. If a reverse bias is applied to the APD, the high electric field in the depletion region multiplies the charge-carriers by impact ionization, giving an avalanche gain. Electrons are then collected in the N layer, while holes are collected in the P layer: a current proportional to the intensity of the incident light flows across an external circuit

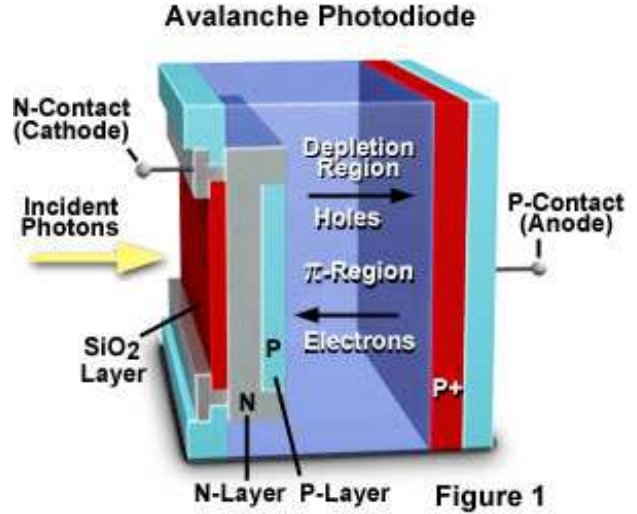


Figure 24: Scheme of an APD.

connected to the two junctions. Figure 25 shows the equivalent circuit of an APD, similar to the equivalent circuit of a standard photodiode.  $C_J$  is the intrinsic capacitance of the APD,  $R_{SH}$  is the shunt resistor and  $R_S$  is the series resistance: typically,  $R_S$  is a few ohms, while  $R_{SH} \simeq 10^7 - 10^{11} \Omega$ .

The relation between the currents is the following:

$$I_3 = I_0 - I_1 - I_2$$

$$I_3 = I_0 - I_s \cdot \left( \exp\left(\frac{q_e V_d}{KT}\right) - 1 \right) - \frac{V_d}{R_{SH}} \quad (1)$$

The detector capacitance  $C_J$  has to be taken into account to determine the cut-off frequency of the system when connecting the APD to an external load or circuit (with input resistance  $R$ ): it adds a pole to the transfer function of the whole system, at a frequency  $f_{cut} = \frac{1}{2\pi RC_J}$ .

**Internal Gain** The APD dark current  $I_d$  and intrinsic gain  $G$  strongly depend on the temperature, due to the interaction of the charge carriers with phonons: increasing the temperature the gain becomes smaller. To measure the internal gain  $G$  at fixed temperature  $T$  as a function of the bias voltage we

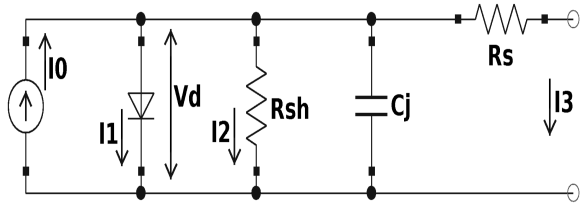


Figure 25: Equivalent electric circuit of an APD.  $I_3$  is the current across the external load.

used the following procedure: we measured the dark current  $I_{off}$  and the current due to a continuous illumination  $I_{on}$  at different values of the reverse bias voltage  $V_B$ . As a light source we used a blue LED, with an emission peak similar to the maximum emission wavelength of  $\text{PbWO}_4$  (420 nm): the stability of this source was checked using a stable PMT and measuring the output current while exposed at the LED light. We did not see any appreciable variation during a measurement period of several hours. We calculated the gain through the following relation:

$$G(V_B) = \frac{I_{on}(V_B) - I_{off}(V_B)}{I_{on}(G=1) - I_{off}(G=1)} \quad (2)$$

$I_{on}(G=1)$  and  $I_{off}(G=1)$  are, respectively, the value of the current due to the incident light and the value of the dark current when the internal gain of the APD is equal to 1, i.e. when the avalanche mechanism is not present: these values must be measured independently to know the gain  $G$ . Figure 26 shows the behavior of  $I_{on}$  and  $I_{off}$  as a function of the bias voltage. For low values of the bias voltage that the dark current is smaller than the current under illumination (the ratio is  $\simeq 1000$ ) and the current under illumination is constant and does not depend on  $V_B$ . It's possible to calculate  $I_{on}(G=1)$  and  $I_{off}(G=1)$  considering only the values of

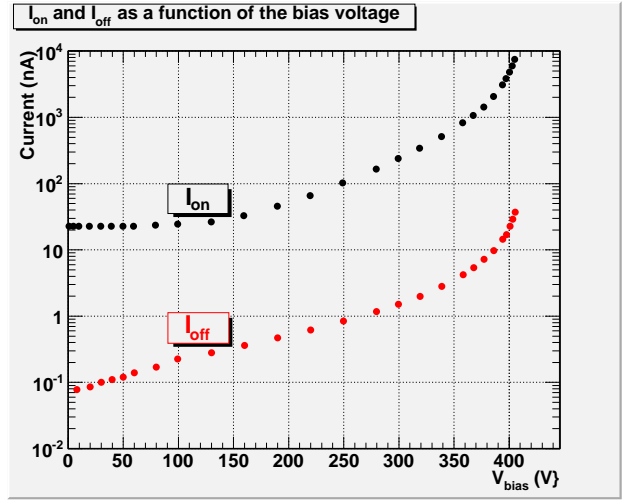


Figure 26: Behavior of  $I_{on}$  and  $I_{off}$  as a function of the APD bias voltage.

the currents measured for  $V_B < 50$  V, performing two best-fits with linear functions.  $I_{on}(G=1)$  and  $I_{off}(G=1)$  are the intersections of these functions with the y-axis. The experimental result of the measure on one of the APDs is reported in Fig. 27. A stand-alone HV source was used to bias the detector, and a pico-amperometer (KEITHLEY Model 6517A) was used to measure the current from the APD. This measure was done at a fixed temperature of  $18.5^\circ$ . We also studied the dependence of the gain from temperature: results are shown in Fig. 28.

In first approximation we can parametrize the gain dependence on the bias voltage  $V_B$  and on temperature  $T$  with a linear combination:

$$G(V_B, T) = G(\alpha V_B - \beta T) \quad (3)$$

Performing a best-fit using a simple exponential function for  $G$ , we derived  $\alpha =$  and  $\beta =$ . The relative dependence of the gain from temperature and from bias voltage is then given by these simple relations:

$$\frac{1}{G} \frac{\partial G}{\partial V_B} = \alpha \quad (4)$$

$$\frac{1}{G} \frac{\partial G}{\partial T} = -\beta \quad (5)$$

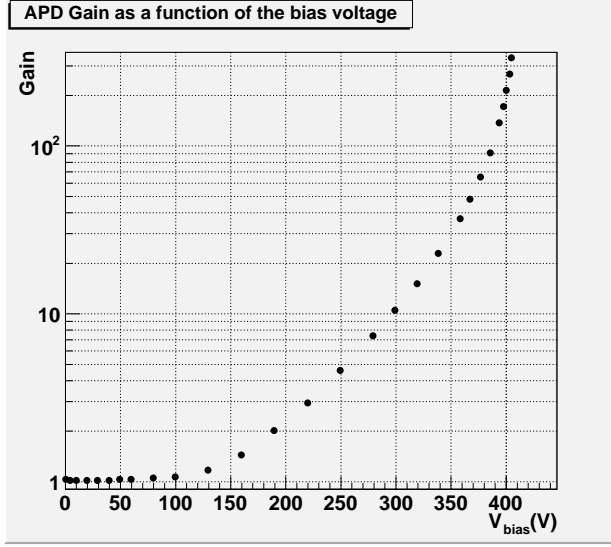


Figure 27: APD intrinsic gain  $G$  as a function of the bias voltage.

At room temperature we measured  $\frac{1}{G} \frac{\partial G}{\partial V} = 3.9\%$  for  $G = 50$ , in agreement with similar data from CMS [32] and PANDA [23]. We also measured the gain dependence from temperature founding:  $\frac{1}{G} \frac{\partial G}{\partial T} = 3.3\%$ .

**Dark Current** The dark current is due to two different contributions: the bulk current  $I_b$  and the surface current  $I_s$ . The latter is independent from the APD intrinsic gain  $G$ , while the first increases with  $G$ , since it undergoes the charge multiplication inside the depletion region. The total dark current is the sum of these terms:

$$I_d = I_b + I_s = I_b + I_{s0} \cdot G$$

The dark current behavior as a function of the gain, is reported in Fig. 29 for room temperature. The data show clearly a linear relation between these two quantities, in agreement with the predictions of a model of the dark current.

**Facility for APD Gain Measurement** In anticipation of the construction of the full FT-Cal detector we have developed in Genova a facility for the automatic measurement of the

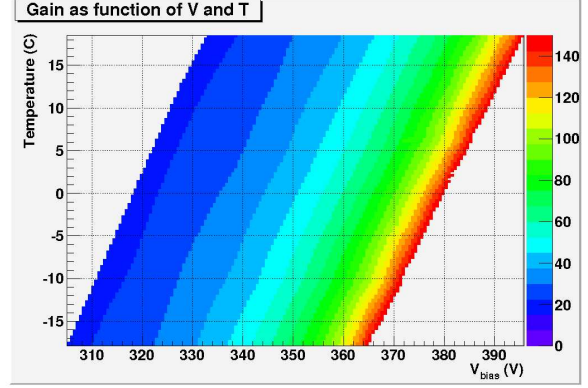


Figure 28: Intrinsic gain of one APD as a function of the bias voltage and of the temperature.

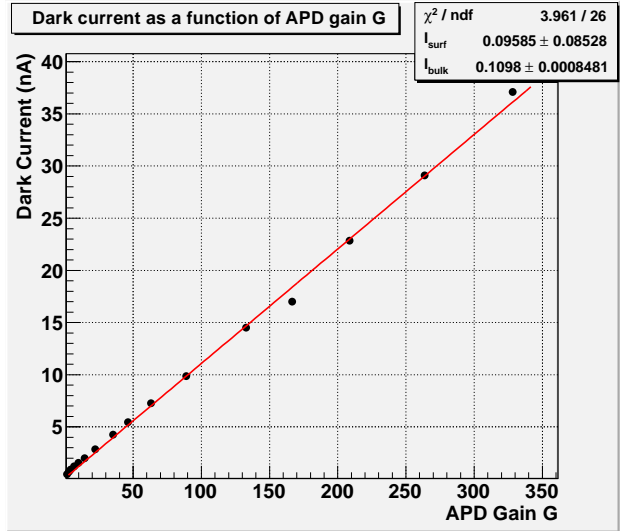


Figure 29: Dark current of the APD as a function of the intrinsic gain  $G$ .

intrinsic gain and dark current of APDs, as a function of bias voltage and at different operating temperatures. This facility can measure up to 24 APDs at once: the full measurement for each temperature takes  $\sim 5$  hour, and the full characterization within 1 day. The full set of  $\sim 400$  APDs will be measured with this facility in less than 20 days.

The facility operates as follows: the gain of each APD is measured with the DC technique already described in the previous two paragraphs. However, only one high-voltage source and one pico-amperometer are used for the whole setup. Both these devices are embedded in a electrometer, KEITHLEY Model 6517A. During operations, the 24 APDs are all biased with the same HV: the HV source of the electrometer is connected to the APD cathodes via independent bias resistors (see Fig. 30 for a schematic). The photo-detector anodes are connected to the inputs of a current multiplexer, that feeds only one of them at time to the input of the electrometer, while keeping the other 31 to ground.

The current multiplexer (see Fig. 31 for a picture) is the “core” of the facility: it has been customly designed in Genova, using mechanical relays (type SPDT) as switches. Relays have been chosen because the currents from the APDs that are measured are of the order of 10–100 nA. All other kinds of switches would introduce a leakage current of the same order, leading to a wrong gain measurement. Tyco “T7SS5E4-12” relays have been chosen for this application, due to their high isolation between the two outputs and the PCB mounting. They are operated trough a dedicated chip (ULN2003A). The APDs are mounted on two drilled copper plates, that keep them at constant temperature: a pipe connected to an external chiller is welded on each of the two plates to provide the necessary cooling. Both plates host 12 APDs. Each of them is mounted in correspondence of a hole, and is connected trough a dedicated connector to a PCB mounted on the opposite side

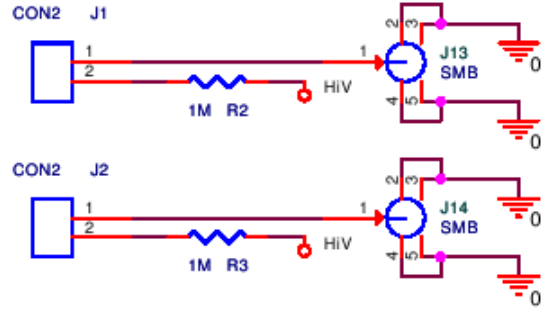


Figure 30: Schematic of the APDs bias circuit of the facility for APD Gain Measurement, for two channels. HiV is the common bias voltage of the two APDs, that are connected trough CON2 connector (1: anode, 2: cathode).

of the plate. This PCB distributes the HV bias to each APD and feeds their currents to the input of the current multiplexer. Figure 32 shows one of the two plates, with two APDs already mounted. During the operations the two holding plates are inserted in a dark and vacuum-tight box, flushed with  $N_2$  to prevent moisture formation. The whole system is controlled via Labview, to keep the interaction with the user as simple as possible. The user can choose the temperature set and select, independently for each measurement, which HV values have to be use during the DC scan. Data are analyzed with a ROOT macro, using the same procedure described in the previous paragraphs, to obtain the intrinsic gain  $G$ . Relevant parameters, as the bias voltage corresponding to a gain of 150 at room temperature and the relative variation of the gain respect to the temperature and the bias voltage in the neighborhood of the nominal working point, are recorded in a file.

For a deposited energy  $E$  in the  $PbWO_4$  crystal,  $N_\gamma = \varepsilon \cdot E$  photons hit the APD surface where  $\varepsilon$  is the product of the LY and the geometrical coupling between crystal and the APD. This leads to  $N_e$  primary charge-carriers in the APD, via a statistical process

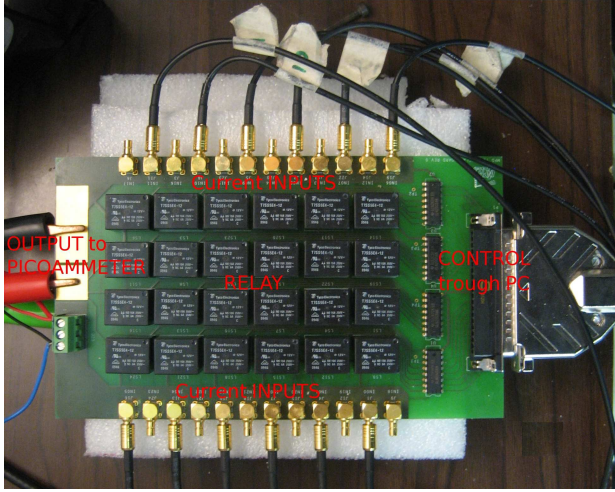


Figure 31: The current multiplexer of the facility for APD Gain Measurement.

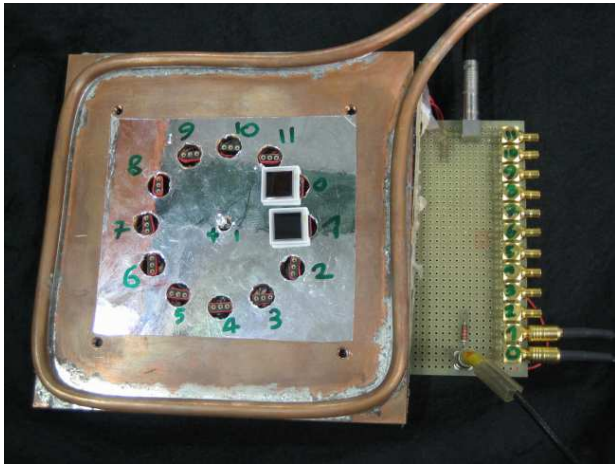


Figure 32: The metallic plate hosting APDs in the facility for APD Gain Measurement. A prototype of the PCB that distributes HV and collects signal from the sensors is mounted on the back of the plate.

with standard deviation  $\sigma_{N_e} = \sqrt{N_e}$ . Subsequently each of these charges undergoes to an independent avalanche multiplication process. Fluctuations in gain  $\sigma_G$  are then related to inhomogeneities in the gain region: this gives another contribution to  $\sigma_G \cdot \sqrt{N_e}$  [33]. The energy resolution is given by the sum of all these contributions:

$$\frac{\sigma_Q}{Q} = \frac{\sigma_E}{E} = \frac{1}{\sqrt{N_e}} \cdot \frac{\sqrt{G^2 + \sigma_G^2}}{G} \equiv \frac{F}{\sqrt{N_e}} \quad (6)$$

**Excess Noise Factor  $F$**  The excess noise factor  $F$  is introduced into the usual parametrization of energy resolution to take into account the effect of gain fluctuation. We measured the excess noise factor  $F$  for one APD using, as light source, a YAP pulser coupled to the detector through an optical pad (Saint-Gobain BC-634A,  $n=1.42$  @ 400 nm). The APD was read using an amplifier developed for the CLASIC IC detector, with a nominal gain in charge  $G_c \equiv 2600$  [24].

To measure  $F$  we used the following procedure:

1. We measured the output charge  $Q$  and its fluctuations  $\sigma_Q$  from the APD as a function of the bias voltage  $V_B$ . We also measured the contribution to the resolution given by the electronic noise, measuring the charge fluctuations  $\sigma_{Q_n}$  out of time respect to the signal.
2. We estimated the number of primary  $e^- - h^+$  couples  $N_e$  from the charge measure performed at the nominal gain of the APD. We calculated the APD intrinsic gain for each measure using  $G = \frac{Q}{q_e \cdot N_e}$ .
3. For each measure, we calculated the *true* statistical resolution subtracting the contribution of the noise:
$$\sigma_{Q_{real}} = \sqrt{\sigma_Q^2 - \sigma_{Q_n}^2}.$$
4. We calculated  $F$  via eq. 6:

$$F = N_e \cdot \left( \left( \frac{\sigma_{Q_{real}}}{Q} \right)^2 - (\delta_{YAP})^2 \right)$$

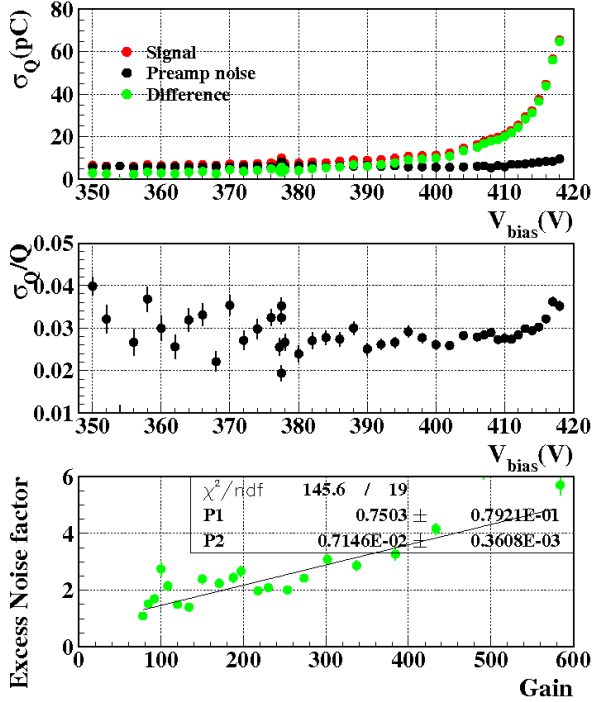


Figure 33: Top: measured charge fluctuations of signal and background, and their difference. Center: relative resolution as a function of the bias voltage. Bottom: excess noise factor  $F$  as a function of the APD intrinsic gain  $G$ .

In the formula above,  $\delta_{YAP}$  is the contribution to the relative resolution from the YAP pulser, assumed to be 2.2 %.

Final results are reported in Fig. 33. We obtained  $F = 1.29$  for  $G = 50$  and  $F = 1.8$  for  $G = 100$ , in good agreement with the measurement from PANDA [23].

### 2.2.2 SiPM

Silicon Photomultipliers (SiPM), also called Multi-Pixel Photon Counters (MPPC), were possible candidates as optical sensors in the FT-CAL thanks to their compact size, insensitivity to magnetic field, active surface that goes from 1 mm<sup>2</sup> for single sensors to more than a cm<sup>2</sup> for sensor arrays. Because of their high gain, SiPM are known to be sensitive to a single photon. In addition, sensors with large number of pixels should provide

Parameter	Measure Conditions	Value
Active Area (mm <sup>2</sup> )		10 x 10
Quantum Efficiency	$\lambda = 420$ nm	70%
Spectral Response Range		320 to 1000 nm
Intrinsic Capacitance $C_J$		270 pF
Dark Current $I_d$	$G=50, T=20^\circ$	5 nA
Excess Noise Factor $F$	$G=50, T=20^\circ$	1.29

Table 6: Hamamatsu Photonics Large Area APD main characteristics.

the necessary dynamical range. In Genoa we performed some tests on selected sensors produced by Hamamatsu Photonics, model SiPM S10931-025P. This SiPM is characterized by an active surface of  $3 \times 3$  mm<sup>2</sup> subdivided into 14400  $25 \mu\text{m}$  pixels. The effective quantum efficiency is  $\simeq 25\%$ .

**SiPMs layout** A SiPM can be viewed as an array of avalanche photodiodes detectors (APDs) working in Geiger-Mode, i.e. with a self-sustaining avalanche process, characterized by a positive feedback mechanism. The detector produces an avalanche current (limited by a series resistor) when a photon hits one channel and it is converted into an electron-hole pair. A quenching mechanism is implemented into the device to switch off this current and let the SiPM channel detect another photon. The equivalent electric circuit of a single SiPM channel is reported in Fig. 34.  $C_D$  is the internal capacitance,  $R_Q$  is the resistor that provides the quenching mechanism and  $R_S$  is the series resistor that limits the current flowing into the detector. Typically,  $R_S \simeq 1k\Omega$  and  $R_Q \simeq 300k\Omega$ .  $V_{BD}$  is the intrinsic potential of the P-N junction, and  $V_{BIAS}$  is the external voltage source used to polarize the SiPM:  $V_{BIAS} > V_{BD}$ .

The *switch* takes into account the avalanche mechanism, that corresponds to the “close” state: the transition between the “open” and “close” states is characterized by two parameters.

- $P_{01}$  is the *trigger probability*, i.e. the probability that an incoming photon initiate the avalanche mechanism. This

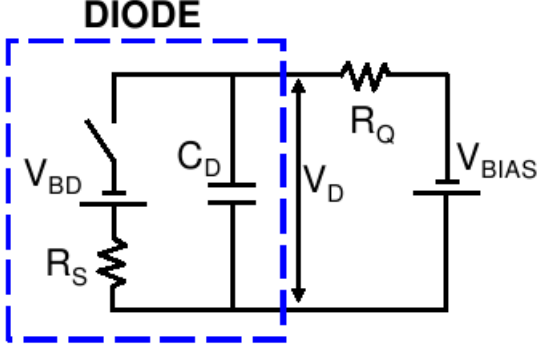


Figure 34: Equivalent electric circuit of a single SiPM channel.

parameter is related to the internal structure of the SiPM and strongly effects the quantum efficiency of the device.

- $P_{10}$  is the probability to quench the avalanche mechanism by a statistical fluctuation to zero of the number of carriers into the high-field region.

The time evolution of the output signal for a single channel after a photon detection (at time  $t_0$ ) can be divided into 4 steps:

1.  $t < t_0$ : there's no avalanche. The switch is open,  $C_D$  is charged to  $V_{BIAS}$  and there's no current flowing across  $R_Q$ .
2.  $t = t_0$ : the avalanche starts. The switch closes, and  $C_D$  discharges across  $R_S$  until it reaches the  $V_{BD}$  potential, with a time constant  $\tau_1 = R_S \cdot C_D$ .
3.  $t = t_1$ : the quenching mechanism stop the avalanche. The switch opens and  $C_D$  recharges to  $V_{BIAS}$  with a time constant  $\tau_2 = R_Q \cdot C_D$ .
4.  $t > t_2$ : the quenching mechanism is over. The switch is open, there's no current flowing across  $R_Q$ .

The output signal from the whole detector is just the sum of the signals from each channel.

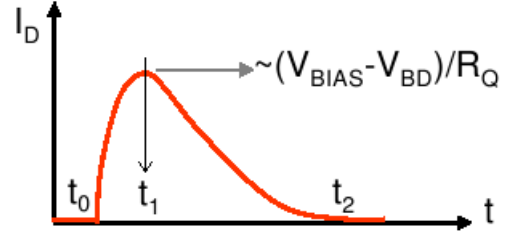


Figure 35: Time evolution of the electric signal from a SiPM channel:  $I_D$  is the current across the quenching resistor.

**Photon counting and saturation** Since in a SiPM each channel is working in Geiger Mode, it produces the same output signal independently of the number of photons hitting it: this fact introduces some non-linearities when reconstructing the intensity of the incident radiation. When a SiPM with  $N_c$  cells and quantum efficiency  $\varepsilon$  is hit by  $N_{ph}$  optical photons the number  $n$  of interactions that can lead to the avalanche in each cell is a Poisson distribution with mean number  $N_{ph} \cdot \varepsilon N_c$ :

$$P_n = \frac{\exp(-\frac{N_{ph} \cdot \varepsilon}{N_c}) (\frac{N_{ph} \cdot \varepsilon}{N_c})^n}{n!} \quad (7)$$

Consequently, each cell can produce its signal with probability given by:

$$P_{cell} = (1 - P_0) = 1 - \exp(-\frac{N_{ph} \cdot \varepsilon}{N_c}) \quad (8)$$

The distribution of active channels in the whole SiPM is binomial, with mean value given by:

$$N_{ON} = N_C \cdot P_{CELL} = N_C \cdot (1 - \exp(-\frac{N_{ph} \cdot \varepsilon}{N_c})) \quad (9)$$

From eq. 9, the relation between the number of incoming photons and firing cells is linear as long as  $N_{ph} \ll N_C$ : for higher intensi-

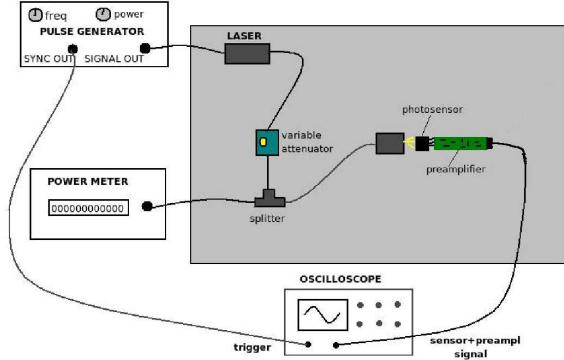


Figure 36: Schematics of the experimental setup for the measure with SiPM.

ties, a non-linear relation holds.

We measured the response of the Hamamatsu S10931-25P SiPM as a function of the incident light intensity: the measurements were performed using a laser as light source with the setup shown in Fig. 36. The experimental setup consists of:

- a Hamamatsu Photonics K.K. M 10306-06 laser. The laser power is 63mW with a pulse duration of 101 ps. The laser wavelength is centered at 439 nm, well matched to the emission spectrum of the  $\text{PbWO}_4$  crystals that will be used in the FT calorimeter. The laser controller allows to vary the power and the laser pulse rate, providing an external trigger signal through the SYNC OUT connector;
- optical fibers, splitters and mechanical supports to convey the light from the laser to the sensor under test and to a power meter (Newport M 2930 C) located outside the box;
- a variable attenuator (Crisel Instrument SRL BB-500-11-440-50/125-M-35-33-3-1-ND) inserted between the laser and the light sensor in order to vary the light intensity. The attenuator is matched to the wavelength of the laser light and operates from 0 to -40 dB.

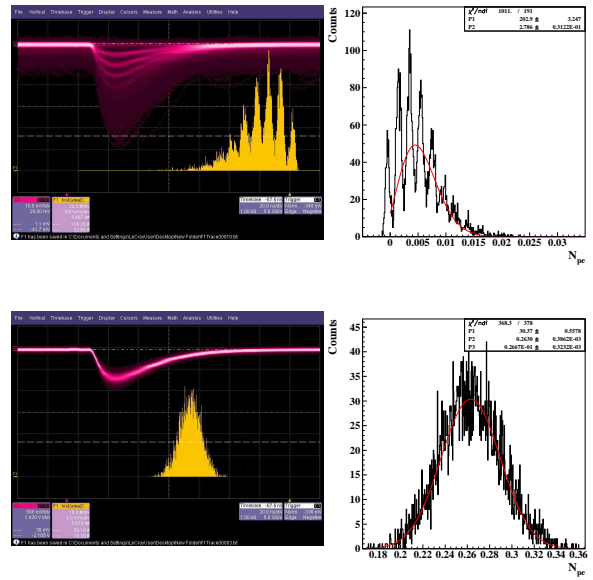


Figure 37: S10931-025P digitized signal (left) and intensity distribution for low light intensity (top) and high light intensity (bottom).

The light from the laser goes through the variable attenuator and then through a splitter. One of the outputs is connected to the power meter to monitor the light intensity and the other to the light sensor. The power measurement is performed setting the laser pulse rate to 100 MHz while for, the actual measurement, this is lowered to 1 kHz to have well-separated light pulses. The light sensor and the preamplifier are located in front of one of the optical fibers with the light spot comparable to the sensor surface. The preamplifier used in this tests was originally designed by IPN-Orsay and used for the the readout of the APDs of the CLAS Inner Calorimeter [24]. For our tests, it has been modified reducing the gain by a factor 30 to match the higher gain of SiPM. For each given setting of the variable attenuator and therefore of the light intensity, the signal from the SIPM is measured with a LeCroy digital oscilloscope using the laser SYNC OUT signal as trigger. The digitized signals are integrated and recorded for a later analysis. Measurements were performed from about 4 nW, corresponding to a number of incident photon of the order of 10, to 200 nW corresponding to several hundreds

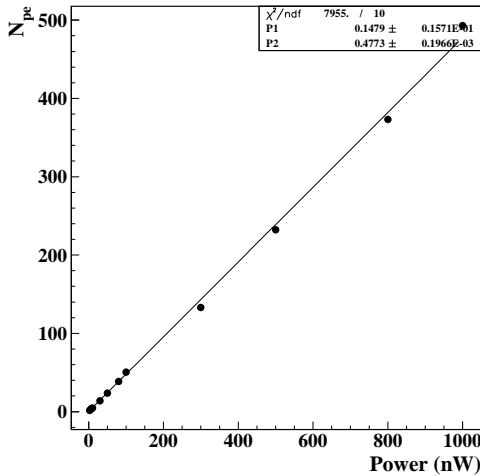


Figure 38: Average number of pixel firing as a function of the laser light power for the S10931-025P sensor.

photons. Measurements at higher power could not be performed because of the saturation of the preamplifier. Examples of the sensor signal and charge distribution are shown in Fig. 37 for low and high light intensity: clear and separated peaks corresponding to single pixel signal, are visible at low intensity, while the charge distribution becomes smooth at high intensity. The single pixel signal was therefore extracted from the low light-intensity signal with a Gaussian fit, where the mean value was used to transform the measured charges into number of firing pixels.

The charge distribution was fitted to a Poisson function up to a light power of the order of 20 nW. For higher power, a Gaussian fit was performed. The possible systematic difference between the Poisson and Gaussian fits was studied and found to be negligible. The result is shown in Fig. 38: the measurements are consistent with linear slope as expected. It should be noted that the errors shown on the graph correspond to the uncertainty on the average pixel number given by the Poisson or Gaussian fits. Systematic errors due to the light power measurement should also be included for a more accurate error evaluation.

Parameter	Measure Conditions	Value
Fill Factor		30.8
Active Area (mm <sup>2</sup> )		3 x 3
Quantum Efficiency	$\lambda = 420$ nm	25%
Spectral Response Range		320 to 900 nm
Intrinsic Capacitance $C_J$		320 pF
Dark count	T=25 <sup>o</sup> , 0.5 phe threshold	4 MHz
Gain		$2.75 \cdot 10^5$

Table 7: Hamamatsu Photonics S10931-025P MPPC tech specs.

This additional contributions are larger than the deviation of the measured points from the linear function. The maximum number of pixel firing is of about 500 for a light power of 1  $\mu$ W. Considering that the quantum efficiency of this sensor is expected to be of the order of 25%, the number of incident photons can be estimated to be of  $\sim 2000$ . This number is still fairly small with respect to the number of pixel of this sensor and therefore the good observed linearity is consistent with expectations. For the Gaussian fits, an additional check was performed comparing the  $\sigma$  from the fits with the fluctuations expected based on the fitted pixel number. For a pure stochastic process, the  $\sigma$  of the Gaussian is in fact expected to be equal to  $\sqrt{N_{PE}}$ . The data are consistent with this condition with 10%.

subsubsectionLAAPD vs SiPM After considering the different advantages and disadvantages of APD and SiPM, we decided to use the LAAPD. The main reason is related to the unknown tolerance of SiPM to radiations. APDs requires a more complex signal processing, higher gain preamplifier, better noise shielding etc., but this technology has proved to work pretty well for CMS and IC-Cal and is the same chosen by the PANDA-EC.

## 2.3 FE & RO electronics

### 2.3.1 The Orsay preamplifier: FT-Orsay

The APD current signal is converted to a voltage pulse which is transmitted to the subsequent electronics chain via a trans-impedance



Figure 39: Front and rear view of an amplifier board.

amplifier (i.e. an amplifier which converts an input current pulse into an output voltage pulse, without performing any time integration). This amplifier has been developed in collaboration with the “Service d’Electronique Physique” (SEP) of the “Institut de Physique Nucleaire” (IPN) in Orsay.

**Circuit Description** The schematic of the amplifier, excluding the HV bias network, is shown in Fig. 40. The first stage is based on a BJT NPN transistor in a common-base configuration, while the second and the third are based on operational amplifiers in a non-inverting configuration. The two BRF182 have been chosen since they are low noise bipolar transistors (the noise figure  $F$  is 0.9dB for  $I_c = 2$  mA at 900 MHz), with a high cut-off frequency. The DC characteristics of the first stage can be easily calculated neglecting the small base current ( $I_b \simeq 0$ ) and therefore  $I_e = I_c$ . Since the base is connected to the ground, the emitter voltage  $V_e$  is equal to the base-to-emitter drop-off  $V_{be} = -0.76V$ . The emitter current is then given by  $I_e = \frac{V_{EE} - V_e}{R_e} = 630\mu A$ , and equal to the collector current  $I_c$ . A current pulse at the input corresponds to a variation in the emitter current  $i_e$ . Considering that the variation in the collector current  $i_c$  is the same, the voltage signal at the collector is given by:  $v_c = i_c \cdot R_c$ . The current-to-voltage gain of the first stage is given by the collector resistance,  $G_1 = R_c = 3.9k\Omega$ . The input impedance of the first stage can be calculated using the hybrid-pi model for the BJT, obtaining  $R_{in} = \frac{V_T}{I_e}$ , where  $V_T$  is the

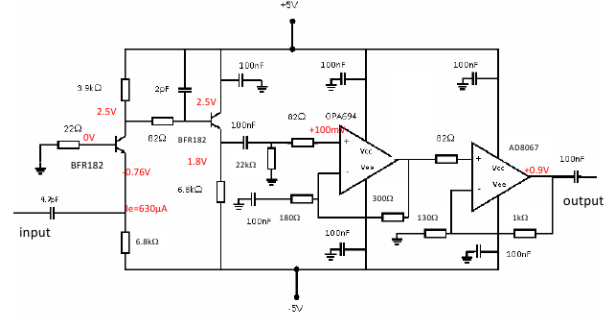


Figure 40: Schematic of the amplifier: the DC characteristics are reported in red.

thermal voltage: for  $T=300$  ° K,  $R_{in} = 41\Omega$ . The second transistor is just a voltage follower to decouple between the first stage and the second one. The second stage is composed by a OPA694 operational amplifier in a non-inverting configuration: its gain is given by  $G_2 = 1 + \frac{R_f}{R} = 2.7$ . This stage is coupled to the first one through a 100 nF capacitor to remove the DC component of the signal coming from the second transistor. In the third stage an AD8067 operation amplifier is used for its high bandwidth (54 MHz for a gain of 10) and because it is a rail-to-rail amplifier, letting the maximum output signal to be 5 V; the gain in bandwidth of this stage is  $G_3 = 8.7$ . The bandwidth of the amplifier is limited by the collector resistance  $R_c$  of the first stage and by the collector capacitance  $C_c$ . The cut-off frequency is given by  $f_{cut} = \frac{1}{2 \cdot \pi \cdot R_c \cdot C_c}$ . With  $C_c = 2pF$ ,  $f_{cut} = 20.5MHz$ .

**Performances** The overall current-to-voltage gain of the transimpedance amplifier is given by the product of the gains of the three different stages:  $G = G_1 \cdot G_2 \cdot G_3 = 91k\Omega$ . The charge gain (i.e. the ratio between the charge delivered by the input current pulse and the charge measured by a charge integrating device fed with the amplifier output signal) is given by  $G_c = \frac{G}{Z_{in}}$ , where  $Z_{in}$  is the input impedance of the charge-integrating device. For  $Z_{in} = 50\Omega$ ,  $G_c \simeq 1800$ . Figure 42 shows the measured charge gain for a prototype of

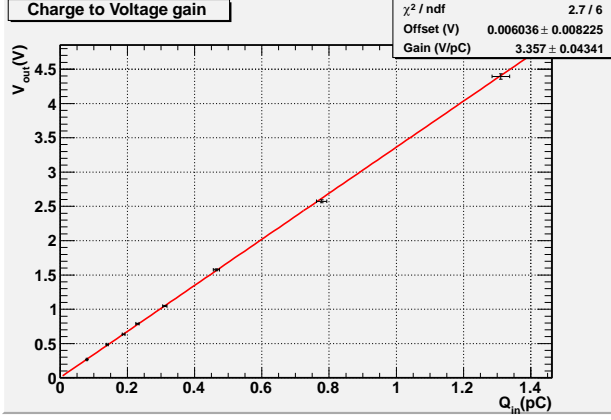


Figure 41: Measured charge-to-voltage gain of the Orsay amplifier.

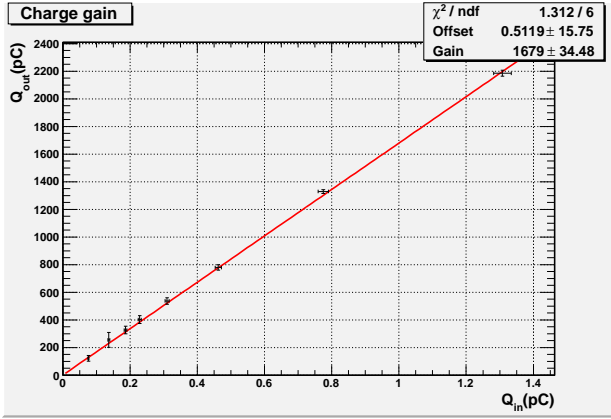


Figure 42: Measured charge-to-charge gain of the Orsay amplifier.

the FT-Orsay amplifier. It is not possible to define the charge-to-voltage gain of this amplifier without considering the time structure of the input current pulse since the amplifier does not perform a charge integration of the input signal. Fig. 41 shows the measured gain when a signal generator is coupled via a 4.7 pC injector capacitance. The signal rise time is 20 ns, similar to the rise time of the signal produced by the APD coupled to the PbWO<sub>4</sub> crystal. The measured value is  $G_v = 3.36 \pm 0.04 V/pC$ . The setup to measure the two gains ( $G_v$ ,  $G_c$ ) is reported in Fig. 43. C is a known capacitor (4.7pF  $\pm 2\%$ ) used to inject the input charge into the amplifier. The outputs signal is analyzed by a digi-

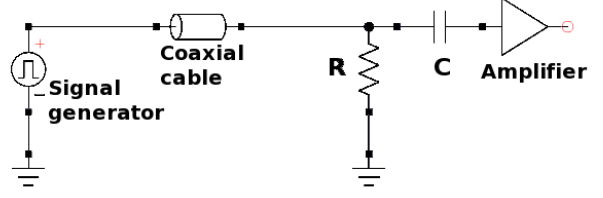


Figure 43: Setup used to measure the charge-to-voltage gain of the Orsay amplifier.  $R=50\Omega$  is used to terminate the coaxial cable.

tal oscilloscope (model LeCroy “WaveRunner 6100A”, 5 GS/s, 1 GHz bandwidth) and integrated is a 100ns gate.

The amplifier intrinsic noise has been measured with the same experimental setup described above, for different working temperatures ( $-20^\circ$ ,  $-10^\circ$ ,  $0^\circ$ ,  $10^\circ$ ,  $20^\circ$ ) using different capacitors placed in parallel to the input to simulate the detector capacitance. The RMS of the output signal has been measured and the ENC<sup>†</sup> has been calculated according to:

$$ENC = \frac{RMS}{G_c \cdot q_e} e^- \text{ (rms)} \quad (10)$$

Figure 44 shows the results obtained with four different input capacitances at different temperatures. The relationship between the output noise and the input capacitance is not linear, but exhibits a sort of “saturation” for high values of  $C_d$ . The temperature dependence is weak.

For an operating temperature of  $+20^\circ$  the measured noise of the preamplifier, with a detector capacitance of  $C_d=280$  pF, the same of the LAAPD we are planning to use, is:

$$ENC = (9000 \pm 100) e^- \text{ (rms)}$$

Fig. 45 shows the amplifier power consumption as a function of operating temperature,

<sup>†</sup>The ENC, “equivalent noise charge” is defined as the charge transported by that input signal giving, at the output of the amplifier, a signal whose amplitude is equal to the RMS of the output noise.

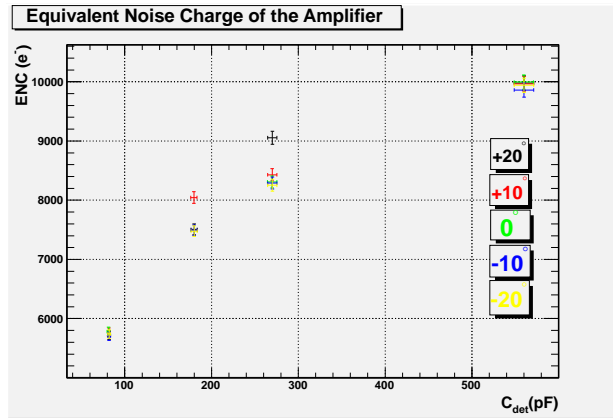


Figure 44: Equivalent Noise Charge of the Orsay amplifier measured as a function of input capacitance and working temperature.

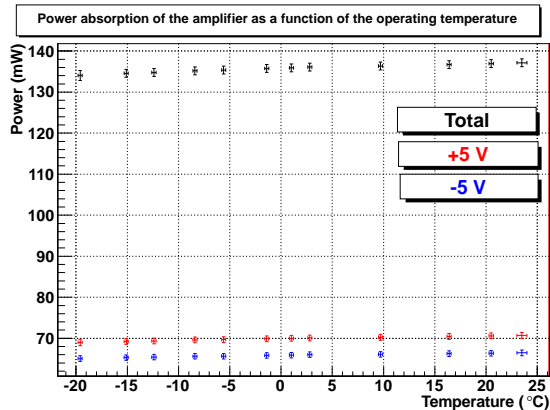


Figure 45: Measured power consumption of the Orsay amplifier as a function of the operating temperature.

including the total power and the single contributions from the +5 V and -5 V supply lines<sup>‡</sup>. For  $T=+18^{\circ}\text{C}$  the power consumption is  $\simeq 140\text{mW}$ , with equal weights from the +5 V and -5 V supply lines. This value slightly decreases while decreasing temperature, down to 135 mW at  $-20^{\circ}\text{C}$ . Measurements did not show any dependence of the power consumption on the event rate, up to 500 kHz.

<sup>‡</sup>Measurements have been done with an input signal to the amplifier equivalent to  $\simeq 100$  MeV deposited in the  $\text{PbWO}_4$  crystal.

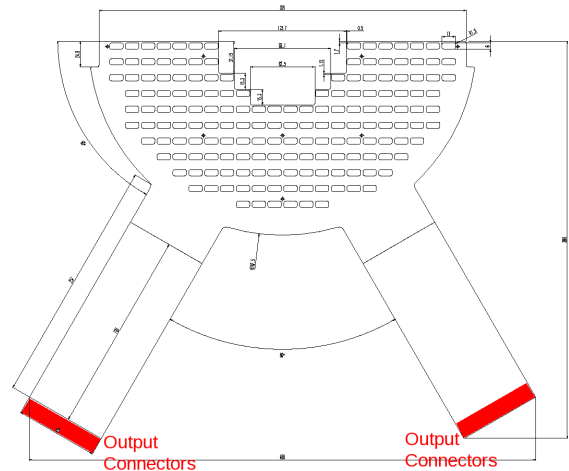


Figure 46: Layout of one of the two half of the FT-Cal motherboard.

**Future upgrades** Some modifications of the current design of the FT-Orsay amplifier have been tested to check the design against future requirements of the experiment. In particular we checked the possibility of reducing the gain without affecting the overall preamp performance (noise, dynamic range energy and time resolution ...). The simplest way is to decrease the gain of the second stage. This is given by  $G_2 = 1 + \frac{R_f}{R}$ ,  $R_f$  being the feedback resistance and  $R$  the inverting resistance.  $R$  can be increased to decrease  $G_2$ , down to  $G_2 = 1$ , i.e. non-inverting voltage follower. This modification has been tested and shown to not affect the performances of the amplifier.

### 2.3.2 FT-Cal motherboard

A custom PCB motherboard has been designed by INFN-Genova Electronic Group to distribute LV and HV to each preamplifier and collect output signals. FT-Cal channels are divided in two symmetric groups, each coupled to a identical PCB. The motherboard has two rigid *ears* hosting signal and voltage connectors outside the thermal insulation. Figures 46 and 47 show the motherboard layout and full assembly in the back

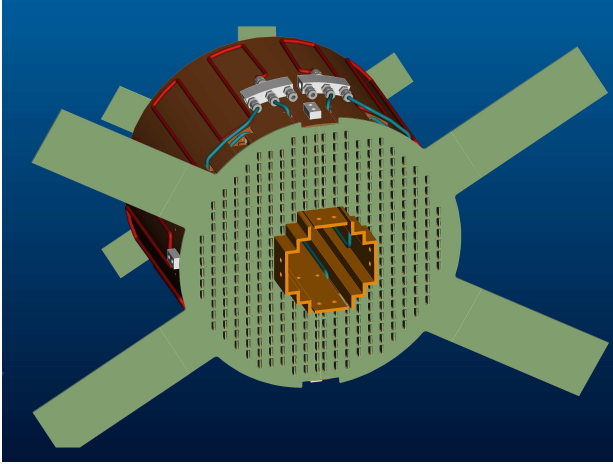


Figure 47: The FT-Cal motherboard mounted in the FT-Cal.

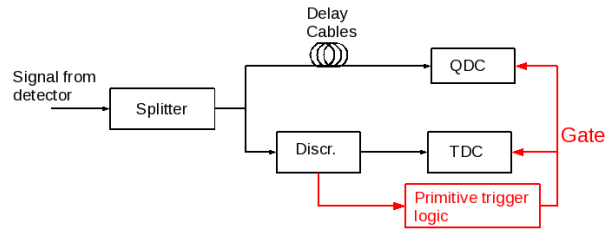
side of the FT-Cal.

### 2.3.3 Readout electronics

After the amplification, the signal has to be acquired via a proper DAQ system and processed to extract the relevant physical information: the *energy* deposited in the  $\text{PbWO}_4$  crystal and the *time* of the interaction. The CLAS12 DAQ system is not based on QDCs and TDCs, as for the CLAS detector [19], but it makes use of fADCs: the signal is continuously digitized by a fast flash analog to digital converter, and, if a trigger condition is satisfied, samples are stored for further analysis. TDCs (multi-hit) are still present in the system. The main advantages of this solution, compared to the “standard” one, are the following:

- Instead of only having the information of the *charge*, fADCs record the whole wave form, as a sequence of samples. This offers the opportunity to perform a more sophisticated off-line analysis, e.g. by applying some digital algorithms to filter signals from noise before calculating the charge.
- The digitization is continuous and the acquired samples are stored in a circular

**OLD DAQ system**



**NEW DAQ system**

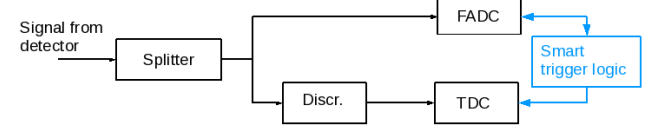


Figure 48: Top: the existing CLAS DAQ system, based on QDCs and TDCs. Bottom: the DAQ system for CLAS12, including fADCs and a smart trigger logic.

buffer inside the fADC. When a trigger is sent to the board the current buffer is frozen and ready for readout, while the acquisition continues, writing to another circular buffer reducing the dead-time of the system.

- There is no need to use delay cables, since the latency between the waveform digitization and the trigger arrival is programmable up to  $8 \mu\text{s}$  (existing CLAS detector has more than 50 km delay cables just for TOF!).

Finally, the use of fADCs gives the opportunity to develop a “smart” trigger logic: simple information about signal shape, time and charge are available *on-line*, and more sophisticated selection algorithms can be used to form the trigger. For more details about DAQ and trigger, see Sec. 7.

**fADC** Jefferson Lab developed a custom fADC that will be used by all 12 GeV upgraded experiments. This board, based on the VME64x standard, has a sampling rate of 250 MSamples/s, with an input range of 2 V. The characteristics of the board are re-



Figure 49: The JLab fADC.

ported in tab.8. JLab-fADC is equipped with a Switched Serial Extension (VXS), in addition to the standard VME backplane: it can transfer trigger information through a high-speed serial data line ( $\simeq 4$  Gb/s) to a dedicated board, mounted into a special slot into the crate. This feature will be widely used in the CLAS12 smart trigger (see Sec. 7.3 for more details).

**TDC** To precisely measure the interaction time, the FT-Cal will make use of commercial TDCs developed by CAEN SpA, model VX1190A, the same used by the other CLAS12 subsystems. Technical specifications are reported in Tab. 9. It is worth mentioning that the time can also be derived by the digitized wave form stored by the fADC. The time resolution achievable with this method is, in general, worse than using a dedicated TDC but, in our case, being the overall FT-

Parameter	Value
Input signals	16
Input range	User selectable (0.5 V, 1 V, 2 V)
Sampling clock	250 MHz
Resolution	12 bits (8 bits available by chip replacement)
Offset regulation	$\pm 10\%$ FS, channel by channel
Trigger latency	up to $8\mu\text{s}$
Data memory	$8\mu\text{s}$

Table 8: JLab fADC specs.

Cal timing dominated by the light statistics, a time resolution of few hundreds ps can be obtained. We are still considering the two options: using only fADC or fADC + discriminators and TDCs.

**Splitter** A Y configuration, passive resistive splitter will be used to split the signal from the amplifier, for the fADC and the Discriminator + TDC chain. The internal resistive network is designed to have equal signals at the two outputs. The possibility to perform a non-equal division of the input has been considered and will be applied, if necessary, to further adjust the overall dynamic range of the system to the fADC maximum input voltage of 2 V. This device has been proved to not introduce any further noise contribution.

**Possible modifications** At the time this document is being written, the JLab fADC firmware is being upgraded to embed inside TDC and scaler functionality. This feature is still under test, but first results show that the obtained resolution is compatible with that of a standard board. If this feature will be fully available at the time of the FT-Cal construction, we plan to simplify our read-out chain eliminating TDCs. Splitters will be kept as a patch panel to connect the 3M cables from the FT-Cal motherboard to the LEMO connectors inputs on fADC boards, and to reduce the signal amplitude if needed (changing their division factor).

Parameter	Value
Input signals	128
Dynamic range	52 $\mu$ s
Resolution	19 bits
LSB	100 ps
Trigger window width	User programmable, from 25 ns to 100 $\mu$ s.

Table 9: CAEN VX1190A TDC characteristics.

## 2.4 Slow controls

Slow controls for CLAS12 will be based on EPICS [34]. For standard equipment, e.g. HV, LV we will use modules which are recommended and supported by JLab and have standard EPICS drivers.

### 2.4.1 APD bias system

To operate, each APD needs to be reverse-biased with an high-voltage positive power source,(see also Par. 2.2.1). The APD intrinsic gain depends on the bias voltage with  $\frac{1}{G} \frac{\partial G}{\partial V} \simeq 4\%$  and therefore the power supply needs to be stable in time, with low output noise. The CAEN board A1520P is an excellent choice: it has been expressly designed for the APDs of the CMS electromagnetic calorimeter fulfilling all our requirements in terms of dynamic range, linearity and noise. Each board is equipped with 12 independent channels: after measuring each APD intrinsic gain as a function of the bias, we are planning to arrange them in group of tens, with relative gain variations not greater than 5%. In this way, only three boards will be necessary to power the whole detector.

### 2.4.2 Low voltages

The amplifiers used in the FT-Cal need to be operated with +5 V and -5 V, as shown in Par. 2.3.1. The power consumption from each of the two voltage sources is approximately 70 mW, almost independent on the event rate, giving a power consumption of  $\simeq 140$  mW per board, for a total of 56 W for a 400-channels calorimeter. For lab testing and operations with FT-Cal prototypes, see

Parameter	Value
Output Voltage	0-500 V
Output Voltage resolution	1 mV
Output Noise	< 20 mV pp
Vset vs Vout accuracy	$\pm 40$ ppm
Thermal stability	$\pm 3$ ppm $^{\circ}$ C

Table 10: CAEN A1520P characteristics.

Sec.2.8.1 and 2.8.2, we used a Delta Elektronika SM 18-50 dual power supply. This would also be a suitable choice for the whole calorimeter, being the maximum power (900x2 W) greater than the requirement, and the output RMS noise sufficiently small ( $\simeq 2$  mV) to not affect the amplifier behavior.

The full FT-Cal will be powered by a Wiener *MPOD universal low voltage power supply*. This choice has been done to be fully compatible with the CLAS12 slow control system, that has chosen the Wiener system as the standard low voltage power supply for the whole experiment. The low-voltage requirements of the detector in terms of total power ( $\sim 30$  W at +5 V and -5 V) and RMS noise (lower than  $\simeq 5$  mV) can be easily be achieved using the MPV8008L board. This model is equipped with 8 independent channels, each delivering up to 40W at 8 V. Sensing is provided to compensate the voltage drop across the connecting cables.

### 2.4.3 Chiller and T control

Temperature stability will be provided by a Lauda XT150 chiller unit. This is a self regulating unit and will not require EPICS control, however, we will monitor the output temperature of the unit using the EPICS *streamDevice* module. The FT-Cal temperature will be also be monitored by a set of PT100 thermoresistors. For the prototypes operations we used an Agilent 34972A Data Logger. The FT-Cal will use Omega modules which have been standard for CLAS and have EPICS support.



Figure 50: Single crystal assembly: from the front to the back, the PEEK holding nose, the wrapped crystal, the LAAPD in the PEEK housing, the FT-Orsay preamplifiers grounded with a Cu plate.

#### 2.4.4 LED monitor system.

The light monitoring system will use a multiplexed LED flasher described in Sec.2.6. The current version is programmed via a USB interface. For the final design an ethernet interface will be used and EPICS support developed based on the EPICS *streamDevice* module.

### 2.5 Mechanical design

The mechanical design of the calorimeter is mainly driven by three considerations:

- minimization of the empty spaces between crystals;
- cooling to 0° C;
- optimal coverage of the requested acceptance without interference with the rest of CLAS12.

#### 2.5.1 Single crystal assembly

The building block of the calorimeter is the single lead tungstate crystal. Each crystal will be  $15 \times 15 \times 200 \text{ mm}^3$ , for a weight of  $\sim 370 \text{ g}$ . Each crystal must be optically coupled to a large area APD and to a pulsed light source for calibration. To achieve the maximum light collection efficiency, the APD covers almost the whole area of the downstream

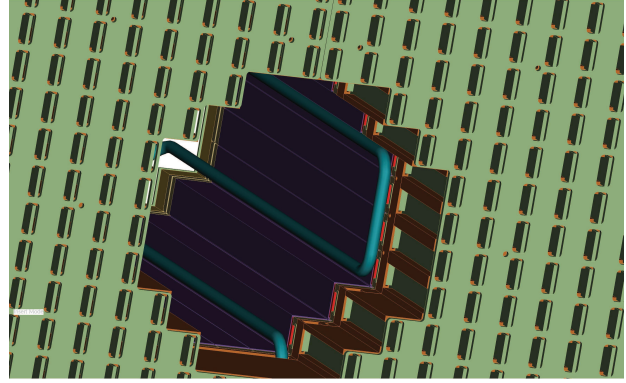


Figure 51: Insertion of the crystals in the copper thermal/grounding shield.

end of the crystal, so the LED for monitoring will be hosted on the upstream end. This reflects onto the mechanical design of the single crystal assembly, since we foresee to have a monolithic self-supporting element made of the crystal itself, the APD, the reflective coating of the crystal and some support structure. To avoid dead volume in the detector, the mechanical support for each crystal will be provided by the reflective material. We chose 3M Vikuiti reflective film. This material is non conductive, has a reflectivity higher than aluminated Mylar one and, if properly hot-formed, can hold the weight of a crystal. Each crystal will be prepared as follows. First of all, a rectangle of 3M Vikuiti film will be hot-formed to fit the crystal shape. In the meantime, the APD will be glued with proper optical glue to one end of the crystal. Then the crystal with its APD and two properly shaped PEEK blocks will be placed in the Vikuiti film and only the PEEK blocks will be glued to the reflective film. The resulting assembly has pins on both ends to be fixed to proper plates and the weight is transferred via the PEEK blocks. Figure 50 shows the single crystal assembly from the frontal PEEK support to the FT-Orsay preamplifier. In Fig. 51 is shown how each crystal will be connected to the copper/grounding thermal shield.

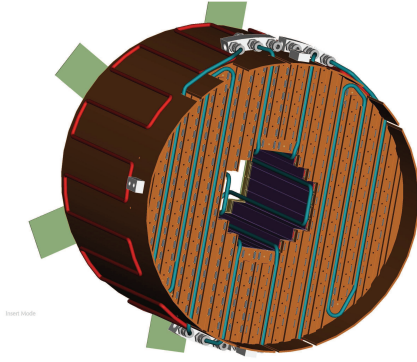


Figure 52: The copper thermal/grounding shield with the cooling pipes.

### 2.5.2 Module design

The crystal assemblies will be installed in an array to allow complete shower containment for electrons in the FT angular acceptance. Two copper plates, placed upstream and downstream the calorimeter, will provide load path and positioning for the crystal assemblies. On the APDs side there will be amplifiers for each APD and a mainboard which will provide power supply and signal collection for each channel. The amplifiers will be installed to allow the replacement of each one of them without dismounting anything else. The copper thermal/grounding shield with the cooling pipes is shown in Fig. 52. A shaped copper vessel will enclose the crystal assemblies to provide proper grounding and the required thermal stability and uniformity. A section view of the complete calorimeter is shown in Fig. 53.

### 2.5.3 Cooling

The FT calorimeter has been designed to operate between  $0^{\circ}\text{C}$  to room temperature. This temperature will be achieved via circulation of coolant in a circuit welded on the rear copper plate and on the inner and outer copper vessels. The cooling system has been designed to compensate the heat inlet coming

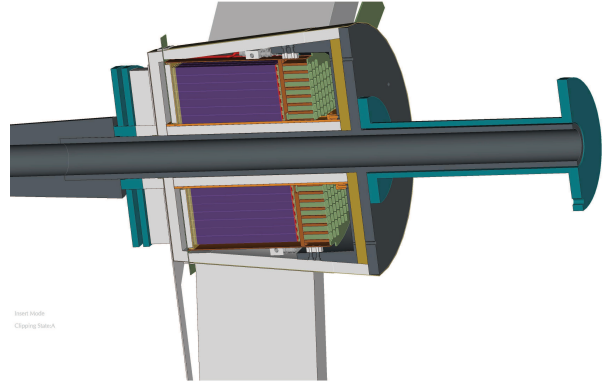


Figure 53: Cross section of the FT calorimeter: in black, the crystals, upstream the PEEK forward blocks and the forward copper plate, downstream the rear copper plate, the preamplifiers (in green) and the mainboard (in white), in light blue and yellow, part of the insulation.

from the outside world, taking into account 20 mm of insulating foam (Polyisocyanurate, declared thermal conductivity  $0.024\text{ W/m}\cdot\text{K}$ ) and from the amplifiers, which are expected to dissipate  $\sim 150\text{ W}$ .

The insulation is less effective between the calorimeter and the inner tungsten pipe. There the maximum allowable thickness for the insulation is smaller than 20 mm, there is no convection with air but the conduction in the tungsten pipe and there are the PEEK rods that provide the path load for the calorimeter. In that region, the effective conductance is  $0.056\text{ W/m}\cdot\text{K}$  over 20 mm.

We have performed Finite Elements calculation to evaluate the needed cooling power and the temperature distribution on the detector, and the result is that we can manage to achieve the design temperature and uniformity, but the inner tungsten pipe and the tungsten cone are expected to stabilize at a temperature just above than the dew point. A typical temperature map is shown in Fig. 54.

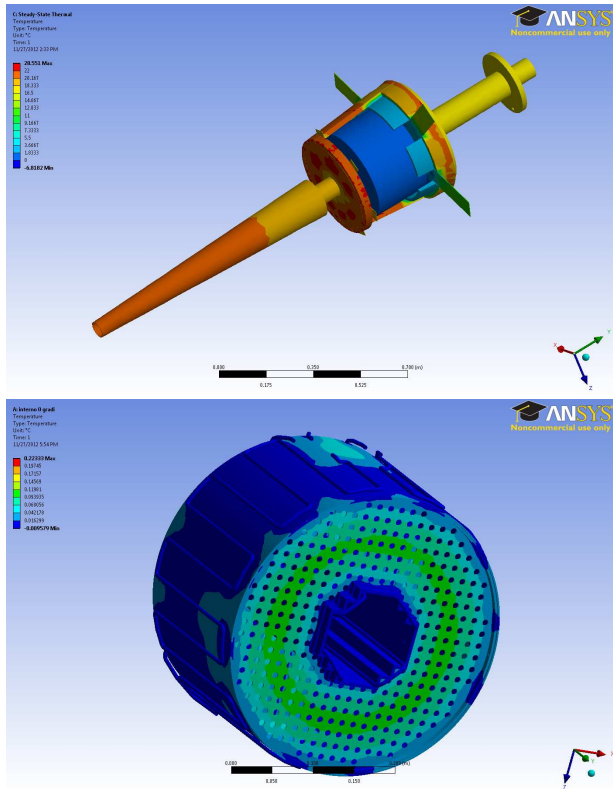


Figure 54: Temperature distribution on the FT calorimeter obtained taking into account the heat dissipated by electronics, air convection and heaters upstream and downstream the insulation. Note that the scale is not homogeneous, to appreciate small variations at lowest and highest temperatures.

## 2.6 Light Monitoring System

Lead tungstate scintillating crystals are known as an appropriate material for use in total absorption shower detectors. Unfortunately, although relatively radiation tolerant, they do lower their light output when exposed to radiation and recover when the radiation source is removed. Extensive studies performed at the Institute for High Energy Physics (IHEP) in Protvino, Russia, confirmed that the PbWO light output changes with the irradiation dose rate. Dedicated measurements showed that degradation of light output in PbWO crystals under pion irradiation with dose rates up to 20 rad/h occurs due to light transmission

loss only, rather than changes in the scintillation mechanism [35]. Further complications arise because at the same irradiation intensity, changes in light output may vary from one crystal to another [36] [37]. In order to maintain the intrinsic energy resolution, crystals have to be continuously monitored and if necessary, recalibrated. Since crystals are coupled to a light sensor, an APD in our case, the monitoring system should be able to test the response of the whole chain: crystal, APD, readout electronics rather than to only measure the change in light transmission. In particular it will be used for monitoring the channel matching and the crystal transparency, the optical contact between crystals and sensors, preamplifier gain and stability, the linearity of the entire electronic section and the timing. Since the PbWO4 light yield and the APD gain depend on the temperature a stable formalization, with  $\Delta T = 0.1^\circ C$ , is required.

There are different options available, based on different methods:

- Monitoring with a radioactive source, for instance a small YAP scintillator with an alpha emitter deposited on top is coupled to each channel. Despite an excellent stability of the emitted light this method presents some disadvantages: the fixed light output doesn't allow to vary the intensity to check the system linearity; the measurement of the relative timing is not possible because the sources are independent and are not to triggerable by an external signal.
- Monitoring with a laser. In this case the light intensity can be varied in a chosen range and the light pulse generation can be controlled via an external trigger source. However lasers are in general very complex and are very sensitive to variations of environmental conditions such as temperature. This method has some other disadvantages related to the complex optical-fibers system to distribute

the light to the crystals.

- Monitoring with a LED. In spite of the need of a thermal control, LEDs offer considerable advantages: matching with crystals is more simple than for lasers, since each crystal can have a LED in front of it and the arrangement of electric wires is less critical than optical fibers. The main disadvantage is related to the complexity of the electric circuitry: to cover a large light range keeping a good timing, each LED needs a separate driver leading, for calorimeter of significant size, to a large number of electronic circuits.

Many electromagnetic calorimeters based on PbWO technology used a monitoring system: CMS-EC (CERN LHC) adopted a laser monitoring system; the signal was distributed to the crystals through optical fibers. PANDA-EMC (FAIR), developed a LED monitoring system consisting in few LED blocks that illuminate 1000-1200 crystal at time; the light distribution is achieved via an optical-fiber system. ALICE-PHOS calorimeter (CERN LHC) used a LED monitoring system with each crystal coupled to a single LED/driver. For the FT-Cal, we are developing a monitoring system based on LEDs. LEDs have a number of advantages, in particular it is possible to obtain a shape and a duration of the monitoring-light flash that would be similar to the features of the crystal scintillation. In fact: the emission spectrum of the monitoring light can be chosen similar to the radio-luminescence spectrum of PbWO, the effective optical path length for monitoring light in the crystal can be matched to the average path length of the scintillation light produced by an electromagnetic shower, and pulse length can be tuned to reproduce the PbWO scintillation decay time. These crystals have a rather complex emission spectrum, consisting in two main components: one blue, peaking at 420nm and one green, peaking at 480-520 nm. Fig. 55 shows the emission spectrum of PbWO4 crystal (blue), compared

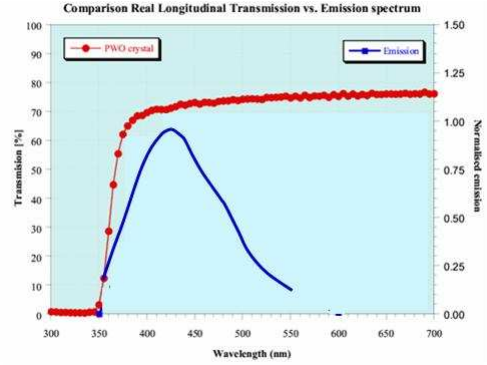


Figure 55: Emission spectrum of PbWO4 (blue plot)

with the longitudinal transmission (red). To optimize the monitoring of the crystal light output change, we are using a blue light LED, with wavelength close to the 430 nm emission peak of the PbWO4 crystal and where the radiation damage may have the maximum effect.

Considering the design performance of the FT-Cal, the monitoring system requirements are listed below:

- The calibration factor of each channel should be determined with a relative accuracy better than  $5 * 10^{-3}$  to achieve the required energy resolution.
- The LED housing should be located on the upstream face of each crystal, at the opposite end respect to the light sensors and electronics.
- The LED intensity should adjustable in a range from 500 to 100.000 photons.
- The Pulse rise time should be in the range from 500 ps to 2 ns.
- The Time jitter (channel by channel) should be  $\leq 200$  ps.
- The Pulse frequency should be in a range from 10 to 100 Hz.
- The LED wavelength should be close to 450 nm.

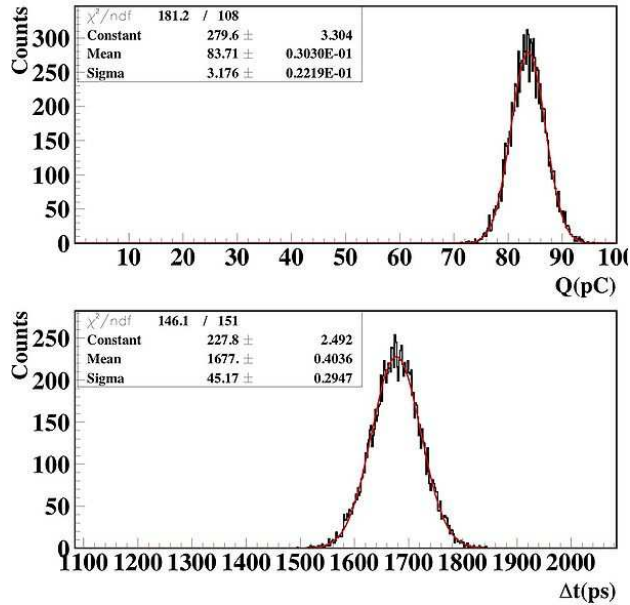


Figure 56: Charge distribution (up) and time distance between trigger and PMT signal distribution (down)

- The work temperature should be from +15 to -25 Celsius.
- The LED light emission spread (channel by channel) should be within 10%.

We assume that each LED, placed in the closed environment of the crystal, will be kept at constant temperature with an accuracy of  $\Delta T = 0.1^\circ C$ . The monitoring system has to show a long-term stability, comparing results from several monitoring runs, and short-term stability, during a single monitoring run. The stability can be characterized by measuring the variations of the monitoring-signal ratio  $R$  of two different channels. In both cases a relative spread of few part per mill is required ( $\sigma_R/\langle R \rangle < 5 * 10^{-3}$ ). We initially looked for some commercial solution finding a LED system developed by CAEN company as part of their SiPM evaluation kit. The system is based on a fast electronic circuit driving a blue LED ( $\lambda=470$  nm). Light is guided to the light sensor via an optical fiber. The LED light intensity can be manually varied,

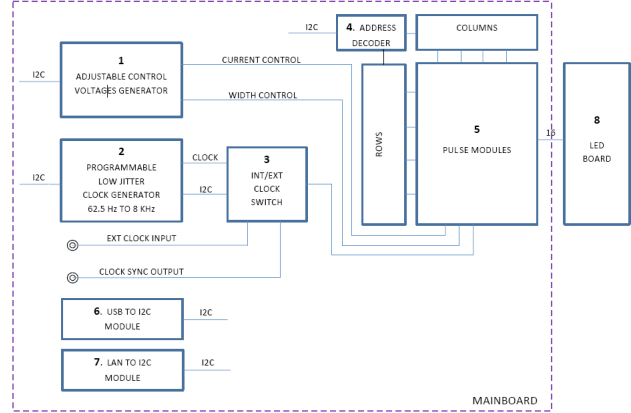


Figure 57: Block diagram of the FT-Cal LED calibrator.

while the trigger can be given either via an internal or an external source. We performed a set of measurements by using a PMT (Hamamatsu R2083) as light sensor, to characterize the charge released and the time property of the driver. Figure 56 shows the charge distribution (up) with a spread of 3.5% and the timing resolution (down) that is about 45 ps. The CAEN driver has excellent time properties with a very small jitter largely exceeding out requirements but the requirements on the dynamical range, the light distribution and the FT-Cal geometry called for a non-commercial solution. For this reason, in collaboration with the Electronic Service of the INFN-GE, we developed a custom circuitry.

### 2.6.1 INFN-LEDMON prototype

The LED monitoring system is splitted in two boards: one containing the control logic and the LED driver circuits, and the other, to be mounted in front of the FT-Cal crystals, hosting the LEDs. The two boards are connected via a board-to-board connector allowing the required flexibility to match the FT-Cal geometry and positioning. The schematic is reported in Fig. 57. The meaning of the different blocks is reported below:

- 1. Adjustable control voltages genera-

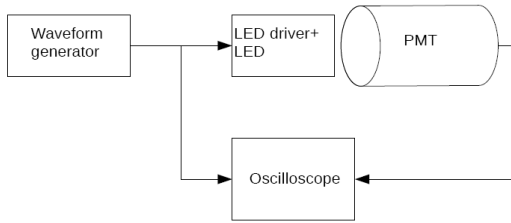


Figure 58: The experimental set-up used to measure the performance of the NFN-LEDMON prototype.

tor. This circuit is composed by a double 12bit DAC and some OpAmps It generates two voltages to independently control the LED pulse width and the the LED current. The two voltages are adjustable via the I2C bus in the ranges 5 to 15 ns and 5 to 25 mA respectively.

- 2. Programmable clock generator. This circuit is composed by a quartz oscillator and a synchronous programmable frequency divider. It generates a square wave used by the pulse module as a trigger. The frequency is programmable via the I2C bus from 62.5 Hz to 8 KHz.
- 3. Internal/external clock switch. Via the I2C bus, this switch/buffer sets the internal or external clock to be sent to the pulse module. An output sync signal is available. The circuit I2C bus.
- 4. I2C address decoder. It is used to address any single LED by means of a rows/columns grid.
- 5. Pulse module. This module is composed by N pulse circuits (N=16 for the Proto-16 and N=332 for the FT-Cal detector). Each circuit is capable to power its LED by means of two VHF transistors controlled by a fast differential voltage comparator that sets the pulse width. A third transistor, controlled by an OpAmp controls the LED current.

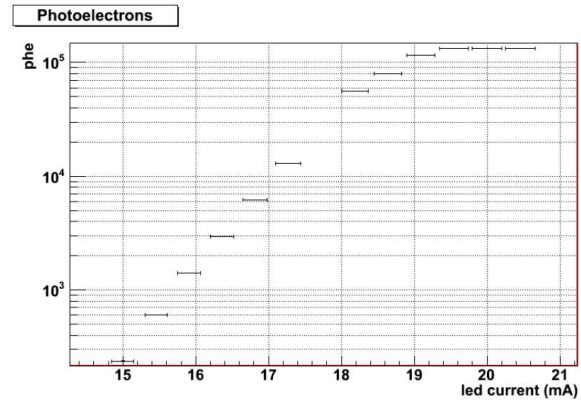


Figure 59: Number of photoelectrons as a function of the driver current. The corresponding energy per crystals range form 10 MeV to 10 GeV.

- 6. USB to I2C Module. This is an external, commercial board connected to the mainboard logic via a 5V/3.3V voltage translator.
- 7. LAN to I2C module. This is another external, commercial board based on the PIC32 micro-controller connected to the mainboard with a high density board-to-board connector.
- 8. LED board. This board is populated only by LED (blue) and diodes. Some special care is taken to couple LED to crystal to avoid crosstalk between different channels.

Each LED is individually lighted by a programmable length and intensity pulse. It is also possible to simultaneously switch on a set of LED with a programmable pattern. The system is triggered by an internal clock or by an external signal. In both cases the trigger signal is available for a precise time reference. The performance of the LED driver has been measured coupling a single monitoring channel to a photomultiplier. The experimental set up is shown in Fig. 58. The driving pulse is very narrow (5ns) keeping a small width when convoluted with the LED emission (<20ns), being the PMT (Photonis

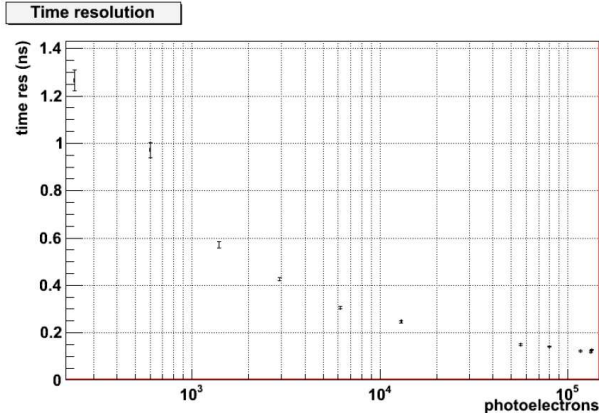


Figure 60: Time resolution measured as the difference of trigger signal and the PMT pulse.

XP2262B) time response negligible. Results concerning the dynamic range and the time resolution are reported in Figs. 59 and 60. Figure 59 shows the measured photoelectrons as a function of the led current. Rescaling results to take into account the APD read-out and the crystal LY/MeV the equivalent energy ranges from 10 MeV (500 phe) to 10 GeV (500k phe) perfectly matched to the expected energy collected by each crystal. Figure 60 shows the measured time resolution as a function of the number of photoelectrons defined as the sigma of the time difference distribution between the trigger signal and the PMT output. The PMT time resolution has not been subtracted by the data. A time resolution of  $\sim 100$  ps is reached at high light intensity. The two plots show that a gain matching between different crystals exploring the whole dynamical range and a time jitter measurements are possible running the LED monitoring systems in the two different setups. As an example of the stability in time of the system, Fig. 61 and 62 show channels 5 and 13 of the Proto-16 at the beginning and at the end of 100h ( $\sim 4$  days) run at  $T=+18^{\circ}\text{C}$ . The stability of each individual channel is in the range of 2%. When the ratio of the two channels is considered, Fig. 63, the stability is at level of few ‰. The plots

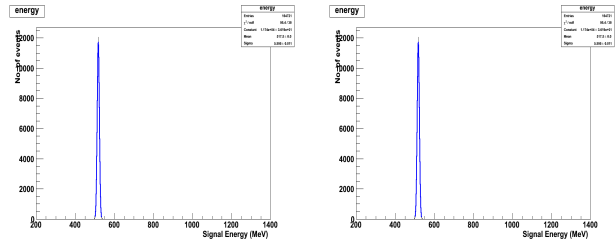


Figure 61: Stability of Proto-16, channel 5, measured at the beginning and at the end of 100h run at  $T=+18^{\circ}\text{C}$

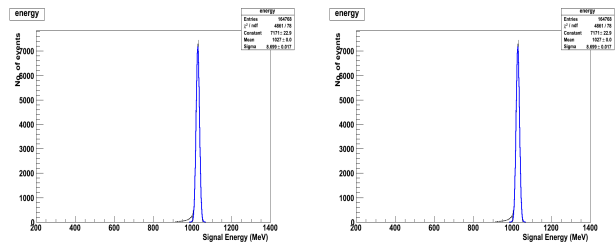


Figure 62: Stability of Proto-16, channel 13, measured at the beginning and at the end of 100h run at  $T=+18^{\circ}\text{C}$

refer to data samples taken in few minutes, running the LED driver at 1 KHz to avoid any temperature drift and minimize other instabilities.

The LED monitoring system can be remotely controlled via ethernet and USB ports. The USB is used for debugging and easy programming while via ethernet an EPIC server can be downloaded and run on the micro-controller.

## 2.6.2 INFN-LEDMON final design

The final LED monitoring system to be installed in the FT-Cal will split the drivers and the LEDs on 6+6 cards. A further controller card, containing the common circuits, will be added. The following paragraphs give a short description of the various blocks and the main differences respect to the prototype. The lay-

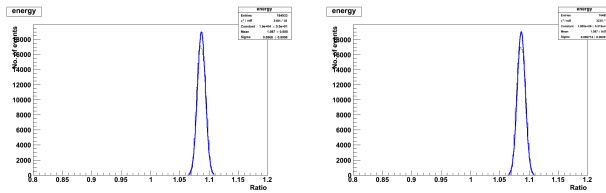


Figure 63: Stability of Proto-16, ratio of channel 5 and 13, measured at the beginning and at the end of 100h run at  $T=+18^{\circ}\text{C}$

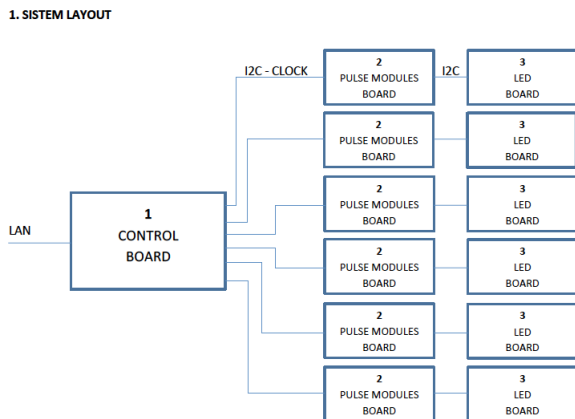


Figure 64: Layout of the INFN-LEDMON system.

out of the new design is shown in Fig. 64.

**Control board** The scheme of the new control board is shown in Fig. 65.

1. Same as the previous version
2. This block is the same as in the INFN-LEDMON prototype, is kept for debugging. The LAN only will be used to control the calibration system.
3. Same as the previous version. Probably a micro SD card will be added in order to store the necessary software.
4. Same as the previous version with some more buffers will be added since the clock signal is now sent to several pulse boards.
5. This is a new module required to control and power the expected number of chan-

nels.

**Pulse module** The scheme of the new pulse module board is shown in Fig. 66.

1. This module is simply a I2C to 64bit decoder. Every bit enables a LED.

2. In INFN-LEDMON prototype the voltage reference module was used only by the DAC. In this new version the reference voltage is also used by the pulse generator to have a more stable pulse duration.

3. This block is similar to the previous version except than now it generates only the current control voltage. The pulse duration is fixed to 5ns because from the tests we understood that this adjustment can be eliminated.

4. In the previous system a current control for each LED was provided and all the pulse modules were powered. In the final version a single current control is provided and only the enabled pulse module is powered in order to reduce power consumption and crosstalk between channels.

5. These modules produce the current peaks necessary to the LEDs. As already written only one module a time is powered and only the related LED will flash.

**LED board** This board is populated only by the LEDs and their counter diodes. The INFN-LEDMON prototype used a 2 layers board; in the final version, two further ground layers will be added to improve signal shielding.

We are in the process of testing a new prototype based on the new design. Results will be included to a newer version of this documents as available.

## 2.7 FT-Cal simulations

Detailed simulations of the FT-Cal have been done with the GEANT4-based Monte Carlo code for CLAS12, GEMC [39] to understand

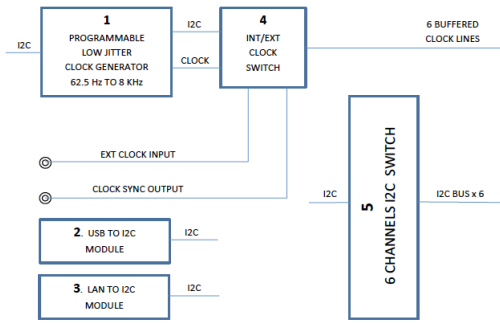


Figure 65: The control board of the INFN-LEDMON system.

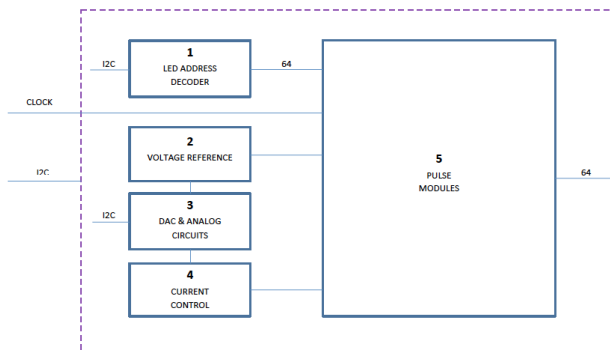


Figure 66: The pulse module of the INFN-LEDMON system.

the calorimeter performance and optimize its design.

### 2.7.1 Geometry

The geometry was implemented in GEMC, assuming the FT-Cal made of  $\text{PbWO}_4$  crystals. Fig. 67 show sections of the detector in the GEANT4 viewer. The calorimeter, consisting of 332 crystals, was placed at a distance of 188.6 cm from the CLAS12 nominal center. The crystals have a rectangular shape with a section of  $15 \times 15 \text{ mm}^2$  and a length of 200 mm, corresponding to about 23 radiation lengths. The crystals are arranged around the beamline to cover angles from  $2^\circ$  to  $5.5^\circ$  to contain the electromagnetic shower produced by electrons in the angular range

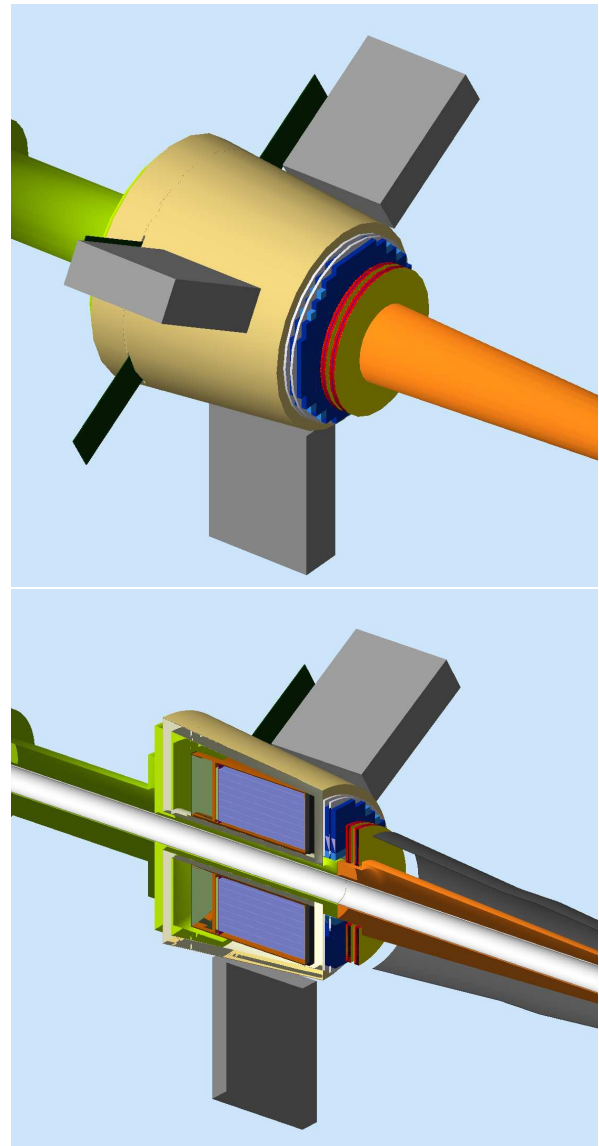


Figure 67: Full view (top) and section view (bottom) of the FT as implemented in the CLAS12 GEANT4 simulation code. The crystals (purple) are enclosed in the copper case (orange) that acts as thermal shield. This is supported by the tungsten beam pipe (green) and surrounded by thermal insulation material (white). The FT-Hodo (blue) and FT-Trck (red-gold) are placed in front of the FT-Cal. The extension of the FT-Cal motherboard (dark green) and the FTM front-end electronic crates (green), located along the direction of the torus coils are also shown. A tungsten cone (orange) is located in the upstream region to shield the detector from electromagnetic background.

from  $2.5^\circ$  to  $4.5^\circ$ . The crystals are placed inside a copper case that acts as a thermal shield. A tungsten cup, composed by a thick plate and a conical structure, is located on the rear part of the crystal assembly, outside the copper case to shield the forward part of CLAS12 from shower leakages. In addition to the crystals, the other components of the FT-Cal, such as the PEEK supports, APDs, PCB motherboard and thermal insulation, are realistically described in the geometry implementation. Simulations were run including the other components of the FT (see Sec. 8) and the Møller shield to have a realistic description of all the materials particles would cross and an accurate determination of backgrounds.

### 2.7.2 Digitization

The energy deposited in the FT-Cal crystals by incident particles is transformed into the corresponding electrical signal as follows. For each *step*  $i$  generated by GEANT while tracking particles in the active volume, the energy deposited,  $E_i$ , and the time of deposition,  $T_i$ , are evaluated and saved in arrays. The information related to steps occurring in the same crystal within a user-selected time window are grouped, defining a *hit*. For the FT-Cal, this time window was fixed to 4 ns, corresponding to the sampling time of the fADCs that will be used for the signal readout. For each hit, the values of  $E_i$  and  $T_i$  are analyzed to determine the overall energy and time information as well as the related digitized information corresponding to the output of the readout electronics (fADCs and TDCs). The main steps of the hit information processing are outlined in the following.

#### Energy:

- the values of deposited energy,  $E_i$ , in each hit are summed to determine the total deposited energy  $E_{tot}$ ;

- the total energy  $E_{tot}$  is multiplied by a fixed light yield to estimate the number of optical photons generated in the scintillator  $N_{OP}$ ;
- the number of optical photons reaching the crystal face,  $N_F$ , where the light sensor is located is then estimated as  $N_F = N_{OP} \times f_{LT}$  where the factor  $f_{LT}$  represents the light transmission efficiency in the crystal and was chosen in order to reproduce the values measured in the laboratory tests;
- the number of optical photons hitting the sensor surface is defined as  $N_S = N_F \times A_{sensor}/A_{crystal}$ , where  $A_{sensor}$  is the active area of the sensor and  $A_{crystal}$  is the crystal face area;
- the number of electron-hole pairs,  $N_{eh}$ , created in the sensor by the incident light is extracted randomly according to a Poisson distribution with mean equal to  $N_{eh} = N_S \times QE_{sensor}$ , where  $QE_{sensor}$  is the effective quantum efficiency of the sensor evaluated as the convolution of the quantum efficiency reported on the manufacturer data sheets with the light emission spectrum of the scintillator;
- the signal produced by the sensor is obtained multiplying the number of electron-hole pairs, previously determined, by the sensor gain  $G$ ; for APDs the gain is randomly selected with a Gaussian distribution with the mean corresponding to the set gain, e.g. 150, and the sigma accounting for the gain fluctuations induced by temperature or supply voltage variations within  $0.1^\circ$  and 10 mV; using the values of  $dG/dT$  and  $dG/dV$  measured experimentally and reported in Section 2.2.1, the total gain fluctuations are of the order of 0.33%;
- the effect of the preamplifier noise is included summing to the sensor signal a random number extracted according to

a Gaussian distribution with zero mean and sigma equal to the preamplifier input noise (ENC) of 9000 electrons; this noise level corresponds to energy fluctuations of the order of 1.6 MeV on a single crystal operated at room temperature.

- the resulting number of electrons is multiplied by the preamplifier gain (1800) to obtain the output signal; this is then converted in Coulomb and finally in ADC channels accounting for the resolution of the electronic boards.

#### Time:

- the time values of each step in one hit,  $T_i$ , are averaged to define the hit time,  $T$ ;
- the arrival time of the optical photons on the sensor,  $T_S$  is evaluated summing to the hit time  $T$  the propagation time  $L/v_{light}$ , where  $L$  is the distance between the hit position and the sensor and  $v_{light}$  is the velocity of light in the crystals;
- the finite time resolution of the system is accounted for summing to  $T_S$  a random number extracted according to a Gaussian distribution with zero mean and sigma set equal to 200 ps;
- the resulting time value is converted into TDC channels accounting to the time resolution of the boards of 25 ps.

Using this algorithms, the output information provided by GEMC for each simulated event contains for each hit the crystal ID, the energy deposited  $E_{tot}$ , the time of deposition  $T$ , the coordinates of the hit position, the identifier of the particle inducing the hit, the fADC channels and TDC channels.

### 2.7.3 Shower reconstruction algorithm

The output of the GEMC simulation were analyzed to determine the energy and time resolution. A cluster algorithm was developed to

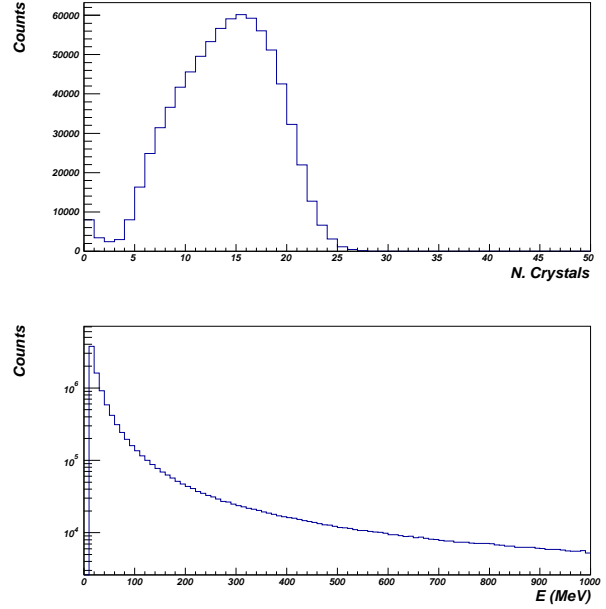


Figure 68: Top: number of crystals involved in a cluster induced by electrons with energy of 0.5-4.5 GeV, assuming a 10 MeV equivalent threshold on the single-crystal signal. Bottom: energy distribution of the single crystal signal for the same events.

identify the occurrence of an electromagnetic shower induced by an electron or a photon, group the crystals involved and determine the total energy and time of the shower.

The clustering algorithm identify first the hit with the highest energy deposition and associate to it other hits occurring in adjacent crystals within a chosen time window. The same process is repeated for each of the secondary crystals associated to the first, adding to the cluster all the hits with a transverse distance from the primary hit less than three times the Moliere radius, until a space or time gap is found.

After the first cluster is identified, the same algorithm is applied iteratively to the remaining hits, until they are all associated to a cluster. Assuming an equivalent threshold of 10 MeV on the signal detected in the single crystal, the number of crystals involved in a clus-

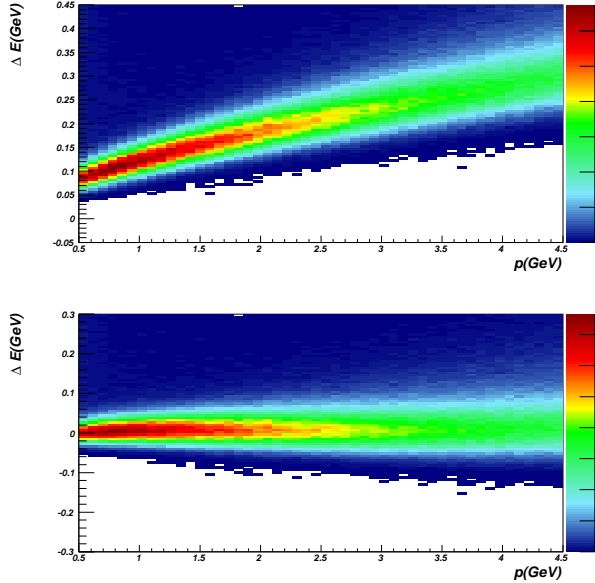


Figure 69: Top: difference between the simulated electron energy and the reconstructed cluster energy as a function of the electron energy for a 10 MeV equivalent threshold on the single crystal signal. Bottom: difference between the simulated electron energy and the cluster energy after the leakage correction.

ter is of the order of 5-25 as shown in the top panel of Fig. 68. The bottom panel of the same figure shows the energy reconstructed from a single crystal, ranging from the chosen threshold to about 60% of the incoming electron energy.

For each identified cluster, the hit information is processed determining the cluster energy as the sum of the energy of each hit and the cluster time and position as the energy weighted average of the related information in each hit.

#### 2.7.4 Leakage corrections

The reconstructed cluster energy can result to be systematically smaller than the actual energy of the particle that induced the shower. This is due to leakages in the shower containment caused by the limited dimension of

the calorimeter, by cuts in the clustering algorithms and thresholds in the hit detection. An example of the difference between the reconstructed cluster energy and the simulated electron energy is shown in the top panel of Fig. 69. This was obtained assuming an equivalent threshold on the APD signals of 10 MeV: the leakage varies from  $\sim 80$  MeV (16%) for 500 MeV electrons to  $\sim 300$  MeV (6.6%) for 4.5 GeV electrons.

Once the geometry of the detector, the digitization and reconstruction algorithms are fixed, this effect can be easily corrected for, by parametrizing the leakage as function of the reconstructed cluster energy and position in terms of an analytic function and applying the correction. In this specific case, the dependence of the difference between the reconstructed cluster and simulated electron energies was fit to a 4th-order polynomial function which was then used as an additive correction to the reconstructed cluster energy. The final dependence of the difference between corrected cluster energy and simulated energy is shown in the bottom panel of Fig. 69.

#### 2.7.5 Energy Resolution

The energy resolution was estimated from the GEMC simulation assuming different thresholds on the single crystal readout and detector geometries. The distribution of the difference between the reconstructed cluster energy and simulated energy for a fixed electron momentum was fit with a Gaussian function and the  $\sigma$  from the fit was used to determine the energy resolution.

Fig. 70 shows the values obtained for electron momenta between 0.5 and 4.5 GeV, as a function of the electron (top) and virtual photon (bottom) momenta. The points of different colors shows the resolution for different constraints on the cluster reconstruction:

- light-green: no threshold on the single crystals and no space constraints on the transverse size of the cluster,

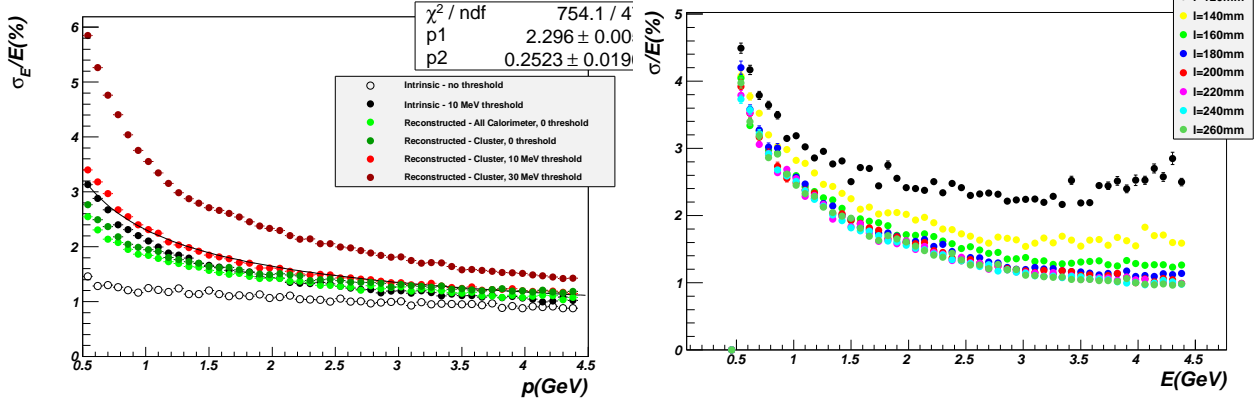


Figure 71: Energy resolution of the calorimeter for different values of the crystal length

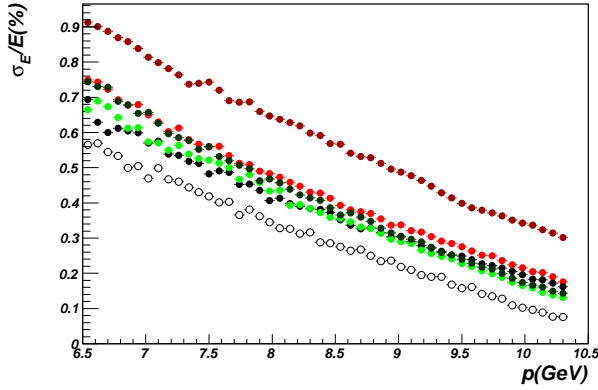


Figure 70: Energy resolution of the FT-Cal for the detected electron (top) and the inferred photon (bottom).

( $\sim 1\%$ ) that can be achieved given the specific detector geometry, while the difference between full and open circles gives a measure of the effect of the threshold. This is found to be one of the main contributions to the resolution of the calorimeter, while digitization effects and cuts on the cluster transverse size contribute for a fraction of a  $\%$ . Assuming to operate the calorimeter with a 10 MeV equivalent threshold, the final resolution is of the order of  $\sigma/E \sim (2.3/\sqrt{E} \oplus 0.5)\%$ .

- darg-green: no threshold on the single crystal but cluster transverse size equal to three times the Moliere radius,
- red: cut on the cluster transverse size and a threshold on the single crystal equal to 10 MeV,
- dark-red: cut on the cluster transverse size and a threshold on the single crystal equal to 30 MeV.

### Dependence on the crystal size

As a comparison, the resolution achieved excluding digitization effects is shown by the black points, with the open and full circles corresponding to 0 and 10 MeV threshold on the single-crystal signal. The open circles correspond therefore to the best resolution

The results described in the previous section were obtained for a crystal size of  $15 \times 15 \times 200 \text{ mm}^3$ . While the transverse size of the crystals was fixed based on considerations related to the PbWO Moliere radius ( $\sim 2 \text{ cm}$ ), the length was chosen based on the available space and of the results of a study of the dependence of the energy resolution on this parameter. Given the available space, the range of crystal length that could be considered is from about 12 to 26 cm. Fig. 71 shows the results of these simulations assuming a 10 MeV equivalent threshold on the crystal signal. The resolution both for the detected electron and for the inferred virtual photon energy shows a significant improvement when

the crystal length is increased from the the lower limit to 18 cm, while tends to saturate for higher values. This saturation is due to the dominance of other effects, such as signal digitization and threshold, over the longitudinal fluctuations of the shower for lengths larger than 18 cm. Similar findings were obtained by the ALICE-PHOS Collaboration in their simulation studies [22]. Based on these results, the crystal length for the FT-Cal was fixed to 20 cm.

### Dependence on the light readout system, crystal material and operating temperature

The dependence of the energy resolution on the scintillator material, on the operating temperature of the crystals and of the light sensors was studied performing detailed simulations of the calorimeter response assuming different light yield of the crystals (120 photons/MeV for PbWO-I @ +18°, 240 photons/MeV for PbWO-II @ +18° and 960 photons/MeV for PbWO-II @ -25°) and light readout based on SiPMs or APD. More specifically, the light sensors that were simulated are the following:

- $5 \times 5 \text{ mm}^2$  APDs with quantum efficiency of 70%,
- $10 \times 10 \text{ mm}^2$  APDs with quantum efficiency of 70%,
- $7 \times 14 \text{ mm}^2$  APDs with quantum efficiency of 70%,
- $2 \times 2$  SiPM arrays, based on  $3 \times 3 \text{ mm}^2$  sensors, with pixel size of  $25 \mu\text{m}$ , filling factor of 30% and effective quantum efficiency of 25%.

The results of these simulations are shown in Fig. 72: the resolution achieved for the smaller size APDs and SiPM arrays are comparable but significantly worse than the resolution for the  $10 \times 10 \text{ mm}^2$  or  $7 \times 14 \text{ mm}^2$  APDs that give the best performances. With these sensors, the resolution appears to be

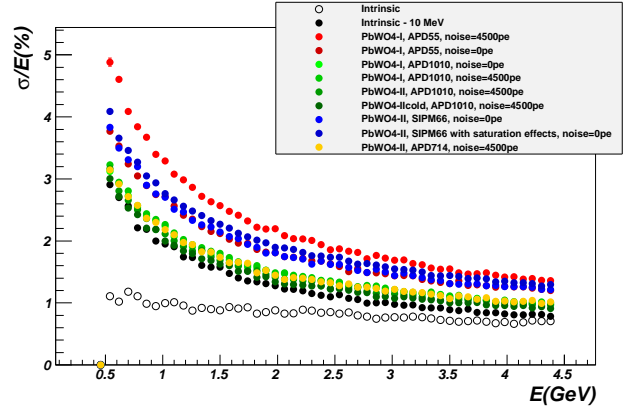


Figure 72: Energy resolution of the calorimeter for different light sensors, scintillator material and operating temperature. The different colors correspond to  $5 \times 5$ ,  $10 \times 10 \text{ mm}^2$  and  $7 \times 14 \text{ mm}^2$  APDs with different preamplifier noise level, to  $2 \times 2$  SiPM arrays with and without saturation effect related to the finite number of pixels, and to different light yields achieved for different crystal material and operating temperature.

only slightly dependent on the scintillator type, on the scintillator operating temperature and on digitization effects such as for example to the noise introduced by the preamplifier.

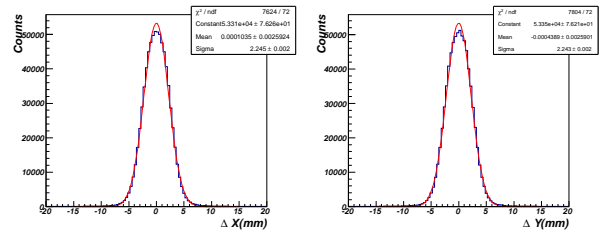


Figure 73: Spatial resolution of the calorimeter in the transverse directions.

### 2.7.6 Spatial resolution

The pixelized structure of the calorimeter allows to determine the impact point of the electron or photon inducing the electromagnetic shower by studying the transverse shape

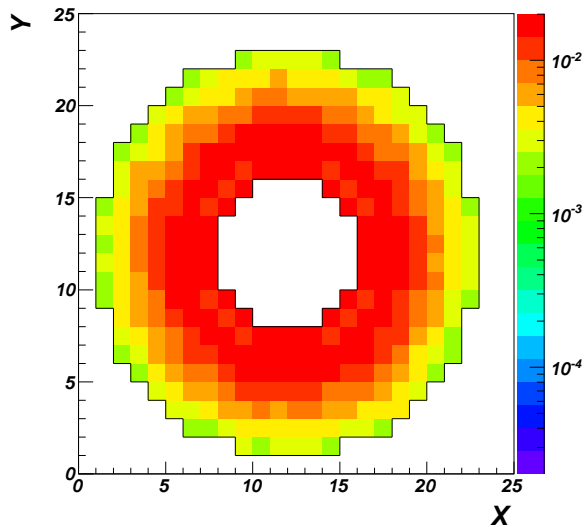


Figure 74: Simulation of the electromagnetic background with GEMC. Energy deposited in the calorimeter in MeV/ns

of the cluster. The best determination of the impact point is obtained by evaluating for each cluster the energy-weighted average of the  $x$  and  $y$  positions of the involved clusters. The resulting resolution is of the order of 2 mm as shown in Fig. 73.

### 2.7.7 Electromagnetic background rates

The electromagnetic background produced by the interaction of the electron beam in the target at the nominal CLAS12 luminosity was also simulated<sup>§</sup>. Fig. 74 shows the energy deposited in the calorimeter in MeV/ns: the maximum energy deposition per crystals is estimated to be less than 0.02 MeV/ns. Most of this dose is due to very low energy particles as shown by Fig. 75. The overall particle rate is of about 120 MHz with only 6% due to particles with energy above 100 MeV. In the energy range to be tagged (0.5-4.5 GeV)

<sup>§</sup>For this purpose, in each event, about 115000, 11 GeV, electrons were generated originating 10 cm upstream the target. The electrons were distributed randomly with the 2 ns radio-frequency structure of the CEBAF beam in a 250 ns window, which corresponds to the data acquisition window that will be used for the CLAS12 Drift Chambers. This number of electrons corresponds to the number of beam electrons that would pass through the target in the chosen time window at the nominal CLAS12 luminosity of  $10^{35} \text{ cm}^{-2} \text{ s}^{-1}$ .

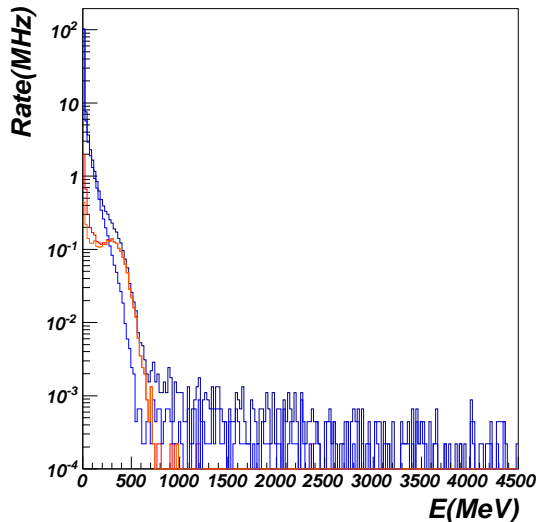


Figure 75: Simulation of the electromagnetic background with GEMC. Energy distribution of particles hitting the calorimeter front face (black-total, red-electrons, blue-photons).

the overall particle rate is further reduced to about 180 KHz, equally shared between photons and hadrons. This is relevant for the trigger rates evaluation described in Sec. 7.

The background impact on the reconstruction of “good” electrons has been studied analyzing in detail the time structure of these events. The relevant background is the one that overlaps in time with the electron signal. The time window that has to be considered is set by the duration of the preamplifier signals and should correspond to the time range in fADCs to obtain the signal charge. The rates and energy deposition were therefore evaluated in a time window of 110 ns, i.e. what was used in the test of the FT-Cal prototype described in the next sections. The results are shown in Fig. 76. The left plot show the number of hits in the calorimeter in the chosen time window while the right plot shows the energy deposition in MeV. Considering the characteristic of the expected signal for “good” electrons (minimum number of crystals of the order of 4 and a minimum energy deposition per crystal of 100 MeV), this background is negligible.

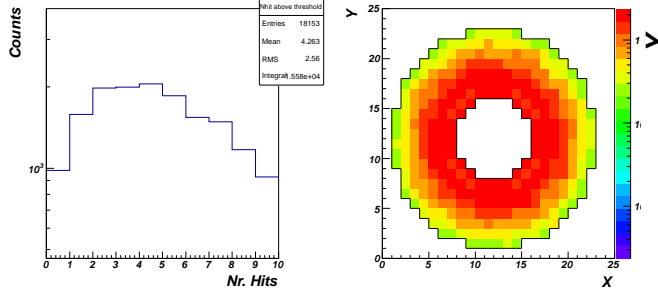


Figure 76: Left: number of crystals in the FT calorimeter with signal above threshold in a 20 ns time window due to the electromagnetic background at a luminosity of  $10^{35} \text{ cm}^{-2}\text{s}^{-1}$ . Right: distribution of the energy deposited in the calorimeter in a 20 ns window; the z-scale is in MeV.

### 2.7.8 Radiation dose

The results of the electromagnetic background study were used to estimate the radiation dose deposited in the FT crystals. Radiation dose can be a critical issue for the operation of scintillating crystals in high background environment since radiation induces a deterioration of the light transmission properties of the material due to the creation of color center in the lattice. These defects are not permanent and can be removed with an annealing procedure, that however may be unpractical during data taking.

The energy deposition in each crystal was evaluated from the background simulation and used to calculate the dose per unit of time. The overall radiation dose at  $10^{35} \text{ cm}^{-2}\text{s}^{-1}$  was estimated to be less than 1.5 rad/h when averaged over the entire calorimeter with a distribution on the calorimeter crystals as shown by Fig. 77. The maximum dose per crystal is of about 3 rad/h, which would result in an maximum integrated dose per crystal of about 2160 rad in 30 days of beam time. This is similar to what has been estimated for the existing CLAS-IC [24], where no significant worsening of the detector performance was observed.

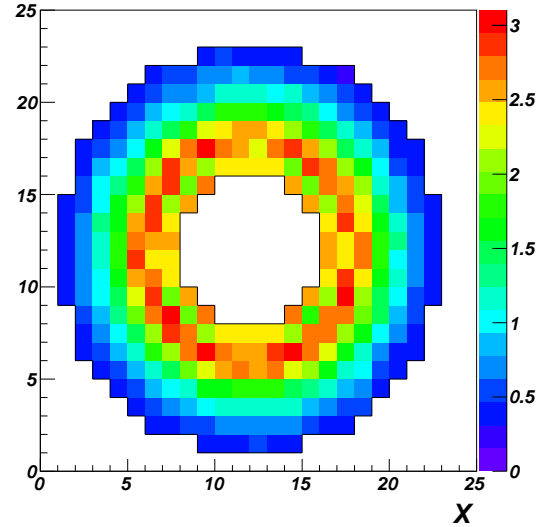


Figure 77: Radiation dose on the FT calorimeter crystals in rad/hour at  $10^{35} \text{ cm}^{-2}\text{s}^{-1}$  luminosity. The maximum values of about 5 rad/h are observed for the innermost crystals, i.e. at the smaller angles.

## 2.8 Prototype tests

Two prototypes of the FT-Cal, with 9 and 16 channels respectively, have been assembled and tested with cosmic rays and electron beams. The prototypes were used to check the single crystal mechanical assembly, the thermal performance, the front-end and read-out electronics, the electrical connections via a motherboard. The response to cosmic rays was studied for both prototypes while the response to electromagnetic shower was studied at JLab and LNF. The Proto-9 has been tested at JLab using 2-3 GeV electrons deviated by the Hall-B tagger system while the Proto-16 has been tested at the Beam Test Facility of LNF with a 0.7 GeV electron beam. Extensive simulations have been performed and compared to the results of the two sets of measurements. Main goals of tests were:

- to measure the energy resolution as a function of single-crystal threshold;
- to measure the energy resolution as a

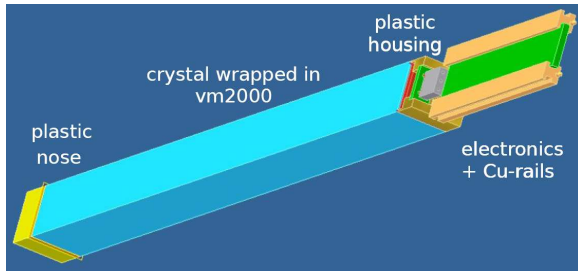


Figure 78: Proto-9 single crystal assembly.



Figure 80: Proto-9 picture.

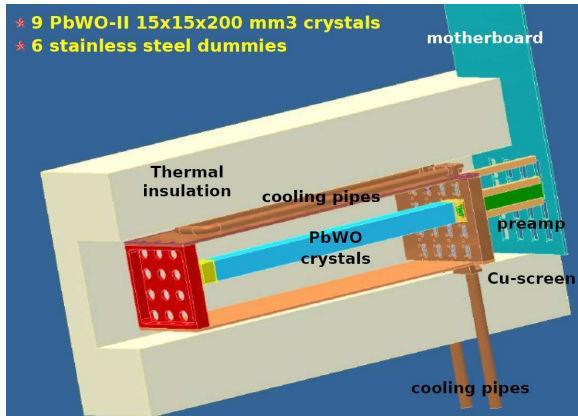


Figure 79: Proto-9 full assembly.

function of  $T$  ( $+18^\circ$ ,  $0^\circ$ ,  $-10^\circ$ ,  $-25^\circ$ );

- to measure the time resolution;
- to verify the system linearity;
- to check rate performances;
- to validate GEMC simulations;
- to measure the electronic noise in realistic conditions;
- to perform detailed studies of electromagnetic shower signal: shower profile, APD signal shape, and test of filtering algorithm.

### 2.8.1 The Proto-9

In the first version of the prototype we assembled 9 BTCP crystals and 6 stainless-steel dummies in a mechanical structure that simulated the real assembly. Each crystals, wrapped in a VM2000 foil, was read by a Hamamatsu S8664-1010 LAAPD, an FT-Orsay pre-

amplifier connected to the motherboard, grounded by using two copper rails and hold by a PEEK support in the front. Figure 78 shows all components of the single crystal assembly. The 9 crystals were then inserted in a mechanical structure made by two copper plates where a pipe was soldered for cooling. Only one side of the 3x3 matrix has been cooled in order to reproduce the realistic condition of the final mechanical assembly where crystals are cooled only from the the external side of the cylinder. Figure 79 shows the full assembly. The detector was then inserted in a gas- and light-tight box surrounded by 5 cm thick insulation. An external chiller provides the necessary cooling power to operate the prototype in a temperature range between  $0^\circ$  C to  $+18^\circ$  with a thermal stability of  $0.1^\circ$  C. A system flushing of dry  $N_2$  prevented moisture formation within the box when the prototype was operated below the dew point. A picture of the plastic box with cooling pipes and signal connectors is shown in Fig. 80.

The Proto-9 response to cosmic muons was measured in Genova. The experimental setup is reported in Figs. 81. The detector was inserted within three plastic scintillator bars read by each side by a PMT. The 6-folds coincidence of the PMTs triggered the data acquisition. The hit position along the bar was reconstructed by the time hit difference allowing a precise geometrical tracking of the muon track. The time resolution of the over-constrained trigger system was estimated to be 75 ps. Figure 82 shows the energy distri-

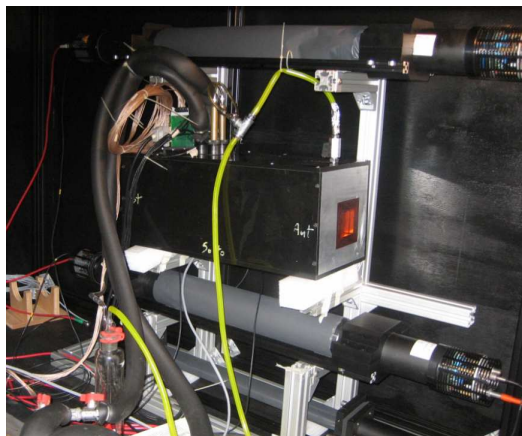
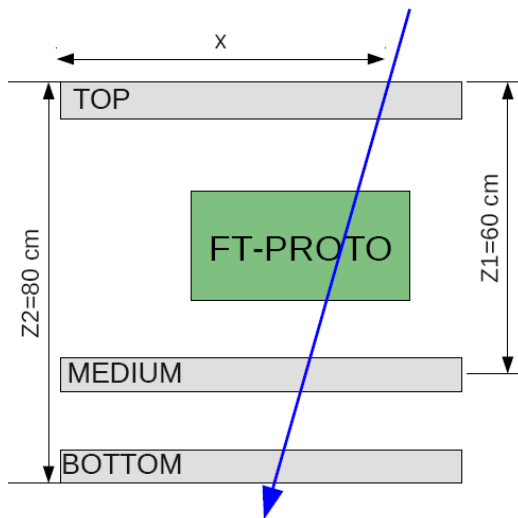


Figure 81: The experimental set-up used to measure the Proto-9 response to cosmic muons.

Contributions of the cosmic muons detected in one of the crystals of the Proto-9.

The detector was operated at different temperatures confirming the light yield dependence measured with a single crystal setup (see Sec. 2.1.3). Figure 83 shows the LY as a function of the temperature,  $T$ , measured in different experimental conditions: single-crystal with PMT readout in red; single-crystal with APD readout) in green, Proto-9 results in black. All results are consistent showing an increase of a factor 2.7 between  $+18^\circ$  and  $-25^\circ$ .

The Proto-9 response to electromagnetic shower was tested at JLab using diffused electrons from the real photon Bremsstrahlung

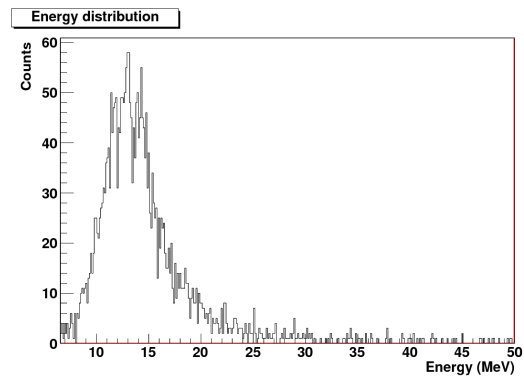


Figure 82: Cosmic-ray energy distribution measured by a single crystal of Proto-9.

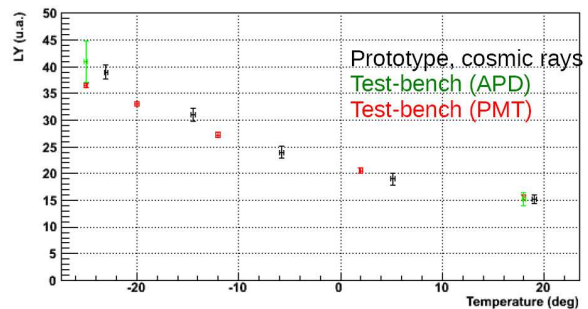


Figure 83: Light yield as a function of the crystal  $T$  measured with different experimental set-ups.

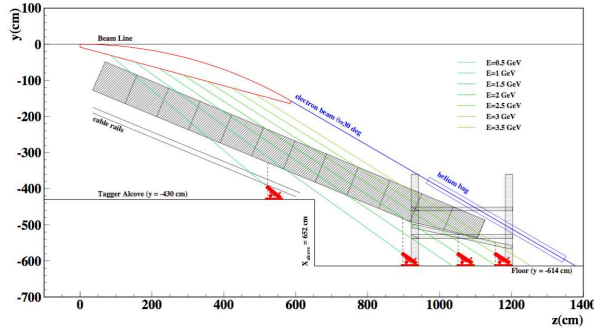


Figure 84: Proto-9 positioning under the tagger hodoscope in Hall-B at JLab.

radiator during a photoproduction experiment. The prototype was placed below the Hall-B tagger hodoscope to detect electrons after their interaction with the  $E$  and  $T$  tagger counters. Figure 84 shows a sketch of the Hall-B tagger system and the positioning of the Proto-9.

The energy resolution of the Proto-9 detector was evaluated by means of Monte Carlo simulations. The tagger components (plastic scintillators) the air gap and all the other passive materials were included in the detector description in order to obtain a realistic estimate of the expected resolution. Figure 85 shows the energy resolution as a function of the incident electron energy. Different colors correspond to different thresholds on the collected energy on each crystal. The test conditions corresponds to an energy threshold of 10 MeV (blue dots). The response to two different energies, 1.31 GeV and 1.92 GeV, was measured by changing the primary electron beam energy from 2.282 GeV to 3.356 GeV. For these energies, the expected resolutions are 2.2% and 1.9%, respectively. The typical signal produced by an electron hitting the central crystal is reported in Fig. 86. The plot shows the 9 crystals matrix with the shower maximum in the central one. The noise level, well visible in channel 8, shows an RMS of 8 LSB corresponding to 4 mV ( $\sim 8$  MeV) and therefore indicating an effective energy threshold of 10 MeV for this ex-

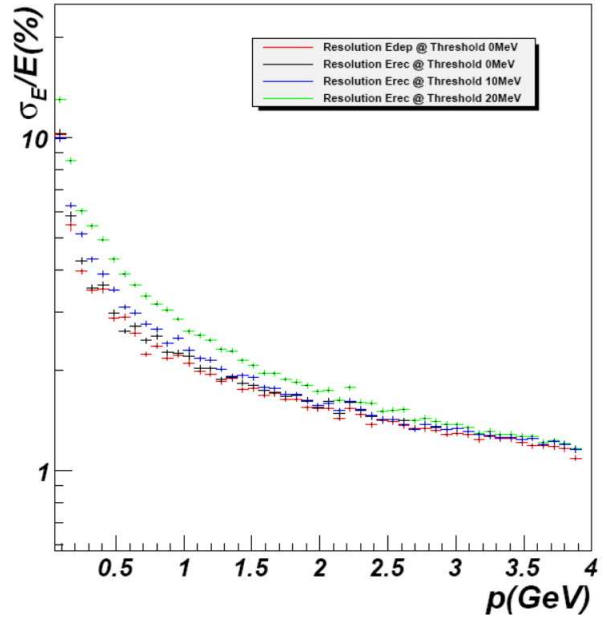


Figure 85: Expected resolution of the Proto-9 detector as a function of the incident electron energy and different threshold on the minimum detectable energy.

perimental setup. The excellent performance of the FT-Orsay preamplifier did not require any digital filtering. The total energy deposited in the prototype was obtained summing up the contributions of the 9 crystals after equalizing the peak position to match the individual gains. Figure 87 shows the energy resolution obtained with 1.31 GeV (top) and 1.92 GeV electrons (bottom). In the upper plot, the distribution is peaked around  $E_{measured}=1.1$  GeV ( $E_{true}=1.31$  GeV) because of the side leaks with a relative  $\sigma$  of  $\frac{\sigma_{E_{true}}}{E_{true}} = 2.5\%$  ( $\frac{\sigma_{E_{measured}}}{E_{measured}} = 3.0\%$ ). Results for electrons with  $E_{true}=1.92$  GeV are shown in the bottom plot:  $E_{measured}=1.6$  GeV and  $\sigma$  of  $\frac{\sigma_{E_{true}}}{E_{true}} = 2.2\%$  ( $\frac{\sigma_{E_{measured}}}{E_{measured}} = 2.64\%$ ) with the expected scaling behavior proportional to the  $\sqrt{E}$ .

### 2.8.2 The Proto-16

An improved version of the prototype, Proto-16, was built assembling 16 crystals in a  $4 \times 4$  matrix (8 provided by the BTCP and 8

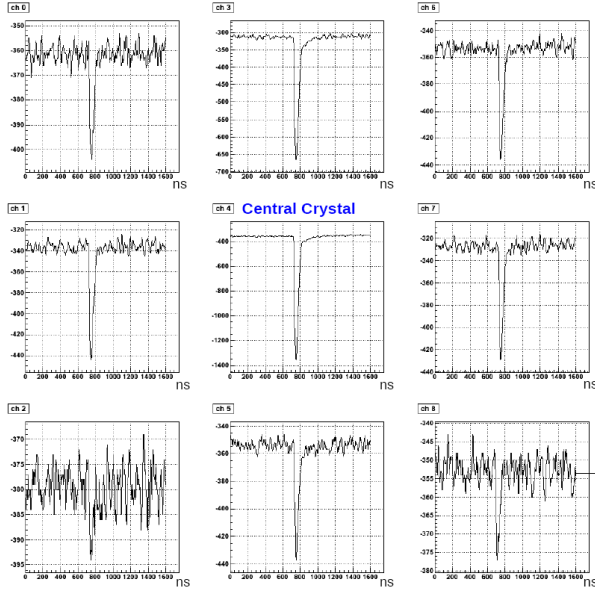


Figure 86: Signal induced by an electromagnetic shower in the 9 crystals of the Proto-9 matrix.

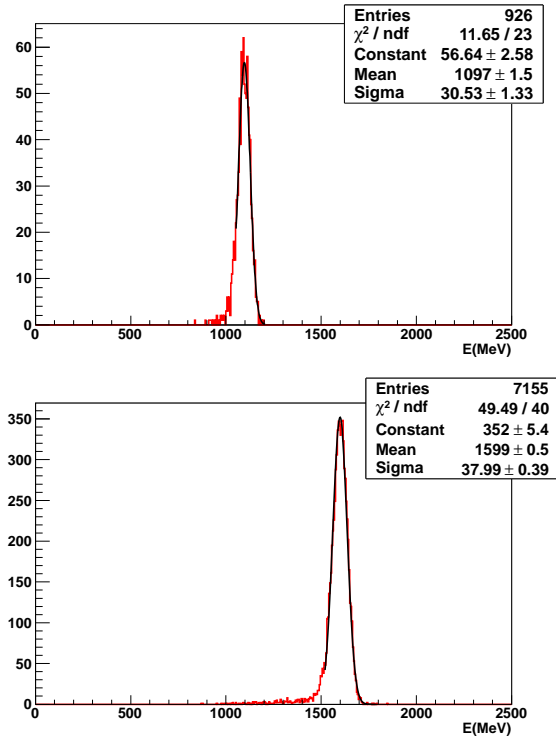


Figure 87: Energy resolution obtained with 1.31 GeV (top) and 1.92 GeV electrons (bottom).

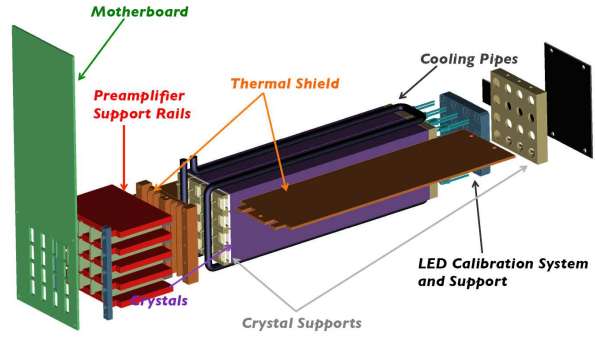


Figure 88: Exploded view of the Proto-16 assembly

from the RIINC company). The mechanics of the Proto-16 was modified compared to the Proto-9 based on the experience gained with the previous prototype. Figure 88 shows the Proto-16 components. In particular, the crystal assembly procedure was improved by implementing the usage of dedicated tools for the APD and wrapping gluing, as well as detailed quality assurance procedures. The grounding of the FT-Cal preamplifiers was improved by replacing the separated rails with horizontal copper plates with carved slots for the insertion of the PCBs. The cooling system was simplified by soldering the cooling pipe to the thermal shield and to the back plate, which is shaped to host a 5-mm pipe. The new LED calibration system was also mounted in front of the crystal matrix and used for the initial tests of the system. All these new features are included in the final design of the FT-Cal that was presented in the previous sections.

Due to the larger crystal matrix, the expected performance of Proto-16 in terms of energy resolution are similar to what expected for the the FT-Cal. A comparison of the expected energy resolution is shown in Fig. 89. The green points correspond to the expected performance of Proto-16 with a minimum energy threshold per crystal of 10 MeV. These almost superimpose to the black dots that show the expected resolution for the whole FT-Cal with the same threshold.

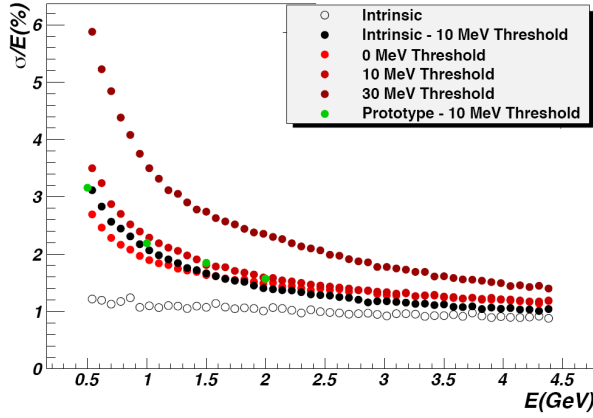


Figure 89: Expected resolution of the Proto-16 detector as function of incident electron energy and different threshold on the minimum detectable energy per crystal.

The Proto-16 was tested at the Beam Test Facility (BTF) [40] of the INFN Frascati National Laboratory, using a 500 MeV electron beam. Two separate runs were performed in May 2012 and October 2012: here we report the results of the later run, where the prototype resolution was studied as a function of the energy and calorimeter temperature. The BTF electron beam is characterized a repetition frequency of 50 Hz and a pulse duration of 10 ns. The beam intensity can be varied by operating different sets of slits, selecting the number of electrons per bunch at the level of a single particle. The prototype performance can therefore be studied as a function of the number of electrons hitting simultaneously the crystal matrix, i.e. of the detected energy.

Fig. 90 shows the experimental hall after the installation of the Proto-16 and associated equipment. The detector was placed on a moveable table that can be displaced in the x and y direction with 0.1-mm accuracy. This feature was exploited to center the calorimeter with respect to the beam. A plastic scintillator bar, read by two PMTs, was placed in front of the beam pipe exit window and was used to determine the arrival time of the electron within the 10-ns bunch duration. The



Figure 90: Experimental setup in October Proto-16 test at the Frascati Beam Test Facility (BTF).

data acquisition, based on the JLAB DAQ standard CODA, was triggered by the RF signal of the Frascati accelerator. For each trigger all the signals of the Proto-16 crystal matrix and of the scintillator-bar PMTs were recorded by CAEN VME boards. Both the Proto-16 and scintillator signals were sent to a passive splitter whose two outputs were connected the 250 MHz fADCs and to leading-edge discriminators. The discriminator output was sent to pipeline TDCs. The whole electronic chain, even if not yet based on JLab fADCs and discriminators, is fully compliant with the CLAS12 front-end electronics and DAQ.

**Pulse digitization and reconstruction** The samples recorded by the fADCs in a 800 ns window were recorded for each trigger and analyzed offline to evaluate the charge and time of any detected pulse, using the following procedure. The signal pedestal were computed for each channel on an event-by-event basis, averaging the first 40 samples and recording the mean and the  $\sigma$ . The presence of a pulse in the remaining samples was detected by requiring at least one sample exceeding the pedestal values by at least  $4\sigma$ . If a pulse was detected, the adjacent samples exceeding the pedestal by at least  $3\sigma$  were summed to es-

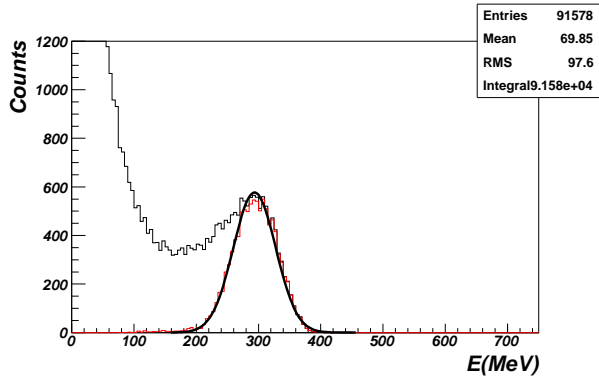


Figure 91: Energy spectrum of a single crystal for event with one 500 MeV electrons hitting the prototype. The black histograms includes all events while the red on is obtained requiring to have less than 200 MeV detected energy in the neighboring crystals.

estimate the pulse charge. For each pulse, the highest sample defined the pulse peak amplitude and position. The samples preceding the peak position were processed to obtain the signal arrival time, using the same algorithm that is presently implemented on the FPGAs of the JLab fADCs.

**Energy calibration** The conversion between charge and energy of the pulses detected in the Proto-16 was first determined using the calibration constants derived by cosmic ray measurements. The calibration constants were then optimized at the Frascati BTF by studying the response of each crystal to 500 MeV electrons. For this purpose, different runs were recorded displacing the Proto-16 with respect to the beam to have electrons hitting each of the 16 PbWO crystals. Events with only one 500-MeV electron hitting the calorimeter were selected by cutting on the total reconstructed energy; the response of each crystal was evaluated by requiring to have less than 200 MeV detected in the neighboring crystals. Fig. 91 shows the single crystal spectrum when no cuts are applied in black and with the cuts outlined above in red. The procedure was applied to all the 16 crystals,

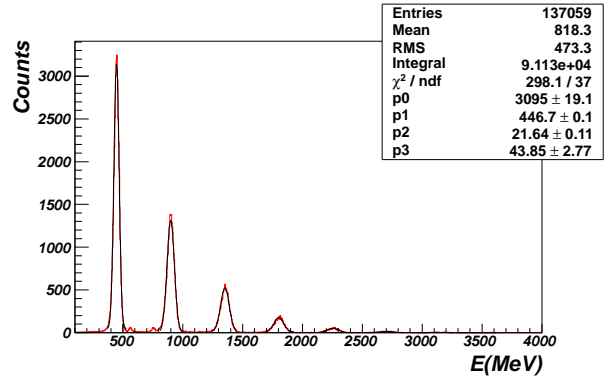


Figure 92: The total energy detected by the Proto-16 after the full calibration is shown in Fig. 92 for an electron multiplicity of the order of 1. The peaks corresponding to different bunch population are clearly visible and well separated.

aligning the position of the peak in the red histograms to the same value by applying multiplicative factors to the charge-to-energy conversion parameter. The total energy detected by the Proto-16 after the full calibration is shown in Fig. 92 for an electron multiplicity of the order of 1-2. The peaks corresponding to different bunch population are clearly visible and well separated. These peaks were fitted with gaussian functions to determine their position and width. The previously determined calibration constants were multiplied by a common factor to align the position of the single-electron peak at 440 MeV, which, according to GEANT4 simulation, is the total energy deposited in the Proto-16 by a 500 MeV electron.

After completing this procedure, the new calibration constants were found to be within 5-10% from the initial values determined with the cosmic-ray data taking: this an important fact since it indicates that initial calibration for the whole FT can be done without beam.

**Energy resolution** The mean values and  $\sigma$  of the peaks in the total reconstructed energy spectrum were analyzed to check the system linearity and determine the resolution. The measurements were performed by cen-

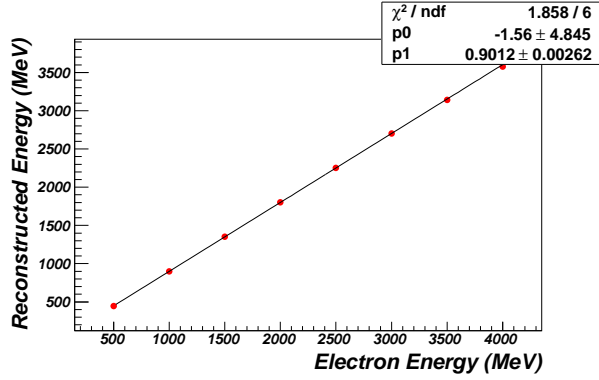


Figure 93: Proto-16 reconstructed energy as a function of the beam bunch energy. The red points were obtained at room temperature and with a APD gain of 150. The linear regression of the experimental points show no deviation from linearity.

tering the beam on the calorimeter to have the maximum containment of the electromagnetic shower. This was repeated varying the Proto-16 configuration and in particular:

- varying the APD HV to have a gain  $G=150$  or  $G=75$ ;
- varying the temperature of the PbWO crystals from room temperature ( $+18^\circ$ ) to  $0^\circ$  and  $-20^\circ$ ;
- connecting the output of the preamplifiers directly to the fADC, removing the passive splitter and therefore simplifying the electronic chain.

The purpose of these tests was to determine the optimal operating temperature of the calorimeter, to choose the optimal gain for the APDs and to select the best configuration of electronic chain. Fig. 93 shows the fitted peak position as a function of total energy in the beam bunch for APD gain of 150 and PbWO temperature of  $18^\circ$ . The linear regression of the experimental points show no deviations from linearity in the explored range. The same measurement performed in different configurations gave consistent results, confirming that the system is linear up to the maximum measured energy of 4 GeV.

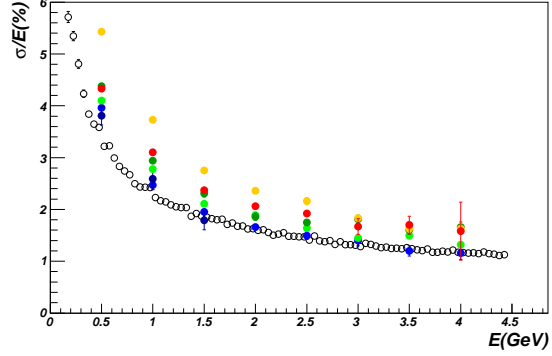


Figure 94: Proto-16 energy resolution as a function of the beam bunch energy. The red and orange points were obtained at room temperature for an APD gain of 150 and 75, respectively. The green points correspond to  $0^\circ$  degrees; the darker points were obtained removing the passive splitter. The blue and dark-blue points correspond to  $-20^\circ$  with APD gain of 150 and 75, respectively. The open black circle show the expected resolution based on GEMC simulations. Only statistical errors are shown.

Fig. 94 shows the energy resolution as a function of the energy in the beam bunch. The colored points correspond to the resolution measured with the Proto-16 while the black open circle are the results of the GEMC simulations. The error bars in the graph show the statistical uncertainty while the systematic uncertainty was estimated to be in the order of 5%. As expected, the experimental resolution increases for increasing energy, reaching an asymptotic behavior at about 3 GeV. The measurements performed in different configuration are in general consistent, varying within a range of 0.5% except for the resolution obtained at room temperature and  $G=75$  (orange points). The resolution in this case is systematically worse than what obtained at the same temperature but  $G=150$ . This was interpreted as due to the preamplifier noise being the dominant factor in determining the resolution at this temperature. From this we concluded that working at high APD gain is the preferable configuration.

The comparison of the resolution obtained at different temperature show that lower temperatures, corresponding to higher light yield and therefore larger signal, give better resolution. The best values were obtained at  $-20^\circ$ , where the experimental points are in good agreement with the simulation results. The dependence of the resolution on the temperature is more evident for high bunch energies, where threshold effects are smaller. Above 2 GeV, the resolution at room temperature seems to be systematically higher than the one obtained at  $0^\circ$  or  $-20^\circ$  with a difference of about 0.5%. The difference of the resolution obtained at  $0^\circ$  and  $-20^\circ$  is on the contrary quite small and negligible within the systematic errors. Based on this results and considering the technical difficulties in operating the FT-Cal at very low temperature, we concluded that the optimal operating temperature of the calorimeter is  $0^\circ$ .

Finally the comparison of the light and dark green points show that no significant difference is observed when the passive splitter is removed and the preamplifier signals are connected directly to the fADC. This indicates that similar energy resolution can be achieved both in the case fADCs and TDCs will be used or in the case fADCs will be used both for energy and time measurement.

## 2.9 Planning, costs and funding

### 2.9.1 Planning

The FT-Cal project is distributed over 4 years. The starting date back to the presentation of the MesonEx proposal to the JLab PAC in January 2011 and its approval few months later. From this date, 1 year was devoted to the R&D phase on the different components of the FT-Cal: PbWO crystals, light sensor, preamps and LED monitoring system. In year 2012 we started the procurement of the PbWO crystals by calling an international bid that is expected to end by 2013. At the same time the  $\sim 400$  preamplifiers (FT-Orsay)

have been ordered from Orsay. In year 2013 the APD procurement is also expected. The readout electronics has partially been ordered (JLab fADCs) expecting to complete the procurement for the beginning of 2014. We are currently working on the mechanical design interacting with engineers at JLab. The full FT mechanical design is expected to be ready for the beginning of year 2013. The full FT-Cal assembly is expected to happen in Genova at the end of 2014. The FT will then be moved to JLab where we plan to install it in CLAS12 in spring 2015, to be ready for the detector checkout and commissioning expected for the end of the same year. The MesonEx experiment is expected to be the first to run in the Hall-B. During the procurement phase, we are running an extensive program of tests and measurements with the detector prototypes in order to finalize the thermal and mechanical design of the FT-Cal components.

The INFN-GE, together with the other institutions involved in the project, University of Edinburgh, CEA-Saclay, Ohio University, James Madison University and Norfolk State University, is committed to develop and apply a detailed commissioning plan for the FT system in collaboration with the CLAS12 Calibration and Commissioning Committee. The full plan is presented in Sec. 6. We are also committed to provide the necessary software for the FT online monitoring and the offline FT calibration. A preliminary Java version of the FT-Cal online monitoring has already been developed and implemented in the standard online monitoring procedures of CLAS12 software group. A complete monitoring/calibration package is expected for the end of year 2014. This will be tested with cosmic ray and on-beam tests. FT calibration procedures will be developed in advance and optimized during the FT commissioning at JLab.

Item	Description	N	€/ch	Total k€
Crystals	PbWO Type-II	330+40	0.4	150
Light sensors	LAAPD S8664-1010	330+40	0.5	185
RO electronics	fADC/Discr/TDC	330+40	0.5	185
FE electronics	FT-Orsay preamps	330+40	0.06	20
Monitoring	LED system			40
LV/HV/Cables	Crates/boards			40
Cooling	Chiller/pipes/T monitor			20
Mechanics				15
Trigger	Jlab boards			15
Total				670
Grand Total	VAT(21%) and contingency(10%)			892

Table 11: Cost estimate for the FT-Cal components.

### 2.9.2 Costs

Table 2.9.2 shows the cost estimate for the FT-Cal (R&D is not included).

### 2.9.3 Fundings

The FT project has been included in the INFN 6-years funding plan (2009-15) providing full financial support for the FT-Cal construction and FT mechanical assembly. The FT technical design report has been evaluated and refereed by a dedicated INFN Review Committee: about 0.5M € has already been allocated for R&D and construction and other 150k € are foreseen for the near future to complete the calorimeter and the mechanical assembly of the FT. Other funds ( $\sim 30\text{k€}$ , mainly for personnel) were also collected from the HP3 initiative within EU FP7.

## 3 FT-Hodo

### 3.1 Design Requirements

The primary task of the Forward Tagger Hodoscope (FT-Hodo) will be to separate electron and photon events in the calorimeter. These events cannot be distinguished using information from the FT-Cal alone due to the similarity of their electromagnetic shower shapes. Electrons will be identified by observing the presence of a hit in the FT-Hodo array, which is correlated in both position and time with a cluster observed in the calorimeter.

The main design requirements of the FT-Hodo are to provide a highly efficient charged particle signal with a spatial and timing resolution similar to that of the calorimeter. Further, to minimise possible misidentification of photons the detector should be designed to (i) suppress the contribution of false events arising from photon conversion in the FT-Hodo detectors and (ii) suppress contributions from the “splashback” of the electromagnetic shower created by events depositing energy in the FT-Cal. As discussed in section 3.3.2 this requires a 2 layer design. The timing resolution of FT-Hodo should be comparable with FT-Cal so as not to compromise the achievable coincidence timing resolution. This requires a timing resolution of the order 1 ns or better. The accurate timing would also allow its potential future use in experimental trigger decisions. The hodoscope will be located within CLAS12 in a region where the combined magnetic field from the solenoid and torus is sufficiently large to render conventional photomultiplier tubes unusable.

The detector geometry and readout is constrained by the surrounding apparatus. The device will be positioned upstream of the FT-Cal, fitting into a circular disk of diameter 330 mm and depth 42 mm.

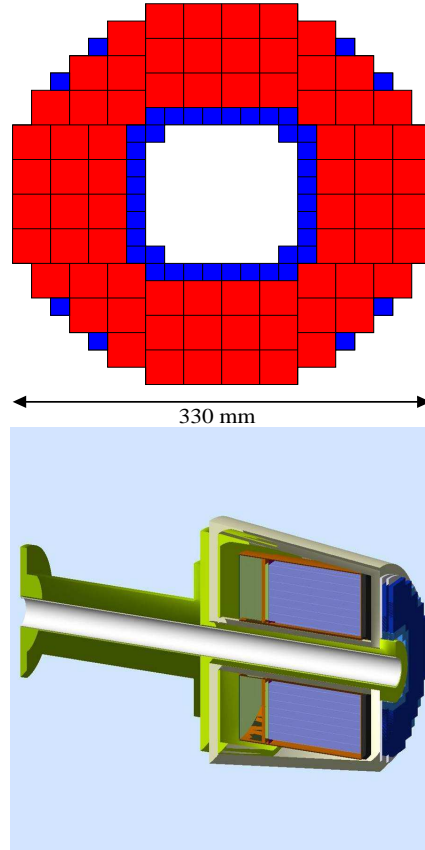


Figure 95: upper: Layout of plastic scintillator detectors in FT-Hodo. Blue squares represent 15 x 15 mm pixels and red 30 x 30 mm. lower: Geant4 visualisation of the position of the 2 hodoscope detector planes (dark blue). The FT-Cal crystals (light blue) and shielding are also shown

#### 3.1.1 Design

A FT-Hodo detector which meets these design requirements has been developed. It comprises a segmented array of plastic scintillator tiles (Eljen-204), embedded with wave length shifting (WLS) fibres (Kuraray K11) and read out by Hamamatsu 3x3 mm<sup>2</sup> silicon photomultipliers (SiPM) via optical fibres. The plastic scintillators provide fast timing and sufficient resistance to radiation damage for use in the high rate environments of the Forward Tagger. The need to minimise material outside of the active area of the hodoscope, to operate in high magnetic fields and tolerate the high background ra-

diation environment necessitates the scintillation light from the detector elements to be transferred away from the hodoscope for analysis. This is achieved by embedded WLS fibres which are fusion spliced to 5m long optical fibres. The WLS fibres absorb the UV light produced in the plastic scintillator and emit at a larger wavelength (green), which matches well with the optimal quantum efficiency of typical SiPMs. The WLS fibre has a relatively small attenuation length ( $> 3.5$  m). These will be fusion spliced at a distance of 10cm from the scintillator tile to clear 5 m length optical fibres which have attenuation length  $> 10m$ . The splicing induces a photon loss of less than 2%. The use of optical fibre allows the captured light to be transported with a light loss less than  $\sim 40\%$  over the 5 metre path to the SiPM.

### 3.1.2 Detector Element design

To match the geometry of the FT-Cal the hodoscope requires pixels of  $15 \times 15$  mm (P15) covering a single crystal and  $30 \times 30$  mm (P30) covering an array of four crystals. The arrangement of these detector elements to make up a layer of the hodoscope is shown in Fig. 95. To increase the number of scintillation photons collected from each tile they will contain multiple embedded WLS fibres, 2 for P15 and 4 for P30. The fibres will be embedded in grooves angled into the scintillator block (see Fig. 96). This choice ensures that the detector elements can touch at their interface without interference from the fibres. The WLS fibres will be surrounded on all sides by scintillator and have an increased path length in the scintillator than a surface groove design. Each pixel will be painted with Bicon BC620 reflective paint to optically isolate each detector element. This has a similar reflectivity (95%) to reflective wrappings such as Mylar.

Each fibre will be glued in position, using Bicon BC600 glue. The fibre will be Kuraray Y11, chosen because of its established resistance to radiation and its good timing

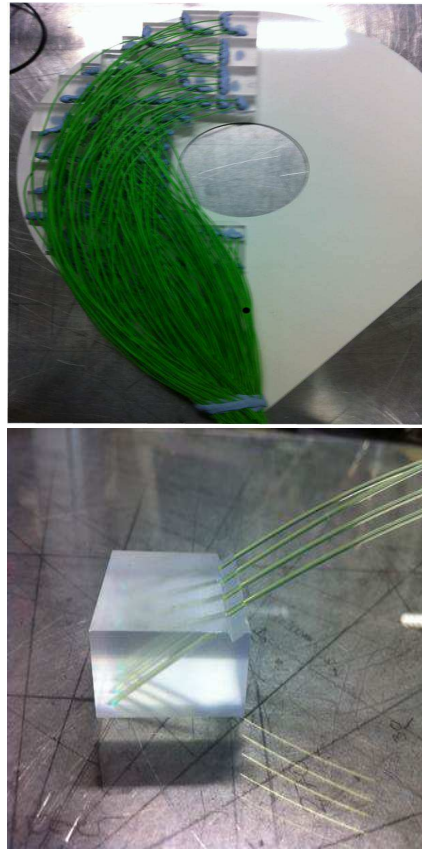


Figure 96: upper: A mock up of the hodoscope made from sized perspex blocks and using cable sheaths to show the route of the optical fibres. lower: A single scintillator element with diagonal holes drilled to accommodate the fibres.

properties. The fibre has been used successfully in other detectors such as the hodoscope used with the inner calorimeter of CLAS [27].

The hodoscope will comprise 2 detector layers, each having 44,  $15 \times 15$  mm (P15) and 72,  $30 \times 30$  mm (P30) pixels as shown in Fig. 95. One layer will be made from 7 mm thick plastic scintillator tiles with the second utilising 15 mm thick tiles. A two layer solution is the preferred option for the hodoscope. The thin (7 mm) front layer of the hodoscope is employed to reduce photon conversion in the hodoscope while the thicker (15 mm) back layer provides a signal with a large number of photoelectrons at the SiPM, giving the most accurate timing information

for the event. The Geant4 simulations and pseudo-analyses illustrating these benefits are outlined in section 3.3.2.

The hodoscope will utilise 3 x 3 mm Hamamatsu S10362-33-100C SiPMs, which can easily accept the maximum of 4x1 mm fibres to be readout by each SiPM. The SiPMs have 100 micron pitch and a quantum efficiency of  $\sim 50\%$ . The maximum number of photons to be input to a SiPM from the hodoscope will be 200. The 100 micron pitch is suitable for such a multiplicity as can be seen in Fig. 97 where the calculated SiPM pixel multiplicity is plotted versus the number of incident scintillation photons for different pitches of SiPM. The smaller pitch designs have significantly lower quantum efficiency and so were not considered. The SiPMs provide a cost effective solution to reading out a large number of channels. Manufacturers other than Hamamatsu were investigated but others were found to have inferior quality. Conventional multianode photomultiplier tubes were also considered but were rejected as they had a quantum efficiency less well matched to the output of the WLS fibres.

The SiPMs will be located  $\sim 5$  m away from the detector, next to the readout electronics. Locating the amplifiers and SiPMs in this region ensures there is minimal additional material introduced around the hodoscope and that the detectors will be located in a region of lower background radiation.

### 3.1.3 Mechanical structure and readout

The hodoscope scintillator tiles will be painted in reflective paint and held in position on the surface of a 2 mm thick plastic support board. This board will be formed from two 1 mm plastic sheets which will be cut to the geometry of the hodoscope and bolted together. This will allow the 2 layers of the hodoscope to be separated for maintenance and also to offer flexibility in the deployment of the detector in future experiments.

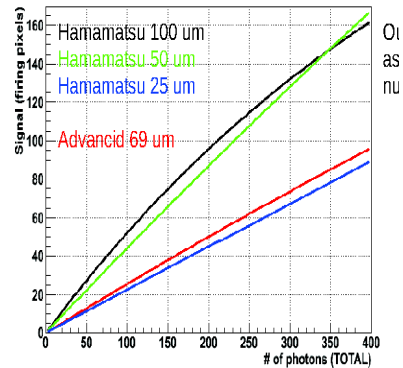


Figure 97: upper: Picture of the SiPM to be used in the hodoscope. lower: Simulation showing the effect of pixel size on the linearity of the output for the 4 fibre design to be used in the hodoscope.

A mock up of half of one layer of the detector has been made to aid the design of the detector (Fig. 96). The routing of the wavelength shifting fibres from each of the tiles has been explored using this mock-up and the configuration shown in the figure was the preferred option. There are 2 designs for the WLS entry point into the tiles (i) corner entry (74 tiles per layer) or (ii) side entry (42 per layer). The fibres exiting the tiles will need 9 mm clearance so as to be able to route easily to the bottom of the hodoscope. The total clearance needed for the 2 layers of the hodoscope is then 42 mm given by sum of scintillator thicknesses (22 mm), support structure (2 mm) and WLSF clearance (18 mm).

The WLSFs will be fusion spliced to clear

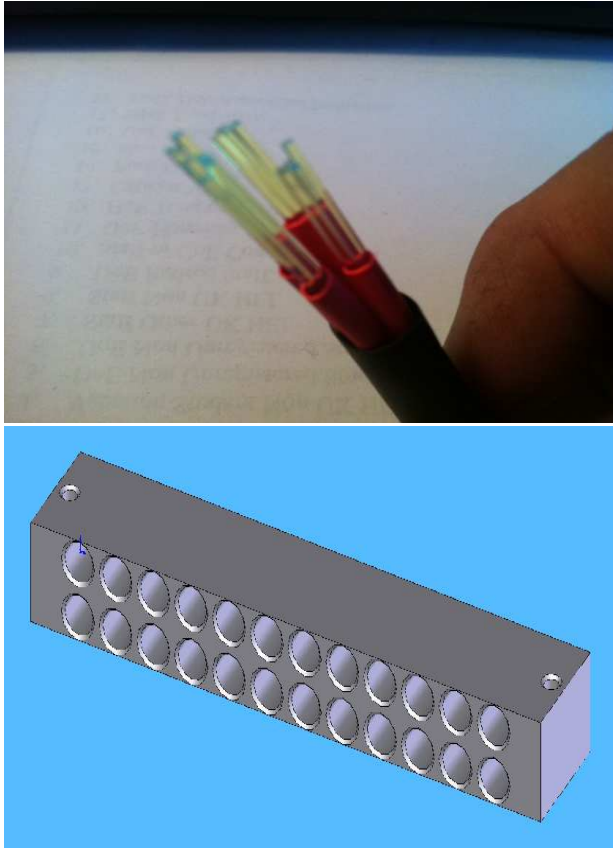


Figure 98: upper: The proposed sheathing system for the 1 mm thick optical fibres. Bunches of 4 fibres (usually from a single detector element) are grouped into 4 to make a bundle. lower: CAD drawing of the block connector which attaches the bundle sheaths to the hodoscope mounting board.

optical fibre (KURARAY CLEAR-PSM) at a distance of  $\sim 10$  cm from the hodoscope tile. The optical fibre has an attenuation length of  $\sim 10$  m. These fibres will be grouped into bunches of 16 as shown in Fig. 98. Groups of four will be sheathed in colour coded light-proof sheaths and these inserted into a larger “bundle sheath”. This system was chosen to allow clarity in the optical connections within the detector to the SiPMs located a significant distance away. The bundles of 16 fibres offer reasonable flexibility and the minimum bend radius of the bunch is approximately 25cm.

The sheathed bundles will be attached to the hodoscope mounting board using a block connector (Fig. 98). Each bundle sheath will be  $\sim 8$  mm in diameter so the block connector will have dimensions of 121 mm wide with 20 mm depth and 18 mm clearance from the mounting board (Fig. 99). The bundle sheaths will be glued in place in the cylindrical mounting holes of the connector block. The joints will be sealed at both ends using an optical sealant. The sheath will extend beyond the connector block by  $\sim 5$  mm to give a good contact to optically seal the connection. The design has 24 mounting holes allowing a total of 384 fibres per layer to be routed. Each layer of the hodoscope requires 376 fibres so the design will allow 8 spare fibres to be routed into the hodoscope which may facilitate repairs if necessary. The spare fibres will also provide optical fibre inputs to the light tight section of the hodoscope which will provide a route for pulsed light, which can be captured by the fibres and used in testing.

The 48 bundle-sheaths from both layers will be routed vertically downward from the hodoscope. The route of the fibres near to the hodoscope is shown in Fig. 100. The bundles will be routed via a support tray to the location of the electronics, covering a total distance of  $\sim 5$  metres. The bend radius is taken to be around quarter of a metre, compatible with tests using fibre bundles made up in Edinburgh. The optical interface to the electronic modules will be a plastic router module, each of which takes 2 bundle sheaths and guides them to 8 separate SiPMs (Fig. 101). The fibres will exit the router through 4 separate matrices of holes, with dimensions matched to the size of the SiPM. The fibres will be glued into the holes and then the protruding fibres will be cut and polished down until they are flush with the outer surface of the router. This will provide a reliable light connection to the SiPM. A similar glue and polishing technique was employed in beam tests of the detector modules at Frascati. A

polished connection is shown in Fig. 100. Using a combination of optical sandpapers the surface was polished to a uniformity of approximately 3 microns. The router will be connected to the SiPMs using a screw tightened connection. The entrance to the router will be lightproofed using rubber cowl and opaque sealant.

The entire active area of the hodoscope (delimited by the extent of the supporting board shown in Fig. 99 and including the connector block) will be enclosed in a lightproof enclosure. The optical fibres inside this enclosure will be unsheathed so care will be taken to test the integrity of the lightproofing. The surface of this area will be formed from lightproof Tedlar material. The supporting structure for the Tedlar will be formed from a series of hexagonal plastic spacers (5.5 mm) wide and 22 or 15 mm tall depending on the hodoscope layer. The hexagonal spacers will have a male threaded section at the bottom end to attach them to the hodoscope support board. Because of the differences between the outer contour of the scintillators and that of the supporting board there are positions to locate the spacers every approximately 20 degrees around the edge of the hodoscope. These will support a 1 mm thick flexible plastic strip which will trace the outer contour of the hodoscope and will be screwed or glued to the spacer supports. This will create an outer edge at the appropriate height to attach the tedlar without putting pressure on the optical fibres. The Tedlar will be glued to the edge of the strip and also fixed using plastic screws which will attach to the upper threaded portion of the spacers. For transporting the hodoscope a further rigid box will also be manufactured to protect the optical fibres.

### 3.1.4 Resistance of hodoscope and read-out to radiation

The hodoscope tiles and fibres will be exposed to maximum dose of 3.8 rad per hour. This

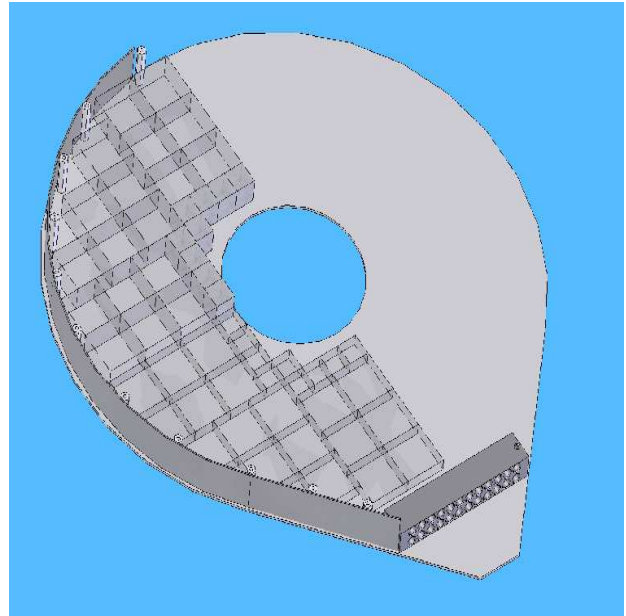


Figure 99: upper: CAD drawing of the hodoscope showing the location of the hexagonal plastic supports for the lightproofing structure and the plastic light proofing strip on the contour of the detector.

was obtained from a GEMC calculation of the forward tagger within CLAS12 with realistic beam and target parameters and without the shielding effects of the Moeller cone. The simulations are discussed in more detail in section 2.7.8.

The resistance of plastic scintillator and the wave length shifting fibres to radiation is well documented. A 116 krad dose (equivalent to 3.5 years of continuous running at CLAS12) will cause loss of 20% of light in wavelength shifting fibre [41]. For plastic scintillator a 20% reduction in light output occurs only after 10 Mrad [42]. Both scintillators and fibres also show natural annealing processes. At 0.64 krad per hour the annealing process can effectively compensate for the radiation damage [43].

A potential loss of 20% of the scintillation light over the operational lifetime of the detector has been accounted for in the design. Even with such losses the hodoscope will operate satisfactorily and achieve the de-

sign aims.

The SiPMs are known to be sensitive to neutron damage which increases the dark count rate. This is a problem when using the devices in single photon counting applications. In the hodoscope the threshold for detection will be equivalent to 3-4 photoelectrons and so these effects are less critical. However the location of the SiPM away from the hodoscope ensures the damage over the lifetime of the device will not be an issue.

Tests of the resistance of SiPMs to neutrons has been carried out at Belle and for the Glue-X experiment. GEMC simulations of the forward tagger indicate that during operation at full luminosity the neutron flux is  $400 \text{ neutrons cm}^{-2}\text{s}^{-1}$  at 1 metre distance from the calorimeter. At 5 m neglecting the effect of shielding and taking a  $\frac{1}{r^2}$  fall off in flux would give  $16 \text{ neutrons cm}^{-2}\text{s}^{-1}$  corresponding to  $0.5 \times 10^9 \text{ neutrons cm}^{-2}\text{year}^{-1}$  of constant running. Noticeable increases in the dark single photoelectron count rate of the SiPMs was only obtained after an integrated dose of  $3 \times 10^9 \text{ neutrons cm}^{-2}$ , which would correspond to 6 years of constant running.

### 3.2 Data Acquisition

This section will discuss the readout systems for the FT-Hodo SiPM including the amplifier design and the flash ADC to be used to store the charge of the signals and extract the timing of the signals.

#### 3.2.1 Front End and Readout electronics

**Analog amplifier for SiPM** The analogue signal from the SiPM will be fed directly to a custom designed pre-amp board. These boards have been designed by the INFN-Genova electronic group, starting from the existing CLAS-IC amplifier [24].

The boards will host 8 independent channels, each coupled to a SiPM, and will be mounted in pairs in the slots of a custom crate, mechanically compatible with the VME

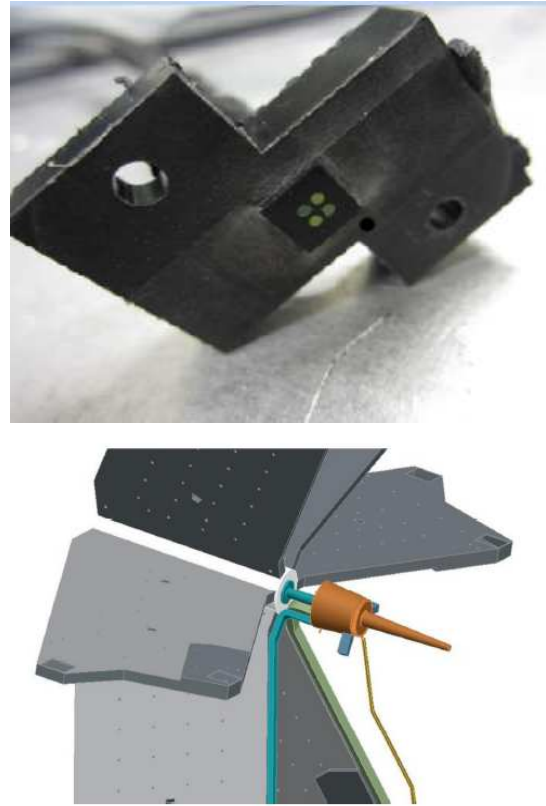


Figure 100: upper: An example of a glued and polished optical fibre connector used in the beam test at Frascati. lower: The forward tagger within CLAS12 showing the route of the optical fibres below the detector.

standard. The 16 SiPMs connected to each pair of boards will be mounted on a mezzanine PCB. This mezzanine will distribute the bias HV to the detectors SiPM and collect their signals for the amplifiers inputs. Fig. 102 shows a prototype of a SiPM amplifier board connected to a prototype of SiPM mezzanine, respectively.

Tests have been done to confirm that the presence of the mezzanine, as well as of the connector between the mezzanine and the board, doesn't introduce any further noise contribution.

The schematic of one channel of the SiPM amplifier board, excluding the HV bias network, is shown in Fig. 103.

Mezzanine / fiber holder

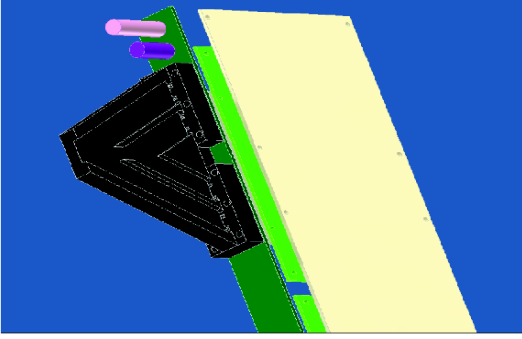


Figure 101: CAD drawing of the connector between the bundle sheaths and the SiPMs. The upper portion of the connector has been removed to illustrate the internal structure of the connector

The first stage is based on a BJT NPN transistor in a common-base configuration, while the second is based on an operational amplifier in a non-inverting configuration. The two BRF92 have been chosen since they are low noise bipolar transistors (the noise figure  $F$  is 2.4dB for  $I_c = 2 \text{ mA}$  at 500 MHz), with a high cut-off frequency and good stability. The gain of the transistor stage is calculated considering that a current pulse at the input corresponds to a variation in the emitter current  $i_e$ . The variation in the collector current  $i_c$  is the same, so the voltage signal at the collector is given by:  $v_c = i_e \cdot R_c$ . The current-to-voltage gain of the first stage is given by the collector resistance,  $G_1 = R_c = 3.9k\Omega$ . The second transistor is used to decouple between the first stage and the second one.

The second stage is composed by an OPA694 operational amplifier in a non-inverting configuration: its gain is given by  $G_2 = 1 + \frac{R_f}{R} = 6.4$ . This stage is coupled to the first one through a 100 nF capacitor to remove the DC component of the signal coming from the second transistor.

The amplifier is coupled to the output connector through a 100 nF capacitor and a 50  $\Omega$  resistor to remove any DC component from

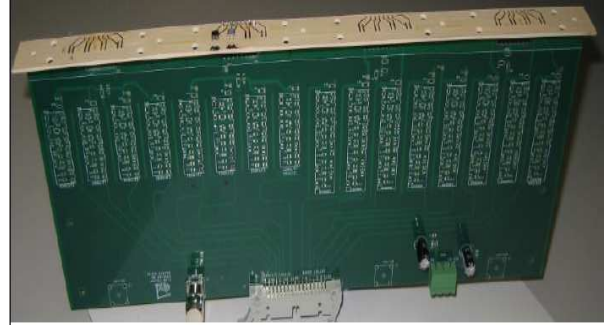


Figure 102: A prototype of the SiPM amplifier board connected to a prototype of the SiPM mezzanine. Two SiPM are actually mounted on the mezzanine. Only the 8 channels on the left part of the board are actually used.

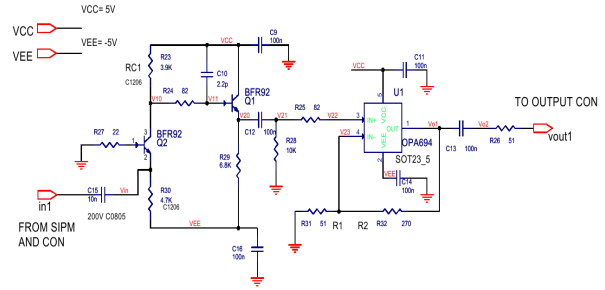


Figure 103: Schematic of a single channel of the amplifier board for SiPM.

the last stage and match the impedance of the output cable.

The overall current-to-voltage gain of the transimpedance amplifier is given by the product of the gains of the two stages:  $G = G_1 \cdot G_2 = 23.7k\Omega$ . The charge gain (i.e. the ratio between the charge delivered by the input current pulse and the charge measured by a charge integrating device fed with the amplifier output signal) is given by  $G_c = \frac{G}{Z_{in}}$ , where  $Z_{in}$  is the input impedance of the charge-integrating device. For  $Z_{in} = 50\Omega$ ,  $G_c \simeq 470$ .

The board has been tested with the same laser system already described in 2.2.2. Fig. 104 shows the results of a measurement done lighting the sensor (SiPM Hamamatsu S10931-100, with active surface 3 mm<sup>2</sup> and pixel size

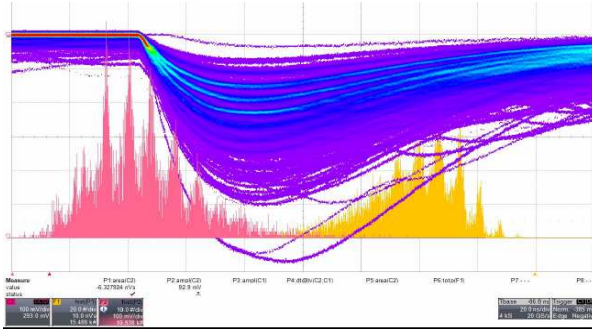


Figure 104: Results of the test of a prototype of the SiPM amplifier board. The vertical scale on the scope is 100 mV/division.

100  $\mu\text{m}$ ) with a low-intensity, 10  $\mu\text{s}$  pulsed laser beam.

The output signal from the board has been sent directly to a digital oscilloscope (LeCroy model “WaveRunner 6 Zi”), and a sync signal from the laser driver was used as trigger. The output signal was integrated within a 70 ns time window. The yellow histogram in fig. 104 shows the distribution of the measured charge, while the pink one shows the distribution of the measured amplitude of each pulse. The digitized waveforms of the pulses are also shown (in persistence mode).

Single photoelectrons peaks are clearly visible, both in the 2 distributions as well as in the waveform.

**Readout electronics** After amplification, the signal has to be acquired through a proper DAQ system and processed in order to extract the relevant physical information, that is the *time* of the interaction (to perform coincidence with the FT-Cal). Also, the *number of photoelectrons* is a quantity that can be measured for each event and could help during the analysis.

The DAQ system for the FT-Hodo is similar to the FT-Cal one, and shares some components with it: for the detailed description of such system, see 2.3.3. Here only a brief summary is reported.

The signal from each SiPM, after been

amplified, is continuously digitized by a fast flash-ADC and, if a trigger condition is satisfied, samples are stored for further analysis. TDCs multi-hit are still present in the system.

### 3.2.2 Slow controls

The slow controls system of the FT-Hodo will be the same of the FT-Cal, and will be integrated with it inside the overall CLAS12 system: see 2.4 for a full description.

The same low-voltage system of the FT-Cal (Wiener “MPOD Universal Universal Multichannel Low - Voltage System”) will be employed for the FT-Hodo.

**SiPM bias system** The 29 channels of high voltage for the SiPM Will be provided by a new CAEN SY5527 supply or exploit existing hv infrastructure from similar devices made available in the decommissioning of CLAS. The SiPM will operate in the range 70 -75 volts. The HV mainframe will be populated by 3 sensing HV supply boards (CAEN A1510) each having 12 channels. The SiPMs will be grouped and mounted on common electronic readout boards according to their gain. The gain matching process will exploit a pulsed laser supply. Possibilities to purchase pre gain matched SiPM will be discussed with the manufacturers when purchasing the modules.

## 3.3 Simulations

To optimise the design of the FT-Hodo, two separate GEANT4 based simulations have been developed at Edinburgh. This section describes the most important results from these simulation studies which guided the design of the detector. The first simulation models a single detector element and tracks the optical photons produced in the scintillation process through the scintillator tile and WLS fibre to the SiPM photodetector. This was used to calculate the expected scintillation photon statistics for different detector designs and to

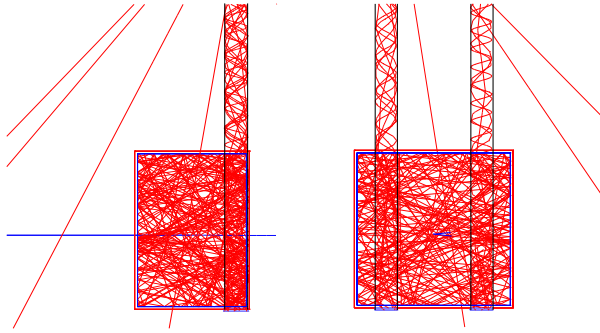


Figure 105: Example of light tracking simulation with 2 WLS. The red lines show the tracks of optical photons, the blue line the incident electron. The black lines show the boundaries of the WLS. The amount of scintillation photons has been reduced by a factor 100 for clarity.

explore the effects of different geometries and light transport systems. The second simulation uses a full reconstruction of the FT-Hodo and FT-Cal to investigate their coupled performance and to establish the capability of the different FT-Hodo designs for electron identification.

### 3.3.1 Optical Photon Tracking in single Element

The detector elements in the simulation used realistic experimental parameters comprising a single plastic scintillator tile wrapped with a reflective coating (reflectivity=85%). For the simulation multiple square grooves were made along the face of the scintillator. The diagonal grooved holes for the final design would be expected to have slightly higher light output. A WLSF is embedded in each groove and surrounded by optical grease (refractive index=1.46). The fibre was multicladd consisting of a core of polystyrene surrounded by an inner layer of PMMA and an outer layer of Fluor-acrylic, both with thicknesses 3% of the fibre radius. The respective refractive indices were 1.6, 1.49 and 1.42. This is consistent with Kuraray-K11 fibre.

The standard GEANT4 physics processes for high energy particles and optical photons

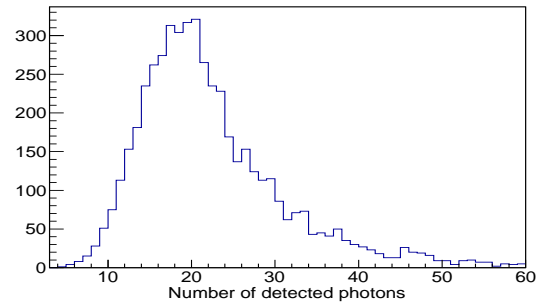


Figure 106: Number of photons detected for tile geometry similar to the previous CLAS Inner Calorimeter, which measured 18 photons per MIP.

were utilised in the simulation. The materials were given realistic photon absorption and emission properties. A visualisation of this simulation is shown in Fig. 105.

To check the simulation a comparison of the results with experimental data from a previous detector design was used, the previous CLAS Inner Calorimeter hodoscope [27]. This consisted a 38 x 38 mm tile with one straight fibre, diameter 1 mm, decay time 7 ns, coupled to a SiPM with a quantum efficiency of 50%. A minimum ionising electron was then tracked through the tile and the optical photons tracked to the photon detector. The previous detector reported 18 photoelectrons and this is in good agreement with the distribution from the simulation, Fig. 106, where the most likely value is around 19. The timing resolution of this design is estimated to be 0.9 ns from recording the time of the first photon in the photodetector.

The simulation was then used to explore possible designs for FT-Hodo. The simulation was used to obtain the number of photons, detected at the SiPM, for different configurations of tile. The area of the tile, the thickness of tile and the number of embedded fibres was varied. A number of configurations for embedded fibres with 1 mm diameter have been simulated as well as a single 2 mm configuration. A quantum efficiency of 50%

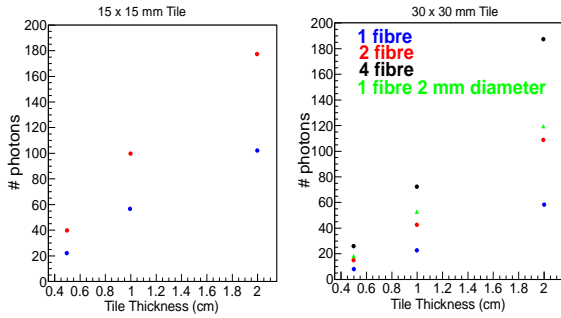


Figure 107: The number of photons detected for different configurations of tile. left-hand plot, 15 x 15 mm; right-hand plot 30 x 30 mm. The x axis is the thickness of the tile and the different colours of points refer to different numbers of embedded straight fibres.

for the SiPM is assumed in the simulation. Fig. 107 shows the dependence of the number of photons detected for different thickness of scintillator tile. The left hand plot is for a 15 x 15 mm (P15) tile and the right a 30 x 30 mm (P30) tile. On each plot the results for 1, 2 and 4 (only 30 x 30 mm case) embedded fibres is shown. In almost all cases the efficiency, defined as the percentage of events with greater than 5 photons detected, was greater than 99.9%. The exceptions to this was for 1 fibre and 2 fibres in a 5 mm thick P30 tile, which were 84% and 99% efficient respectively.

The simulation illustrates important effects when considering the design. Doubling the tile width (15 to 30 mm), or halving its thickness produces a drop in the number of detected photons by more than a factor of 2. While doubling the number of fibres gives less than a factor of 2 increase in the number of detected photons. A 1 cm thick scintillator P15 tile, with two fibres, gave 100 photons and a P30 tile with 4 fibres 80 photons.

The effect of a bend in the fibre was tested in the simulation to be able to quantify the light loss which could be introduced when routing the fibre to the SiPM. The bend radius versus the number of photons relative

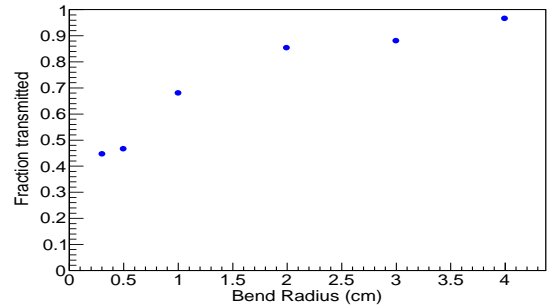


Figure 108: Effect of bending the fibre. Shown is the fraction of photons transmitted to the photon detector as a function of a bend radius in the fibre.

to an unbent fibre is shown in fig. 108. For a bend radius of 3 cm, 90% of photons are transmitted. In addition, previous systems have shown a 3-4 cm bend radius will not significantly damage the fibres [42].

The results for the timing resolution are shown in fig. 109 with a similar layout. The main factor in improving the timing resolution is increasing the number of detected photons, although simulations also showed using Bicron fibres with shorter decay times (3.5 ns compared to 7.1 ns) could improve the resolution by up to 20%. Achieving sub nanosecond timing resolution was possible for most configurations employed in the simulation. For the 1 cm thick, 2 fibre P15 tile and 4 fibre P30 an intrinsic resolution of 0.4 ns is determined. Increasing the thickness to 2 cm improves the resolution to 0.3 ns which is comparable to the SiPM timing resolution. Convoluting the WLS/SiPM resolutions give an overall resolution of 0.5 or 0.4 ns for the 1 and 2 cm thick tiles respectively.

The expected results for the 7 mm and 15 mm thick tiles used in the final design of FT-Hodo were obtained by interpolating the simulated data. Timing resolutions in the range of  $\sim 0.5$  to  $\sim 0.75$  ns are expected from the different detector elements of FT-Hodo and the MIP detection efficiency is expected to be better than 99.9%.

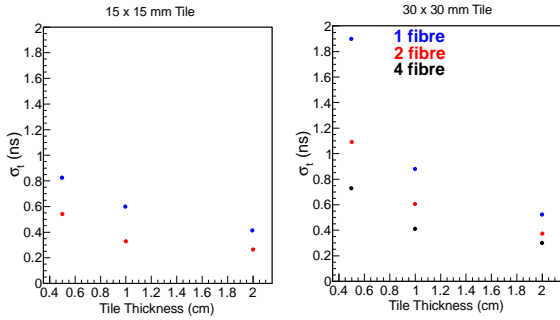


Figure 109: The timing resolution for different configurations of tile. The layout is as for fig. 107.

### 3.3.2 Combined simulation of Hodoscope array and FT-Cal

The second simulation investigated the dual operation of the FT-Cal and FT-Hodo, the main goal being to obtain a quantitative assessment of the number of incident photons which would be misidentified as electrons in realistic operation of the hodoscope. The simulation includes the full geometry of the calorimeter and several configurations of hodoscope with 1 or 2 layers, P15 or P30 pixels and various thicknesses. In the simulation electron and photon events were distributed over the complete face of the calorimeter.

The hits in the calorimeter had energies reconstructed by summing neighbouring crystals, with the hit position calculated from a square root energy weighted mean. It was found that energies were correctly reconstructed for electron angles of 2.5 to 4.6° and events were restricted to this angular range. Hodoscope elements which fired in timing coincidence with the reconstructed calorimeter cluster were analysed. Fig. 110 shows some typical characteristics of the hodoscope events. The top right plot shows the energy deposited by electron and photon events in a 10 mm thick scintillator tile. For an electron the mean is just under 2 MeV, whereas the vast majority of photons hits are below 1 MeV. The top right plot shows the transverse distance (TD), from the calorimeter cluster to the hit hodoscope element for electrons with

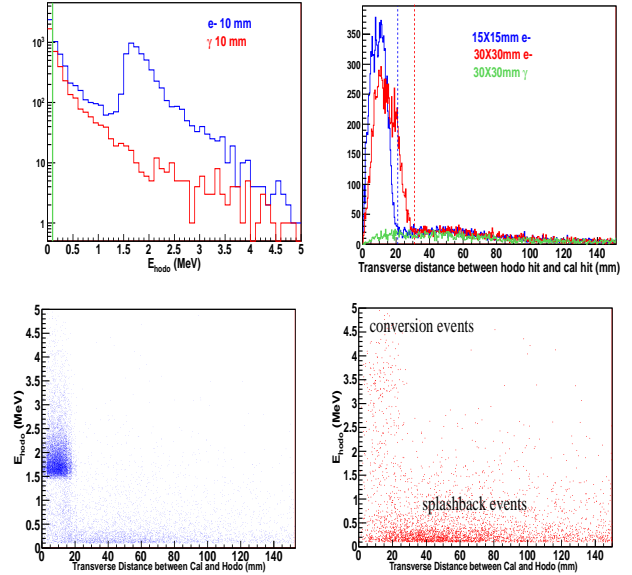


Figure 110: Characteristics of hodoscope in coincidence with FT-Cal. Top-left, energy deposit in hodoscope, Top right transverse distance between calorimeter cluster and hit hodoscope element. Bottom-left, these two variables in 2D for electrons and photons (right).

pixel size 15 and 30 mm and photons with 30 mm. The electron coincidences are contained within a TD cut of 21 and 31 mm for P15 and P30 respectively. The bottom plots show the energy in the veto versus TD for electrons (left) and photons (right). Good electron coincidences cluster around 2 MeV and less than 20 mm as already observed. Other hits with lower energy and larger TD arise from electromagnetic shower splashback from the calorimeter. Such splashback events dominate the photon plot, which also has a significant contribution from events converting in the scintillator characterised by high energy and small TD, as for electron events. As the conversion events contain 2 minimum ionising particles the energy can be up to twice as large as for single electrons.

These simulations were analysed to compare the degree of photon misidentification for different configurations of hodoscope. The results are shown in Fig. 111. For the most

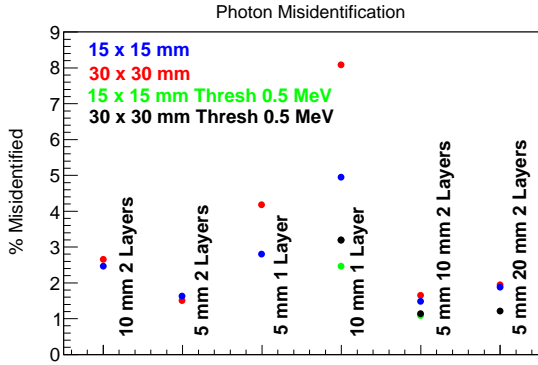


Figure 111: Misidentification of photons for the different configurations of hodoscope detailed on the plot.

basic configuration, P30, 10 mm thick with 1 layer, the misidentification can be as poor as 8% if no threshold is applied to the veto signal. The main contribution to this is splashback from the calorimeter as seen in Fig. 110, bottom-right plot. Applying a threshold of 0.5 MeV reduces the misidentification considerably to 3%. Using smaller hodoscope pixels also has a significant effect on the misidentification as it allow a smaller TD cut eliminating more splashback events. The best method of cutting splashback is to use a coincidence between 2 layers, which reduces the overall misidentification to under 3%. When using 2 layers the main cause of misidentification is photon conversion in the first layer. It can be seen that reducing the size of the first layer to 5 mm almost halves the misidentification while increasing the thickness of the second layer has little effect.

The results of these simulations indicate that to minimise photon misidentification 2 layers of hodoscope should be used, with the first layer as thin as possible to minimise the contribution of photon conversion events leaving a signal in both layers. With a thin first layer the second layer can then be made thicker to optimise other parameters like timing resolution. When two layers are employed the size of the pixels do not have a large effect

on the misidentification as this only reduces splashback.

The general properties expected from different hodoscope designs are outlined in Table 3.3.2.

### 3.4 Frascati Beam tests

A beamtest of a mini hodoscope setup has been carried out at the beam tests facility in Frascati. The setup of the tests are as described for the calorimeter. The setup comprised 8 detector tiles with a readout chain very close to that proposed for the final detector. There were 2 P30 and 2 P15 detectors per layer. Each element was coupled to Kuraray K-11 wavelength shifting fibres which were readout by 100 micron 3x3 Hamamatsu SiPMs coupled to a prototype of the planned readout electronics. An example of a sample pulse shape is shown in Fig. 112. The result of fitting many events and plotting the pulse area as a histogram is also shown in the figure for a 15 mm thick P30 tile. Clear single and double photoelectron peaks can be resolved in the spectrum and the Landau produced by the minimum ionising electrons in the beam can be clearly resolved. The Landau is well removed from the noise. The tests showed excellent agreement between the predicted number of photoelectrons from a thin scintillator with 4 WLS fibres and the Geant4 simulations confirming the suitability of the detector and light readout for the purpose. A minimum ionising peak at twenty five photoelectrons is visible from a 4 mm thick EJ204 tile with 4 WLS fibres.

There were quality control problems with the recent batch of thicker scintillator tiles used in the test. Although the MIP peak was at 60 photoelectrons for a 15 mm P30 this is a factor of  $\sim 2-3$  less than predicted by the simulation. Samples of P30 tiles made from old NE102a scintillator available at Edinburgh gave a factor 2 more light than the new scintillator in the tests. It is assumed

	1 layer P30	2 Layer P30	1 Layer P15	2 Layer P15
SiPM hits per MIP	72	26/185	100	40/175
Time resolution (ns)	0.5	0.4	0.5	0.4
$\gamma$ misidentification	3%	1.2%	2.5%	1.2%

Table 12: Summary of performance of different hodoscope configurations.

that the scintillator batch had poor light output and further scintillator samples are ordered. These will be tested in benchtests in early 2013.

### 3.5 FTHodo summary

The 2 layer design for FTHodo consisting of a thin 7mm thick front layer and a thicker 15 mm thick layer with fibre readout over 5 metres would deliver a close to 100% efficient charged MIP detector, with a time resolution of  $\sim 0.5$ - $0.7$ ns and a photon misidentification of  $\sim 1.2\%$ . This easily meets the stated design criteria for the device. The costs to construct the detector are outlined in table 3.5. A Gant chart outlining the planned construction schedule is shown in Fig. 113.

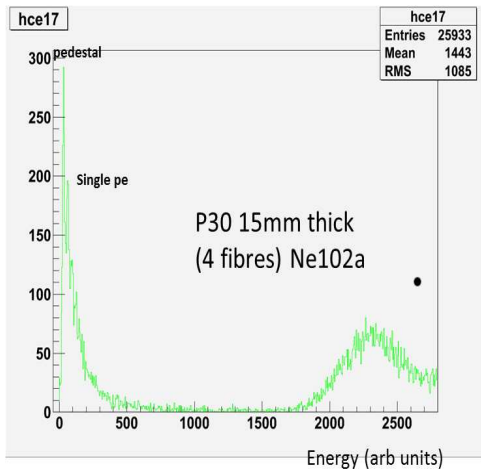
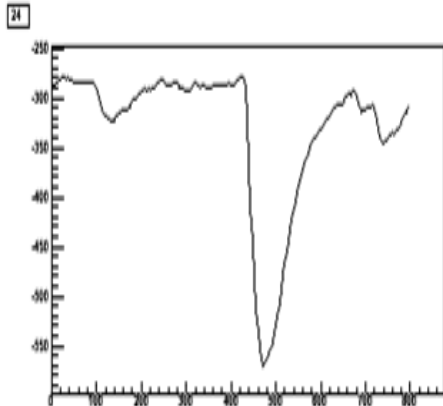


Figure 112: upper: A single detector pulse from a scintillator tile as sampled by the Flash ADC during the Frascati test. lower: The result of fitting the pulse shapes and extracting the pulse area, plotted as a histogram. Single and double photoelectron events can clearly be seen as well as the Landau for minimum ionising particles.

	2 layer design comprising 116 elements per layer
Scintillator cost	31,250
Fibre cost	20,000
SiPM cost	15,250
Flash ADC cost	67,975
Pre-amp cost	7,200
Optical Fibre support structure	1,000
Cables to connect to Flash ADC's, Sheaths	3,000
Light coupling Interface to SiPMs	1,000
Hodoscope mounting boards, lightproofing	500
VME crate to hold hodoscope amplifiers	10000
Slow control	1000
20 channels of HV and LV supply	36000
<b>Total cost</b>	<b>203,175 euros</b>

Table 13: Cost estimate for construction of the hodoscope.

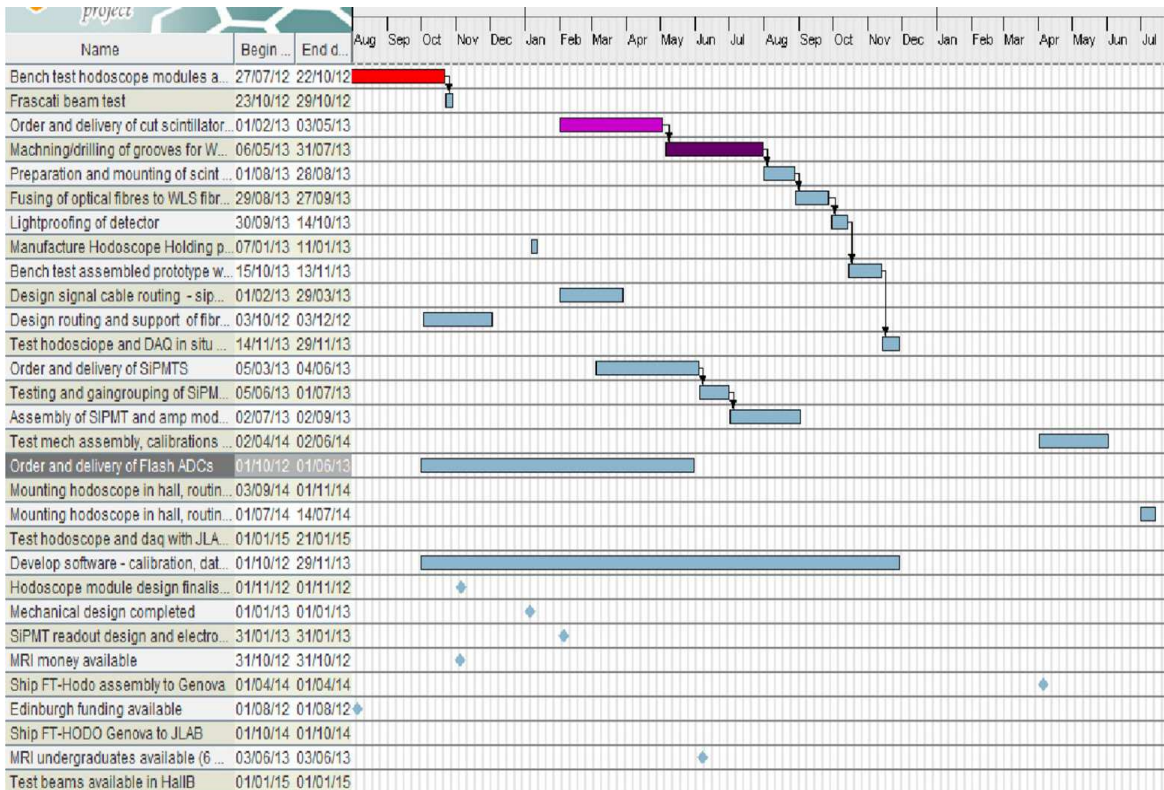


Figure 113: Gantt chart showing the outline construction plan for the hodoscope.

## 4 FT-Trck

### 4.1 Tracker design

#### 4.1.1 Micromegas geometry

Two double layers of Micromegas detectors will be located in the space between the calorimeter and the High Threshold Čerenkov Counter (HTCC). Two layers are indeed a good compromise to achieve an efficient background rejection and track reconstruction with a low material budget. These two layers are each composed of a double faced Micromegas disk bulked on a common PCB. Each side of the PCB displays strips, the downstream ones being perpendicularly oriented to the upstream ones. This particular geometry enables the determination of the (X,Y) coordinates of a track. To limit the number of electronic channels the pitch chosen is  $500\ \mu\text{m}$ , which leads to a resolution better than  $500/\sqrt{12} = 144\ \mu\text{m}$ . The expected drift space will be 5 mm to ensure a good efficiency and the amplification gap will be  $128\ \mu\text{m}$ . To stiffen the mechanical behaviour of the detectors, they will be built on  $600\ \mu\text{m}$  PCB. The two layers will be assembled in a single rigid structure to get a reliable positioning during mounting/dismounting.

The first and second double layers will be located respectively at 1771 mm and 1791 mm downstream of the target, and centered on the beam axis. They will cover polar angles from  $2.5^\circ$  to  $4.5^\circ$ , thus the detectors will be annular-shaped with an active area defined between a 70 mm inner radius and a 142 mm outer radius. The overall inner and outer radii of a disk are 60 and 170 mm respectively. Figure 4.1.1 shows the acceptance in the momentum-polar angle space, but with an internal radius of 80 mm.

The above mentioned double layer design has been implemented in the CLAS12 GEANT4 package, Gemc, as illustrated in Figure 115.

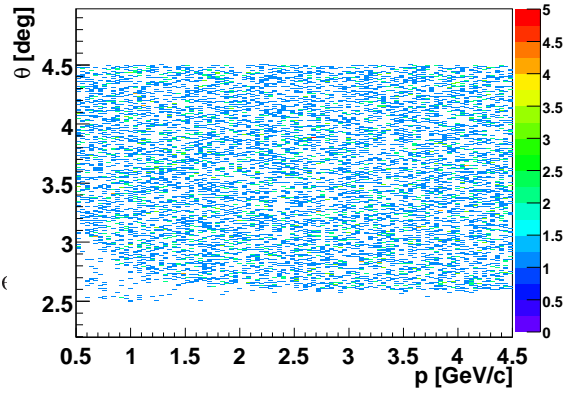


Figure 114: FT-Trck acceptance in the momentum-polar angle space. Electrons were generated without background with  $\theta$  between  $2.5^\circ$  and  $4.5^\circ$  and  $p$  between 0.5 and 4.5 GeV/c. For this simulation, the inner radius of the Micromegas active area was 80 mm.

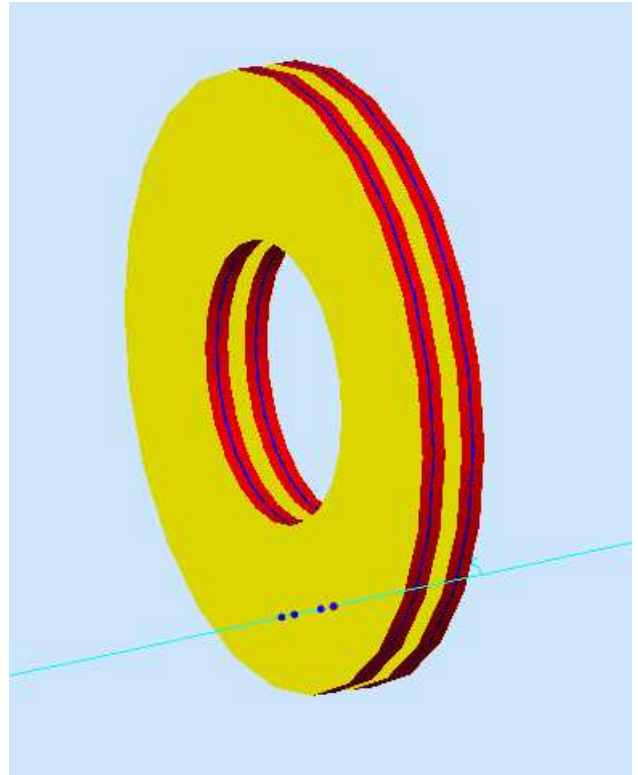


Figure 115: Gemc view of the two double layers of the FT-Trck.

### 4.2 Electronics and DAQ

It is assumed that the FT-Trck readout will follow the scheme adopted for the Micromegas

based central tracker detectors. It will consist of frontend and backend parts. The frontend electronics is responsible for pre-amplification and shaping of the detector signals, for their pipeline buffering during the trigger generation process, for digitization and compression of selected event data and their delivery to the backend electronics. The latter is responsible for the event data concentration and provides an interface with the CLAS12 event building system. The backend electronics also provides a fixed latency path between the CLAS12 trigger system and the FT-Trck frontend electronics. The readout has to be dimensioned for about 4K electronics channels and has to cope with up to 100 kHz channel hit rate (due to the expected physics background of 50 MHz) and with the canonical CLAS12 trigger rate of 20 kHz and latency of 16  $\mu$ s.

#### 4.2.1 Channel count

The FT-Trck consists of 2 stations, each station being composed of a double faced disk with a Micromegas chamber on each face bulked on a common PCB. The strips are oriented perpendicular to the symmetry axis of the stations. In one station the strips of the upstream face are perpendicular to the strips of the downstream face. The outer diameter of the active area of each station is 284 mm. With the strip pitch of 0.5 mm each Micromegas disk will account for 848 channels, each station for 1696 channels and the total amount of FT-Trck channels will be 3392.

Note that for the Micromegas CT (MCT) it is aimed to produce 512-channel FE boards. Obviously with the Disk-shaped Micromegas chambers of 512 strips the best match is achieved between the FT-Trck chambers and the FE electronics. This avoids FE boards which serve several chambers (a potential source of noise) and/or FE boards which are not fully used (the size of the system) and simplifies the interconnection scheme between the chambers and FE boards (improved modularity).

In this case the pitch should be 0.414 mm. The overall channel count will be 4096, as summarized in Table 14. This alternative solution feasible if the geometrical data are set to the present values would be the best choice as spatial resolution would improve.

Pitch	D detector	station	FT-Trck
0.5 mm	848	1696	3392
0.414 mm	1024	2048	4096

Table 14: Channel count.

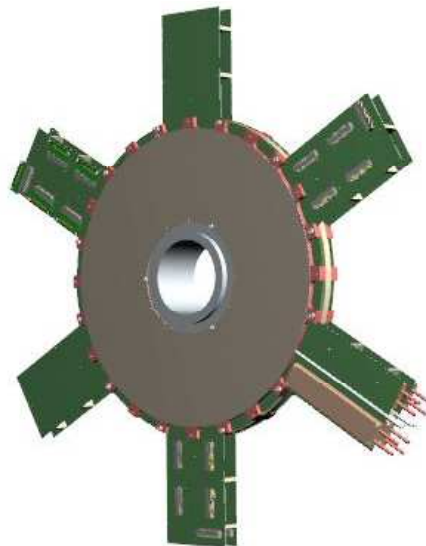


Figure 116: 3D view of the tracker equipped with front-end electronics.

#### 4.2.2 Front-End electronics

Because of the stringent space occupation within the central tracker, the MCT frontend electronics is being designed to be placed off-detector. The micro-coaxial cable assemblies connect the detectors and the FE boards. Non-amplified analog signals transit via the cable assemblies from the chambers to the FE electronics. According to the preliminary studies, for the FT-Trck electronics the length of the cables will not exceed 80 cm.

The 512-channel frontend boards, called FEU (Front-end unit) are housed in 4U crates. The crates are assembled from commercially available standard components. The crates can be designed with the desired number of slots. Two types of crates are foreseen for the MCT electronics: with 2 and 6 slots. The width of the FT-Trck frontend crates will be adapted according to the final channel count and detector - frontend board modularity. Assuming as an example the chambers of 512 channels, 8 FEUs will be needed. These could be housed in 3 3-slot crates that would be located in the shadow of the torus coils. As an example, Fig. 116 displays an example of the double layer design with frontend boards.

#### 4.2.3 Backend electronics

The JLab Hall D Electronics Working Group develops and produces various electronics boards for the Hall D Trigger System. The electronics will be widely used at CLAS12 as well. It is foreseen to adapt some of the developments for the backend electronics of the MCT readout system. The MVT and the FT-Trck systems can share a common backend. Such backend electronics would be housed in a single VXS crate and would consist of a Trigger Interface (TI) module, a Signal Distribution (SD) module, a number of Sub-System Processor (SSP) modules and a crate controller CPU, as shown on Figure 117.

#### 4.2.4 Clock/trigger distribution and data and control flow

The flow of trigger, data and control messages is shown on Figure 117. The TI receives a low jitter system clock and fixed latency trigger signals from the CLAS12 trigger supervisor. It also delivers to the trigger supervisor combined status information (e.g. Busy) of the MCT/FT-Trck read-out system. The physical layer interface is based on a parallel optic technology. The clock and trigger signals are delivered to the SD board over the VXS

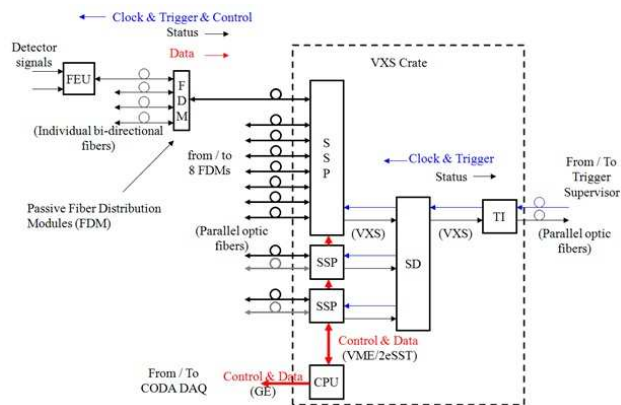


Figure 117: Data and control flow.

backplane. The SD board conveys properly delayed and aligned clock and trigger signals to the SSP boards. It also gathers their status information, combines and sends it to the TI board. These communications happen over the VXS backplane.

Each SSP communicate with up to 32 frontend units (FEU) over bidirectional optical links. Downstream fixed latency communication links will transfer to the frontend units the clock and trigger information (clock will be encoded in data). Over the upstream information the SSP board will receive event data from the FEUs. A single SSP should be enough for the entire FT-Trck readout system. The interconnection between the SSPs and the FEUs will be ensured by a fiber-optic plant consisting of individual fiber-optic cables, parallel fiber-optic cables and fiber distribution modules.

The readout of event data is done by a JLab “standard” crate controller CPU. High rate 2eSST DMA would be needed to retrieve the data from the SSP boards. The data are sent to the CLAS12 DAQ event builder over the Gigabit Ethernet interface of the CPU. The CPU is also used for control and monitoring purposes of the read-out system.

#### 4.2.5 Frontend Units

The main components of the mixed analog-digital FEU boards are eight ASICs, called Dream (Dead-timeless Readout Electronics ASIC for Micromegas), an eight-channel 12-bit 40 MHz ADC and a FPGA device. The 64-channel Dream ASIC performs the collection, the amplification, the filtering, the discrimination and the analogue storage of the detector signal in an analogue memory that is used as a trigger latency and de-randomizing buffer. The sampled signals which have been marked by the trigger are readout asynchronously without stopping the analog storage process allowing a “dead-time free” operation for trigger rates up to 20 kHz and more. Each channel of the Dream chip integrates a charge sensitive preamplifier (CSA), an analogue filter (shaper) and a 512-sample analog memory. Four programmable dynamic ranges (50fC, 100fC, 200fC, 1pC) of the CSA and 16 selectable peaking times of the shaper makes possible the use of the Dream ASIC with a wide variety of Micromegas chambers (i.e. different detector capacitances). The 512-cell deep circular analog memory provides enough buffering to stand the 16 ns trigger latency for a sampling rate of up to 32 MHz.

The Micromegas electronics is being designed to provide both timing and charge information of the detector signals. It is aimed to obtain a timing precision of the order of 15 ns. A 10-bit dynamic range for the frontend electronics will ensure accurate charge measurements with large enough ratios of MIP over threshold (aiming 10), threshold over noise (aiming 6) and maximum charge over MIP (aiming 10).

Detector signals have two distinct components: a fast one from electrons with few ns rising time and a relatively slow one from ions. The ion signal represents about 80-90% of the total charge and lasts for about 100 ns. To avoid ballistic deficit during the charge integration process the peaking time of the Dream shapers will be set to about 100-150 ns. The

shaped signal will have a semi-Gaussian form with about 250-375 ns width. These shaped analog signals will be continuously sampled at 20 MHz. For each trigger, a programmable number of samples of every channel will be sent to an external 12-bit FADC for digitization. The subsequent signal analysis will take place in the FPGA device of the FEUs. After the pedestal subtraction step, a common baseline will be determined for all channels of an ASIC. Next the baseline will be subtracted from all samples. Finally, a programmable threshold will be applied to the obtained result. This zero-suppression technique will minimize the common noise pickup effects. The zero-suppressed data will be collected and sent to the event-builder for subsequent on-line and/or off-line analysis. The trigger readout timing will be adjusted in a way that the digitized samples will correspond to a point on the channel baseline and at least two points on its rising edge. Extraction of signal timing information with the precision less than the sampling period is possible for example by linear interpolation towards the baseline. Charge information can be obtained from the amplitude of the signal or adopting various signal processing algorithms, e.g. FIR digital filter.

#### 4.2.6 FT-Trck data volume

The following have been assumed to estimate the amount of expected FT-Trck data. 512-channel D-shaped Micromegas chambers are considered with the total channel count of 4096 for the entire FT. The physics background rates of 50 MHz have been assumed. In average, the hit multiplicity per track and per layer is about 2 for all detector stations. The trigger rate of 20 kHz has been taken. A zero suppression mechanism with subtraction of a common noise and application of a threshold is assumed. The results are summarized in Figure 118.

The event sizes and the required data

Number of Samples	Background hit rate kHz	Event size Kbyte	Bandwidth Mbyte/s
4	100	1	20
8		3.2	64

Figure 118: Data volume.

throughputs are relatively modest. It looks that a common MCT/FT-Trck backplane is viable. For 4 readout samples their combined data bandwidth would be about 80 MByte/s - far lower than the 200 MByte/s 2eSST DMA throughput achievable in a single VXS crate.

#### 4.2.7 Services

The FT-Trck frontend electronics will need single power supply voltage in the range of 4.5-5 V. Preliminary estimations indicate that the power consumption of the boards will be around 15 W. The FT-Trck frontend crate(s) will be powered from a remote power supply. A good candidate could be a modular low voltage power supply from the Wiener PL508 series. Depending on the number of FT-Trck frontend crates, the power supply should be equipped with one or two 5 V modules. The power supply will be located some 10-12 m away from the frontend crates. A pair of power cables with relatively large cross section (9AWG - 6 mm<sup>2</sup>) and a pair of thin sense cables would be enough to guarantee less than 1 V voltage drop at 30 A current intensity.

Cooling of the boards will be done by compressed air-flow brought to each crate with an 8 mm<sup>2</sup> flexible tubes. The heated air has to be extracted from the vicinity of the detector area. A tube with larger about 50 mm<sup>2</sup> cross-section will be needed per crate.

An interlock system between the cooling infrastructure and the low voltage power sup-

ply must prevent powering the frontend crates when cooling is off. Yet another interlock system is needed to avoid applying high voltages to the Micromegas detectors when the frontend boards are not powered.

### 4.3 High voltage and gas system

#### 4.3.1 High voltage distribution system

Each Micromegas layer will need two high voltage supplies ( $\sim 450$  V for the micro-mesh, and  $\sim 1000$  V for the drift electrode), for a total of 8 cables.

A HV distribution rack will be installed in the Hall, 10 to 15 m away from the detectors. The HV rack will be connected to the detectors with red RG59 cables (or smaller section cable if possible). HV connectors will be located on the edge of the detectors.

#### 4.3.2 Gas system

The gas foreseen for the Micromegas detectors is a mixture of Neon, isobutane (up to 10%) and CF<sub>4</sub> (up to 5%). The use of Neon compared to Argon reduces significantly the discharge probability in the detector, and the CF<sub>4</sub> ensures a good time resolution (around 10-15 ns). The gas mixture may be in the flammable category, which will imply some added work in terms of safety system.

A gas rack with the valves and flow-meters will be installed in the Hall, 10 m away from the detectors, and is likely to be the same used for the Forward Micromegas Tracker. The gas rack will be connected by rigid stainless steel lines to the gas bottles and a mixing unit, situated outside the Hall in the gas shed. From the gas rack one in (diameter 8 mm) and out (diameter 12 mm), rigid first and flexible at the end, stainless steel lines will go up to a distribution panel (100mm x 100mm). From the distribution panel, the gas will be parallelized between the FMT and the FT-Trck in two small, 6mm-diameter plastic lines to the detectors. The equipment to be

delivered should meet US standards in term of maintenance and safety. Therefore Saclay requires an active cooperation in the design validation, component research (US norms), and implantation of the gas system. A JLab safety advisor should be active from the design validation to the installation with ad-hoc gas procedure and security items.

#### 4.4 Expected performance

This section details the reconstruction algorithm which has been developped, as well as the resulting tracking performance of the proposed setup.

##### 4.4.1 Event generation

In order to develop the tracking code and evaluate its performance, electron events have been simulated using Gemc. In a first simulation, single electrons have been generated from the center of the target with momentum between 0.5 and 4.5 GeV/c and polar angles  $\theta$  between 2.5 and 4.5°. This is the first approach to understand which kind of cuts needs to be applied to select good electrons. In a second simulation, events have been generated with background corresponding to the standard CLAS12 luminosity ( $10^{35} \text{ cm}^{-2} \cdot \text{s}^{-1}$ ). Assuming a 100 ns time window for the FT-Trck, around 50,000 beam electrons have to be simulated for a single event. Figure 119 shows the corresponding hit rate per detector. Three to five background hits are expected in average for each detector per event.

##### 4.4.2 Clustering, point association and first cuts

The clustering is the association of strip hits from a single particle. If two or more contiguously strips record a signal, the charge barycenter is computed to determine the position of the particle. Moreover, as an electron is expected to deposit energy in all the

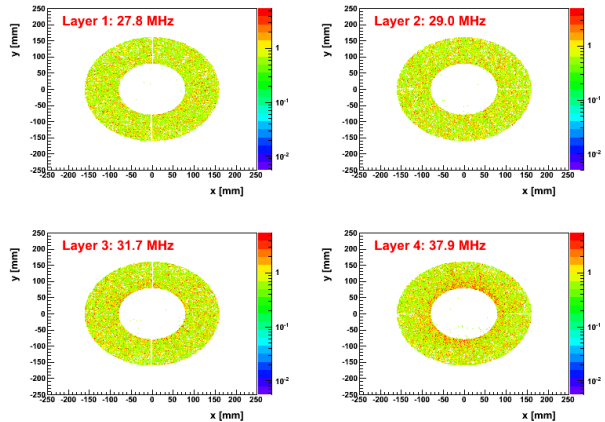


Figure 119: Background rate per detector at the nominal CLAS12 luminosity.

layers, only events with at least one hit in each layer are kept. Then for one double layer, all possible combinations of X and Y are checked and kept only when the corresponding radius is in the active area. The angles  $\phi$  and  $\theta$  of each cluster are then saved, tbeing defined as:

$$\phi = \tan\left(\frac{y}{x}\right) \quad (11)$$

$$\theta = \tan\left(\frac{\sqrt{x^2 + y^2}}{z}\right), \quad (12)$$

where  $z$  is the beam direction and  $x$  (resp.  $y$ ) the horizontal (resp. vertical) axis perpendicular to  $z$ .

At this step we have a  $(\phi, \theta)$  couple for each cluster of each double layer. Track candidates are then built as an association of clusters from the first layer with clusters of the second layer. The aim is to get a good selection of tracks with strong background rejection. First, the cluster radius in the first layer should be smaller than the one in the second layer, otherwise the track candidate cannot come from the target (Fig. 4.4.2 left). Then, for each cluster on the second layer, a  $(\theta, \phi)$  area is defined on the first layer. If a cluster is found in this area, the two clusters are associated in a track candidate (Fig. 4.4.2 right).

Condition	Cut [mm, deg]
Cluster center on the first layer	$68 < R_1 < 162$
Cluster center on the second layer	$68 < R_2 < 162$
difference between the two radii	$-15 < R_1 - R_2 < 6$
difference between the two theta	$ \theta_1 - \theta_2  < 0.6$
difference between the two phi	$ \phi_1 - \phi_2  < 10$

Table 15: Summary table of the cuts for the selection of events with FT-Trck alone.

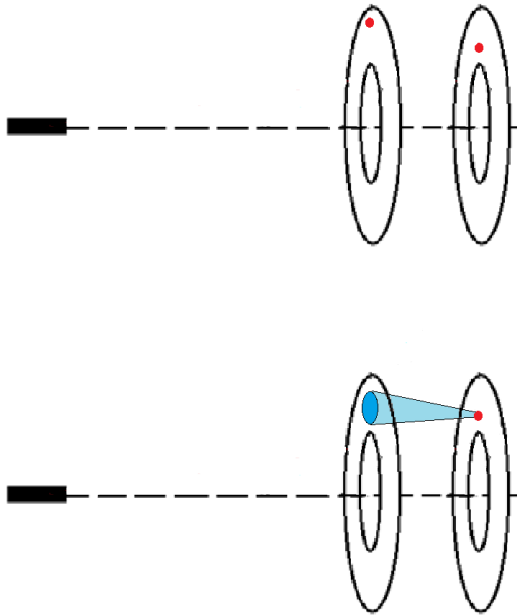


Figure 120: Illustration of FT-Trck cuts. (Left): if the cluster radius  $R_1$  of the first layer is larger than the radius  $R_2$  of the second layer, the track is rejected. (Right): around the cluster of the second layer an area is defined on the first layer. If there is a cluster inside this area, a track candidate is defined.

The Table 15 presents a list of the cuts applied so far.

When a track candidate is defined, a corresponding  $\phi$  angle is kept, and defined as the average of the  $\phi$  angles of the two layers.

For reasons that will appear below, only the  $\theta$  angle of the second layer is kept.

#### 4.4.3 Matching with the calorimeter

The calorimeter is used to obtain the energy of the particle but also for noise rejection. A similar procedure is applied: for a given position obtained in the calorimeter, we check if there is a corresponding track candidate in the FT-Trck. The cuts applied are presented in the Table 16.

When the matching is successful, the algorithm for the backward reconstruction is called.

#### 4.4.4 Backward extrapolation

The aim of the extrapolation is to determine the particle parameters at the vertex position. Using the movement equations of a charged particle in a magnetic field, the track is reconstructed from the second layer of Micromegas to the target. There are two main difficulties for the reconstruction.

The initial angle  $\theta$  calculation using formula 12 assumes that the particle is coming from the center of the target following a straight line. If this indeed leads to a good approximation at moderate momentum, low momentum electrons (below 1 GeV/c) are significantly bended due to the magnetic field. In this case a wrong initial angle is used as shown on Figure 121 where the difference between the  $\theta$  used for the reconstruction and the real

Condition	Cut [mm, deg]
difference between the two radii	$-0.44 * p - 13 < R_2 - R_{calo} < -0.44 * p + 2$
difference between the two theta	$-0.8 < \theta_{calo} - \theta_2 < 0.5$

Table 16: Summary table of the cuts applied for the matching between the FT-Trck and the calorimeter.

one is plotted as a function of the momentum.

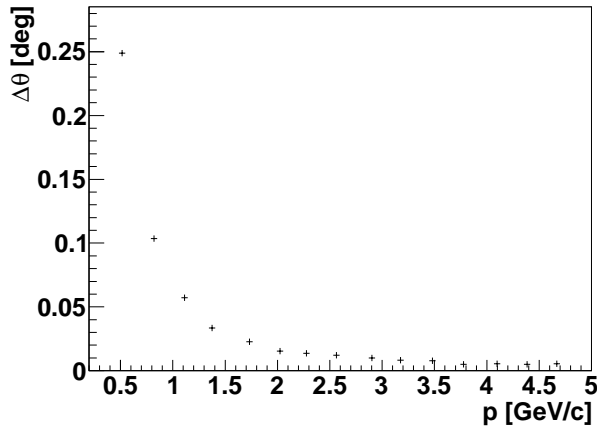


Figure 121: Difference between the  $\theta$  used in the reconstruction and the real one as a function of the momentum. Electrons are emitted from the center of the target with  $\theta = 3^\circ$ .

To avoid this problem the angle calculated from the two clusters of the track could be used but the distance between the two layers makes the  $\theta$  estimation even worse. It has therefore been decided to correct this bias at low momentum by fitting the distribution shown in Figure 121.

The second difficulty concerns the end of the backward reconstruction. It is an important point because if the particle is stopped too far from the point from which it has been emitted, it can drastically change the value of the track parameters. It has been found that the best criteria consists in defining the vertex as the track position with the smallest distance to the beam axis. If the vertex position is located outside the target, the extrapolation is

stopped at  $z = 0$ .

#### 4.4.5 Results

We present here the results using events simulated with background, and electrons generated all along the target. The left (resp. right) part of Figure 122 shows the average resolution for  $\theta$  (resp.  $\phi$ ) by bins of 0.25 GeV/c. The requirements are matched for electrons with momentum above 1 GeV/c. A new version of the calorimeter is available, and yields to a significantly better momentum resolution. This version has not been used in the tracking yet, but should help to meet the requirements at low momentum.

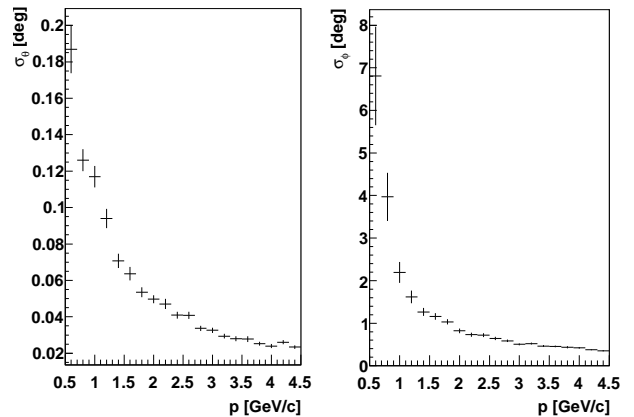


Figure 122: Resolution for  $\theta$  (left) and  $\phi$  (right) as a function of the electron momentum by bins of 0.25 GeV/c.

## 4.5 Costs and planning

### 4.5.1 Electronics

The presented cost estimate assumes the use of 512-channel Disk-shaped Micromegas chambers. The cost breakdown is as follows:

- Frontend units:  $8 + 2 \text{ spares} = 10 \times 2 \text{ k€} = 20 \text{ k€}$ ;
- Signal cables:  $64 + 16 \text{ spares} = 80 \times 150\text{€} = 12 \text{ k€}$ ;
- Backend: 6.2 (if shared with the MCT) or 22 k€(if independent system);
- Frontend-backend connections:  $8+2 \text{ spares} = 10 \times 100\text{€} = 1 \text{ k€}$
- LV Boards - 4 k€(if independent system);

At this phase a good cost estimate for the FT-Trck readout electronics would be 59 k€.

Production of the frontend cards will start in 2013, with prototypes due in January and mass production to begin in October. The backend units should have prototypes ready in February 2013, and after tests production will follow in Fall.

### 4.5.2 Detectors

Three Micromegas double faced disks (2 + 1 spare) plus two prototypes will be built using the bulk technology at Saclay. The total cost, including the PCB manufacture, the test bench and the assembly of the detectors is  $5 \times 5 \text{ k€} = 25 \text{ k€}$ .

The cost of the HV boards is  $2 \times 4.3 \text{ k€} = 8.6 \text{ k€}$ , and one expects 5 k€, for the gas system. The Saclay personnel cost (Labour cost) is 44 k€. Adding various small size equipment (flowmeters, stainless steel tubes, etc..) and the cost for transportation, the cost estimate would be 91 k€.

The general cost including the electronics would then be 150 k€.

The design of the tracker would be ready by

December 2012. A prototype will be delivered in Saclay in April 2013 then tested during Summer. Final or modified design would be ready in October 2013. The final detector should be ready to be tested with final electronics in Summer 2014 and shipped to Genova in September 2014. The three following months will be dedicated to the mounting of the full photon tagger equipment.

## 5 Integration and Installation

### 5.1 Introduction

In this section the structure for the whole Forward Tagger (FT) will be described. The mechanical design of this system has been driven by geometrical constraints by the rest of the detector, geometrical acceptance optimization and performance optimization, taking into account cooling, material budget, front-end electronics location.

The FT detects electrons scattered between  $2.5^\circ$  and  $4.5^\circ$  w.r.t. the beam axis. To allow this acceptance, the FT calorimeter must cover down to  $2^\circ$  and up to  $5^\circ$  with lead tungstate crystals. Since no massive materials are allowed at angles larger than  $5.5^\circ$ , crystals, cooling, mechanical supports and tungsten shielding have been optimized in a very compact design. Outside this  $5.5^\circ$  we will only have insulating material, which has a very low density,  $35 \text{ kg/m}^3$ , and routing for cabling and services in the blind area of the CLAS12 detector, where the toroidal magnet coils are.

As described in this document, the FT is built by several parts that can be grouped as follow:

- the inner tungsten pipe,
- the tungsten cone acting as Moeller electrons shield,
- the tracker,
- the hodoscope,
- the calorimeter,
- the front-end electronics,
- cabling and services.

From the mechanical point of view, the most challenging part is the integration of the calorimeter, due to the weight and fragility of the crystals. Anyhow, due to the need for precision positioning and space constraints, also the relative positioning and alignment of the various sub-detectors will be critical.

### 5.2 Constraints from other sub-detectors

The FT must be installed around the beam line between the Cherenkov Counter and the first layer of Drift Chambers. The Cherenkov Counter will be movable along the beam axis. In operating position, it will extend up to 1730 mm downstream w.r.t. the Interaction Point (IP) this plane defines the upstream border of the allowance for the FT. The first layer of Drift Chambers will be installed in front of the toroidal magnet coils, with an inclination of  $68^\circ$  w.r.t. the beam axis. The front-end electronics boards of the Drift Chambers define the downstream border of the allowance for the FT. The minimum distance of the Drift Chambers boards from the beam axis will be  $\sim 140$  mm at 2280 mm downstream w.r.t. the IP. Taking into account the outside radius of the FT, including insulation, and the inclination of the Drift Chambers, the FT can not exceed  $\sim 2150$  mm w.r.t. the IP.

The FT will need cabling and services routing, for gases and cooling. These services must be connected to the outside of CLAS12. All the routings will be installed in the shadow area of the toroidal magnet coils, i.e. in six slots extending radially from the beam line to the periphery. Each coil will be  $\sim 100$  mm thick, allowing us to host also some front-end electronics, which must be close to the detectors.

All the FT will be attached to the toroidal magnet cryostat. This is needed both for mounting sequence constraints and to avoid massive supports in front of the Drift Chambers. A support pipe with a proper flange will be attached to the magnet cryostat. On the other end, another flange will be bolted to a corresponding flange of the inner tungsten pipe. A proper system to allow precise alignment and positioning of the detector w.r.t. the beam line and the interaction point.

To the inner tungsten pipe all the other systems will be attached. The calorimeter will be kept in position w.r.t. the inner tung-

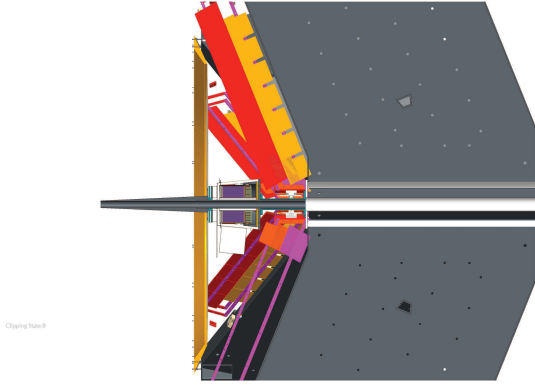


Figure 123: Allowable space for the Forward Tagger: on the left, the Cherenkov counter, on the right the toroidal magnet cryostat and one sector of the Drift Chambers. Two boxes for front-end electronics, placed in the cryostat shadow, are shown as well.

sten pipe via four radial supports, made of PEEK. PEEK has been chosen because of its low thermal conductivity ( $0.25 \text{ W/m}\cdot\text{K}$ ) and its relatively high tensile strength ( $\sim 100 \text{ MPa}$ ). In addition, it features high radiation hardness and excellent stability over a broad range of temperatures [44].

The tungsten cone will be attached to the inner tungsten pipe with a system of flanges and o-rings, to allow evacuation of the beam line if needed. The tungsten cone will end, in downstream direction, with a cylindrical section. On this section, the tracker and the hodoscope will be bolted. These detectors will be placed between 1740 mm and 1795 mm downstream w.r.t. the IP. A view of the allowable space for the FT is shown in Fig. 123.

In the next sections, the mechanical design for each subsystem will be described in detail, followed by the description of the mounting procedure and integration in CLAS12.

### 5.3 FT mounting procedure

The different steps of the FT mounting procedures are shown in Figs. 124 and 125. The FT will be mounted on a cart flipping two times

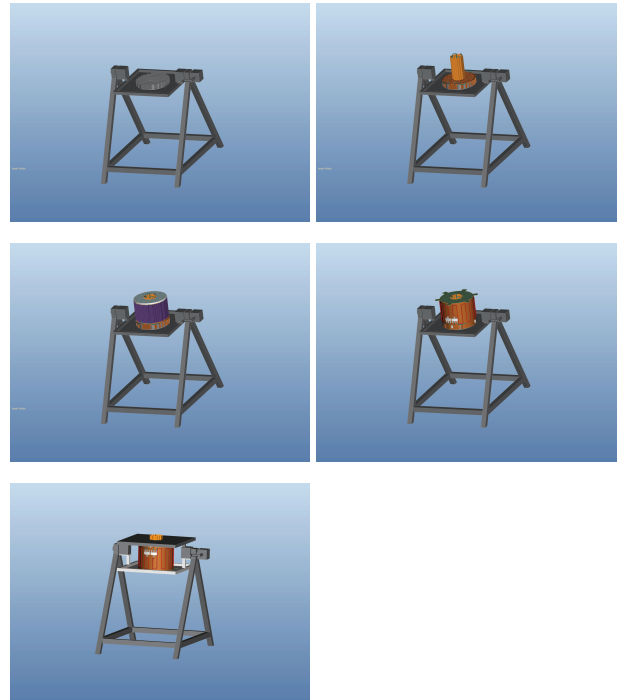


Figure 124: FT mounting procedure, step one. From top-left: assembly of the back copper plate on the support (1), the inner skin and the inner cooling system (2), crystals and front grid (3), the LED system, the external skin and the external cooling system (4), rotating the FT with the front part down-ward looking (5).

the partial assembly to simplify the procedure. At the end the system will be placed with the front part up-ward looking. The FT-Hodo and the FT-Trck, pre-assembled in the lab, will be then inserted around the central pipe.

### 5.4 Installation in CLAS12

The Forward Tagger (FT) will be attached to the torus cryostat. No other attachment points are foreseen. Due to this, the installation procedure will essentially reflect the distance of the various subsystems from the main attachment point.

Since the cables and pipes needed for the FT detectors will be installed together with



Figure 125: FT mounting procedure, step 2. From top-left: the motherboard on the back side (1), the back tungstane hat (2). Flipping again: the front part is now up-ward looking, inserting the inner tungstane pipe (3), completing with the external thermal insulator (4).

the ones of the drift chambers, we will not describe here their installation procedure, but we will assume to have them in position before the beginning of the FT mounting procedure.

The first part that will be installed is the main support pipe. This will be bolted to the torus cryostat flange and properly aligned. The alignment is needed to guarantee the proper and accurate positioning of the inner tungsten pipe, which is the actual reference for the detectors.

The FT calorimeter will not be mounted in on-beam position. We foresee to use *ad hoc* tooling to manage the precise and safe construction of the detector, since the single crystals are very delicate and the whole calorimeter is quite heavy. The inner tungsten pipe and the complete calorimeter with its insulation and case will be installed on operating position as a whole. A proper carrying tool, allowing for moving this element with the overhead crane will be designed and used to put it in position.

The calorimeter will be fixated to the main support pipe via a flange on the inner tungsten pipe. After the bolting, the carrying tool will be removed and the alignment will be verified with lasers and proper check points on the calorimeter itself. Then cables and pipes will be connected and fluids will be circulated to verify the correct functioning of the system.

The Moeller shield will be made of several parts. The first element will be installed on the inner tungsten pipe to allow the mounting of the tracker and of the hodoscope. The front-end electronics boxes for the tracker will be installed on the calorimeter case. The hodoscope read-out and front-end electronics will be installed in their locations as well.

The alignment of the two tracker planes is critical, therefore they will be mounted on a common support frame and precisely aligned before being delivered in Hall B. The hodoscope will be fixated to this support frame as well and aligned. The support frame will feature some precisely machined and adjustable attachment points to be connected and finely aligned to the first element of the Moeller shield.

The hodoscope and the tracker will be installed at this stage, as a single object, taking advantage of the support structure. The optical fibers collecting the light from the scintillator tiles of the hodoscope with their photon sensors already glued will be connected to the read-out electronics. The tracker planes will be connected to their front-end electronics and to the gas pipes. Electronics and gas supply system will be finally tested.

The installation procedure will finish with the fixation of the remaining part of the Moeller shield. A final check of the alignment of the cone will be performed and eventual adjustment of the cone position, via thin metal foils, will be performed.

## 5.5 Cabling and services routing

All services and cables necessary for the operation of the FT detectors will be routed along the torus coils to minimize the interference with the CLAS12 Forward Detector. These include the following items:

- FT-Cal:
  1. signal cables (332 coaxial cables with diameter of 2.5 mm),
  2. HV (3 multiwire cables with diameter of 15 mm) and LV cables (6 cables with diameter of 3 mm)
  3. slow controls (32 wires with diameter or 2 mm),
  4. cooling pipes (2 thermally-insulated pipes with diameter of 35 mm) and gas lines (2 pipes with diameter of 8 mm);
- FT-Hodo:
  1. optical fibers (768 1-mm fibers grouped in 48 bundles for a total diameter of 55 mm);
- FT-Trck:
  1. optical fibers for the transmission of the digitized (8 lines with diameter of 2 mm),
  2. slow controls (3 usb cables),
  3. HV (8 cables) and LV (4 wires for a total diameter of 4 mm) cables,
  4. gas lines (2 pipes with diameter of 8 and 12 mm) and cooling lines (3 inlet tubes with diameter of 3 mm and 3 outlet tubes with section of 500 mm<sup>2</sup>).

Cables and pipes will be grouped and routed along the direction of the magnet coils using appropriate rails. The FT-Cal signals cables and the FT-Trck optical fibers will be routed on the left side of the detector along the coil between sector 1 and 2 of CLAS12, toward the electronic that will be located on the left

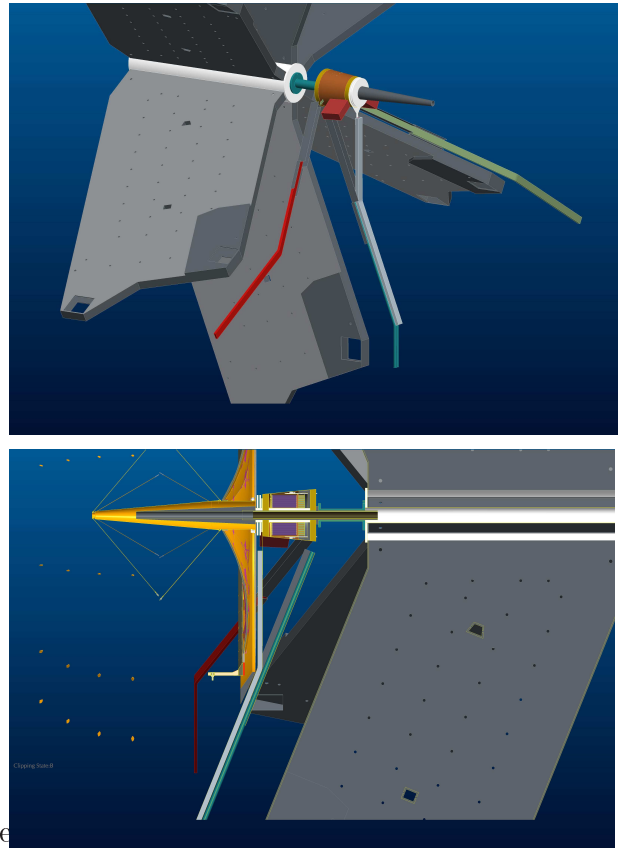


Figure 126: Schematic of the proposed cable and services routing for the FT detectors in 3D view (top) and a section view (bottom).

side of the Space Frame. The FT-Hodo fibers will be routed down toward the crate hosting the preamplifier that will be attached to the torus magnet legs. The HV, LV and slow controls for both Ft-Cal and FT-Trck will be routed on the right side of the detector along the coil between sector 4 and 5 of CLAS12. The gas and cooling lines for both FT-Cal and FT-Hodo will be routed on the left side of the detector along the coil between sector 1 and 6 of CLAS12. These pipes will be extended up to appropriate gas panels, to the air compressor and chiller that will be located on the ground floor of the experimental hall.

The rails width and depth will be chosen compatibly with the space available both

during the normal operation or maintenance of the CLAS12 drift chamber, and with the clearance between the HTCC and the CLAS12 Forward Detector. With the grouping described above the necessary cross section along the 4 outgoing direction is always less than  $4000 \text{ mm}^2$  and therefore compatible with the available space of  $50 \times 80 \text{ mm}^2$ . In addition the rails will be designed to be removable in case of maintenance of the FT. Fig. 126 show a schematic of the proposed routing paths.

## 6 FT Commissioning and Calibration

This section describes the procedures that will be followed during the construction of the FT and its installation in Hall B to ensure the proper functioning of the device, verify alignment and positioning, identify and replace faulty components. A complete series of tests will be performed to insure the proper functioning of the all subsystem composing the FT. In Genova, first checks will be performed during the assembly phase. Besides tests on crystals, light sensors, electronics, and thermal behavior, cosmic ray will also be used. The detector will be moved at JLab and after the installation in CLAS12, the response of the FT to the cosmic rays will be tested to provide: channels gain matching; absolute light output, time synchronization with respect to CLAS12 (trigger), absolute time measurement, coincidence timing between FT-Hodo elements and relative FT-Hodo/FT-Cal timing. Once the beam will be available in the Hall, we will make use of known reactions to commissioning the detector. The elastic electron scattering will be used to measure the FT components alignment and absolute efficiency, the FT-Cal energy and position resolution, the FT-Trck position resolution and the FT-Hodo response to MIPs. The reaction  $p(e, ep\pi^0)$  will be used to measure the FT response to  $\pi^0$  induced em shower, detecting the scattered electron and the proton to test the FT-Hodo veto efficiency, the FT-Cal resolution via  $M_{\pi^0}$  reconstruction, and to measure background in FT-Trck.

As for the other CLAS12 subsystems, the commissioning plan is divided in three steps: quality assurance and sistem checks, system checkout, commissioning and calibration with and without the beam. In the following we describe the different procedures foreseen for each FT component.

### 6.1 Quality assurance and system checks

For the FT-Cal and the FT-Hodo we report in details the quality insurance procedures. For the FT-Trck we refer to the Central MicroMegas commissioning plan since the FT-Trck shares the same technology.

#### 6.1.1 FT-Cal, PBWO Crystals

TEST # FT-Cal PbWO-II crystals	
PbWO crystals	Measure the physical/optical properties (size, light yield, decay time, light transmission, radiation hardness, ...)
Special equipment	The tests will be performed at the ACCOS facility at CERN
DAQ Configuration and Trigger	The facility has all the necessary electronics/daq/trigger
Manpower and time needed	The ACCOS facility tests 20 crystals at time, 100/day therefore we expect to operate the machine for 1 week, 2 people
Software for analysis of results	ACCOS produces automatically the results
Computing resources	No need of computer resources
Information to be saved in the database	Some information will be saved in the DB: size, LY, light transmission, radiation hardness, decay time

#### 6.1.2 FT-Cal, APD

TEST # FT-Cal light sensors	
APD/SiPM	Measure the properties of the light sensors at fixed T (visual inspection, gain%V, linearity, dark current, dead areas ...)
Special equipment	The tests will be performed in Genova using laser and LED sources
DAQ Configuration and Trigger	The daq will be custom, optimize to the necessary tests
Manpower and time needed	3months, 1 person
Software for analysis of results	Custom system
Computing resources	No need of computer resources
Information to be saved in the database	dG/dV, dG/dT, QE, dark current

#### 6.1.3 FT-Cal, Front-End electronics

TEST # FT-Cal FE electronics	
Preamplifiers	Measure the properties of preamplifiers for APD/SiPM readout: gain, output signal shape for reference pulse, noise and motherboard
Special equipment	The tests will be performed in Genova/Orsay using local test bench
DAQ Configuration and Trigger	NA
Manpower and time needed	1month, 1 person
Software for analysis of results	NA
Computing resources	NA
Information to be saved in the database	Gain, Trise, Tfall, noise RMS

#### 6.1.4 FT-Cal, cooling system

TEST # FT-Cal cooling system

Thermal shield, FT-Cal vessel, chiller and pipes	Test of cooling system including pipe and vessel tightness, T uniformity, cooling power
Special equipment	The tests will be performed in Genova using local test bench
DAQ Configuration and Trigger	NA
Manpower and time needed	2 weeks, 1 person
Software for analysis of results	NA
Computing resources	NA
Information to be saved in the database	Temperatures should be store during data tacking

### 6.1.5 FT-Cal, Read-Out Electronics

TEST # FT-Cal RO electronics	
fADC, splitters, discriminator, TDC	Test of the whole RO chain from the preamp to the stored data: proper functioning of each board and each channel: ADC conversion factor, charge linearity, TDC conversion factor and linearity, Discriminator minimum threshold
Special equipment	The tests will be performed at JLab/Genova using the local electronic test benches
DAQ Configuration and Trigger	?
Manpower and time needed	?
Software for analysis of results	NA
Computing resources	NA
Information to be saved in the database	ADC conversion function, TDC conversion function, Discriminator minimum threshold

### 6.1.6 FT-Cal, Slow controls

TEST # FT-Cal Slow controls	
HV for light sensors bias and LV for preamps, motherboards	Test of the functionality of crates and boards and power/signals distribution
Special equipment	The tests will be performed in Genova using the local electronic test benches
DAQ Configuration and Trigger	NA
Manpower and time needed	1 week 1person
Software for analysis of results	HV and LV monitoring system
Computing resources	NA
Information to be saved in the database	LV, dead channels

### 6.1.7 FT-Cal, LED monitoring system

TEST # FT-Cal monitoring	
LED system to monitor gain matching, linearity, light transmission	Test of the functionality of the system, individual LED calibration, light output
Special equipment	The tests will be performed in Genova using the local electronic test benches
DAQ Configuration and Trigger	NA
Manpower and time needed	1 week 1person
Software for analysis of results	Dedicated software to control the system and analyze the results that will be integrated in standard CLAS12 DAQ
Computing resources	NA
Information to be saved in the database	Individual LED light output

### 6.1.8 FT-Cal, Cables

TEST # FT-Cal cables	
HV, LV, signal cables	Test of the functionality of all connection cables
Special equipment	The tests will be performed in Genova using the local electronic test benches
DAQ Configuration and Trigger	NA
Manpower and time needed	1 week 1person
Software for analysis of results	NV
Computing resources	NA
Information to be saved in the database	NA

### 6.1.9 FT-Hodo, Prototyping

TEST # FT-Hodo-Prototyping	
	Geant 4 simulation of various designs of detector elements Each element comprising plastic scintillator tiles with wavelength shifting fibres embedded in surface of scintillator tile. Simulate the various detector element designs comprising different tile sizes/shapes and coiled/linear wavelength shifting fibre. Simulations will include modeling of propagation and capture of scintillation photons. Compare predicted yield of scintillation photons for various configurations and different techniques to embed the fibre. Couple to simulation of forward tagger with realistic beam parameters to assess the contribution from splashback
Geant4 simulation of detector elements Construct prototype detector elements to be used in hodoscope. Characterise test modules Test with SiPMTs	Construct 2-3 prototype detector elements. Initial tests will use standard PMT (Hamamatsu h36140-10) coupled to wavelength shifting fibre.  Assess efficiency of modules for detecting MIPs at various regions on surface of tile, establish timing resolution. Exploiting cosmic and beta source tests. Compare with Geant4 simulation predictions.  Detector modules will likely be coupled to SiPMT in final design for operation in magnetic field of CLAS12. Default design is use same amp and SiPMT as used in current hodoscope. Tests of alternative amp modules and light sensors will be carried out as part of the tests in Genoa.

Special equipment	DAQ system with ADC and TDC readout available in detector labs at Edinburgh. Hamamatsu tubes and additional plastic scintillator modules available for coincidence measurements with sources/cosmics.  Wavelength shifting fibres and scintillator tiles available at Edinburgh. Diamond tipped cutting tool equipment available for manufacturing prototypes.
DAQ Configuration and Trigger	Use Edinburgh DAQ system. Double coincidence between 2 plastic scintillator strips with prototype detector sandwiched between.
Personpower and time needed for prototype development and design	Geant simulations: 1 month, 1 person Manufacture of prototypes: 1 week, 1 person Bench tests of prototypes: 1 month, 1 person Light sensor (SIPMT) and readout tests in Genoa: 1 month, 1 person
Personpower and time for construction of final array	Construction and testing of detector modules: 1 month, 2 person Mounting onto support board: $\frac{1}{2}$ month, 1 person Connecting WLS fibres to light sensors and readout: $\frac{1}{2}$ month, 1 person Testing complete array with cosmics/sources: $\frac{1}{2}$ month, 1 person
Software for analysis of results	Geant4 framework exists. Implementation for tests carried out by Edinburgh RA and student. Results analyzed in ROOT.
Computing resources	No need for computing resources
Information to be saved in the database	NA

### 6.1.10 FT-Trck, Micromegas

A detailed description of MM commissioning is reported in the MM commissioning plan. FT-MM will adopt the same procedures reported there.

### 6.1.11 FT-Cal, Checks

TEST # FT-Cal checkout 1	
Full check of the whole FT Cal subsystem	Test of the full assembled calorimeter: <ul style="list-style-type: none"> <li>• Vacuum tightness</li> <li>• Cooling and T stability</li> <li>• HV check for individual channels, LV check, cabling check</li> <li>• Light transmission and signal output for individual channel using the light monitoring system (presence of signal, linearity tests)</li> <li>• Cross-talk between crystals</li> </ul>
Special equipment	The tests will be performed first in Genova and then repeated before installation in CLAS12
DAQ Configuration and Trigger	DAQ bench test Genova / DAQ bench test JLab
Manpower and time needed	1 week 1person (x2) + space for JLab tests
Software for analysis of results	Local CODA installation
Computing resources	INFN-GE CODA setup for tests in Genova and JLab
Information to be saved in the database	NA

### 6.1.12 FT-Cal, Checks with cosmic rays

TEST # FT-Cal checkout 2 – Cosmic rays	
Full checkout of the FT-Cal using stand-alone cosmic ray setup	Measure the FT-Cal response to cosmic ray for (individually) <ul style="list-style-type: none"> <li>• gain matching</li> <li>• absolute light output</li> <li>• relative timing</li> </ul>
Special equipment	The tests will be performed first in Genova and then repeated before installation in CLAS12
DAQ Configuration and Trigger	DAQ bench test Genova / DAQ bench test JLab
Manpower and time needed	1 week 1person (x2) + space for JLab tests
Software for analysis of results	Local CODA installation + dedicated monitoring tools
Computing resources	INFN-GE CODA setup for tests in Genova and JLab
Information to be saved in the database	NA

## 6.2 System checkout

Here are described the checks that will be performed upon completion of installation to verify the proper functioning of the system.

### 6.2.1 FT-Cal, Checkout with LED system

Checkout of FT-Cal with LED	
Full checkout of the whole FT Cal subsystem installed in Hall-B	Installation of the FT-Cal in CLAS12 Test of the full assembled calorimeter: <ul style="list-style-type: none"> <li>• Vacuum tightness</li> <li>• Cooling and T stability</li> <li>• HV check for individual channels, LV check, cabling check</li> </ul> Light transmission and signal output for individual channel using the light monitoring system (presence of signal, linearity tests)
Manpower and time needed	1 week INFN and Hall-B technicians for installation 1 week checkout INFN researchers 1 week DAQ JLab expert to integrate the FT-Cal in the CLAS12 RO and trigger systems
Software for analysis of results	NA
Computing resources	NA
Dependencies from other systems	CLAS12 DAQ and Trigger
Information to be saved in the database	Translation tables

### 6.2.2 FT-Hodo, Checkout with cosmic rays

Checkout of FT-Hodo with cosmics	
Full checkout of the whole FT Hodoscope installed in Hall-B	Installation of hodoscope in CLAS12. <ul style="list-style-type: none"> <li>• Mounting of device onto supports</li> <li>• Cable routing of input voltage and signal readout cables</li> <li>• Connection of readout to ADC/TDC modules</li> </ul> Signal test of all hodoscope detector elements in-situ using cosmics. Software analysis for comparison of relative timing and MIP efficiency of individual hodoscope elements
Manpower and time needed	2-3 days HallB technician and Edinburgh researchers 1 week checkout Edinburgh researchers 1/2 week JLab DAQ expert to integrate ADC and TDC output from FT -hodo into recorded data stream
Software for analysis of results	NA

Computing resources	NA
Dependencies from other systems	CLAS12 trigger and DAQ. Will require development of FT-Hodo stand alone cosmic trigger
Information to be saved in the database	NA

### 6.2.3 FT-Trck, Checkout

A detailed description of MM checkout is reported in the MM commissioning plan. FT-MM will adopt the same procedures reported there.

Here are described special runs and procedures that will be performed to get first calibration data for the system including pedestal runs, laser runs, measurement with radioactive sources etc.

### 6.2.4 FT-CAL, LED monitoring

Special Run # FT-Cal LED monitoring	
Description	Measurement of the response of each channel to LED pulses
Goal	LED run to check (individually): - Channel functionality - linearity; - gain stability - timing - noise and resolution
DAQ Configuration and Trigger	CLAS12 DAQ and trigger with a special FT-CAL-LED configuration
Manpower and time needed	2 day 1 person
Software for analysis of results	Monitoring histograms to be implemented in standard CLAS12 special run monitoring
Computing resources	ND
Dependencies from other systems	Stand-alone tests
Information to be saved in the database	TBD

## 6.3 Calibration with cosmic rays

Here are described the conditions and goals of data taking with cosmic rays.

Run # FT Cosmic Ray calibration	
Description and goals	Measure the FT-Cal response to cosmic ray for (individually) <ul style="list-style-type: none"> <li>• gain matching</li> <li>• absolute light output</li> <li>• time synchronization with respect to CLAS12 (trigger)</li> <li>• absolute time</li> </ul> Measure the FT-Hodo response to cosmic rays <ul style="list-style-type: none"> <li>- gain matching</li> <li>- absolute light output</li> <li>- test coincidence timing between hodoscope elements</li> <li>- test coincidence timing between hodoscope elements &amp; forward tagger</li> <li>- time synchronization with respect to CLAS12</li> </ul> Measure the FT-Micromegas response to cosmic rays (see detailed MM commissioning plan) <ul style="list-style-type: none"> <li>-</li> </ul>
DAQ Configuration and Trigger	Dedicated FT-Cal-COSMIC trigger and daq configuration. Dedicated FT-HODO COSMIC Trigger
Dependencies from other systems	F-TOF, DC, CLAS12-trigger
Manpower and time needed	Few days for data tacking and 2 weeks of analysis
Software for analysis of results	Reconstruction software with matching between FT-Cal and other CLAS12 sub-systems (F-TOF, DC and trigger)
Computing resources	Minimal requirement of central systems
Information to be saved in the database	TBD
Repetition frequency	Any available time, 1 per week at least

## 6.4 Commissioning with beam

Here are the run conditions and configurations that are foreseen for this system in the initial phases of operation with beam to check the system and to perform a complete calibration of the detector.

### 6.4.1 Beam run - FT $e^-$ calibration

Beam Run # FT electron calibration	
Description and goals	Use the elastic electron scattering to measure the FT response (FT components alignment and absolute efficiency, FT-Cal energy and position resolution, FT-MM position resolution, FT-Hodo response to MIPs) to scattered electrons in the energy range 0.5-5 GeV tagging the proton Different current sets :Minimum possible current ( $I=100\mu A$ ) to 10E34, E=1,2,3,4,5,6 GeV LH2 standard 5cm target, thin target for alignment Magnets configuration: TBD after running detailed MC simulations

DAQ Configuration and Trigger	Standard CLAS12 DAQ configuration + FT trigger
Dependencies from other systems	All CLAS12 on, and in particular the CD to tag the proton
Manpower and time needed	1 week (?)
Software for analysis of results	CLAS12 reconstruction software
Computing resources	?
Information to be saved in the database	TBD
Repetition frequency	Once at the beginning of CLAS12 operations. Dedicated calibration procedures make using of the standard data will be developed

### 6.4.2 Beam run - FT $\pi^0$ calibration

Beam Run # FT $\pi^0$ calibration	
Description and goals	Use the reaction $p(e,e'\pi^0)$ to measure the FT response (FT-Hodo veto efficiency, FT-Cal resolution via $M\pi^0$ reconstruction, background in FT-M) to $\pi^0$ induced em shower, detecting the scattered electron and the proton Current scan (from minimum to nominal luminosity) E=6, 9GeV LH2 standard 5cm target Magnets configuration: TBD after running detailed MC simulations
DAQ Configuration and Trigger	Standard CLAS12 DAQ configuration + FT trigger
Dependencies from other systems	All CLAS12 (CD+FD)
Manpower and time needed	1 week (?)
Software for analysis of results	CLAS12 reconstruction software
Computing resources	?
Information to be saved in the database	TBD
Repetition frequency	Once at the beginning of CLAS12 operations. Dedicated calibration procedures make using of the standard data will be developed

## 7 FT DAQ and trigger

The hardware trigger for the MesonEx experiment should be designed to allow quasi-real photoproduction and electroproduction measurements to run in parallel. In electroproduction runs, both the scattered electron and the hadronic final state are detected in the CLAS12 detector. For meson spectroscopy, scattered electrons will be detected in the FT and hadronic final states in CLAS12. To be able to collect data for both experiments at the same time, the CLAS12 DAQ system should be able to trigger and record both types of events. For electroproduction experiments, a single electron trigger will be employed while, for meson spectroscopy, the DAQ will be triggered by the coincidence of a multi-particle final state in CLAS12 and a signal in the FT within the relevant energy range. The main requirements for the trigger is to be  $\sim 100\%$  efficient for the final states of interest and not to exceed the DAQ readout limit by keeping the background rate as low as possible.

### 7.1 Trigger requirements

CLAS12 will have a free running DAQ system. ADCs and TDCs will collect data in pipeline mode. Readout of data will be done after the trigger decision is made with an expected event rate of  $\geq 10$  kHz [20]. The new CLAS12-DAQ front-end electronics, in particular the use of flash ADCs (fADCs) for calorimeters, time-of-flight and Cherenkov counters, and the availability of fast field-programmable gate arrays (FPGA) will allow to employ a multi layer trigger system [20]. The trigger will have a fast cluster finding algorithm (already implemented in the CLAS1C read-out) with energy and position reconstruction in EC, and hit position and signal strength reconstruction in Cherenkov and time-of-flight counters. These requirements will be implemented at the Level-1 trigger, using features of fADCs and crate trigger processing (CTP) boards. At Level-2, track seg-

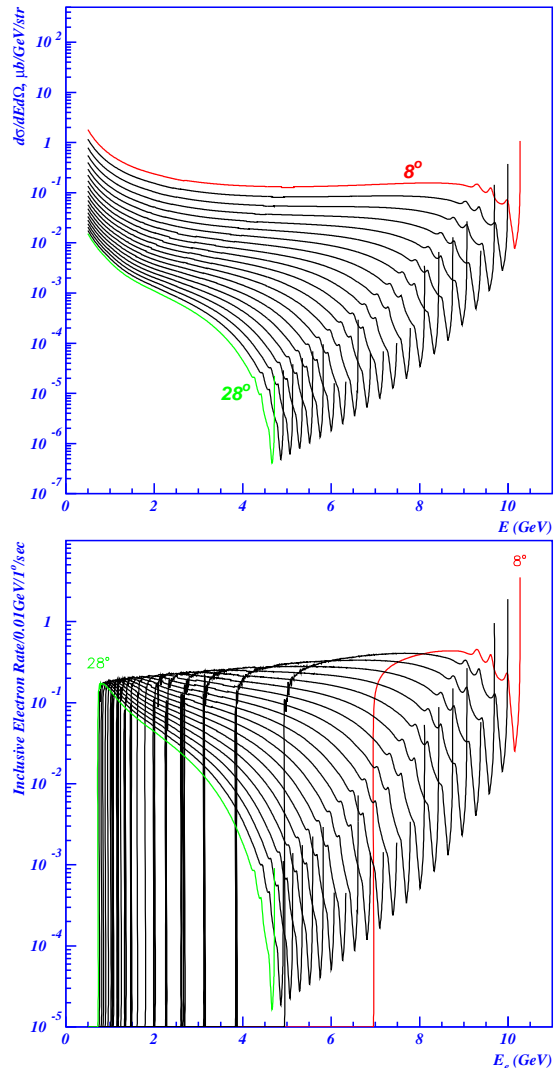


Figure 127: Cross sections (top) and rates at  $10^{35} \text{ cm}^{-2} \text{ sec}^{-1}$  (bottom) for inclusive electron scattering,  $ep \rightarrow e'X$ , at 11.5 GeV as a function of scattered electron energy, for scattered angles from  $8^\circ$  to  $28^\circ$ . Calculations done using the code of Ref. [45].

ment finding, track linking, and track position information in drift chambers will be used. Summing all contributions, the overall time for Level-1 and Level-2 trigger decision making is  $< 10 \mu\text{s}$ . At the next step, before recording the event, the Level-3 software trigger will be employed: combining information from detectors and tracking will make the final decision on the event.

At luminosities and energies foreseen for

CLAS12 standard electroproduction experiments, such a complex trigger is important even for single electron trigger runs. Present experience with CLAS showed that a trigger system that uses sector-based coincidence of signals from calorimeters (with a cut on the total energy sum) and signals from Cherenkov counters (over a certain threshold), while being very efficient, has a very poor electron-selectivity. For example, at  $E_{beam} \sim 6$  GeV and  $L \sim 2 \times 10^{34} \text{ cm}^{-2} \text{ sec}^{-1}$ , only 7% of triggered events have an electron. Moreover, a simple sector-based Level-2 trigger involving the tracking is also inefficient for rejecting the background (non-electron) events since there is almost always a track found at the sector level. From the analysis of the remaining 97% of non-electron events, it turned out that most of events were produced via forward photoproduction [46] where a fake trigger was caused by accidental coincidences between the Cherenkov counter and the electromagnetic calorimeter. With higher beam energies (11 GeV) and higher luminosities ( $10^{35} \text{ cm}^{-2} \text{ s}^{-1}$ ), the expected purity of the trigger based on a simple, sector based trigger system will become worse.

To have a realistic estimate of requirements for trigger selectivity and to calculate the expected trigger rates, we studied the CLAS data collected in electron and real photon experiments with production of multi-particle final states. In the next two sections, we discuss the expected trigger rates for standard CLAS12 electroproduction and quasi-real photoproduction runs.

### 7.1.1 Electroproduction trigger rate

Inclusive electron rates were calculated using parametrization of electron scattering cross section with radiative effects from Ref. [45]. In Figure 127 top-panel, the radiative cross section for  $ep \rightarrow e'X$  as a function of scattered electron energy for several values of scattered electron angle (from  $8^\circ$  to  $28^\circ$ ) is shown. In the calculation the beam energy was as-

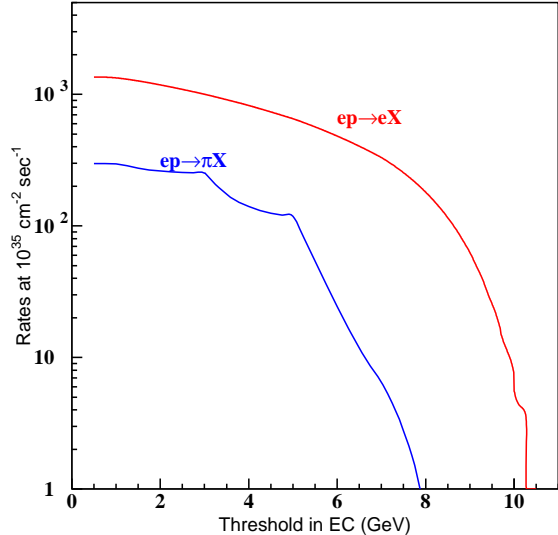


Figure 128: Trigger rates integrated over production angles as a function of the minimum energy (trigger threshold) for inclusive electron and  $\pi^{+/-}$  production at luminosity of  $10^{35} \text{ cm}^{-2} \text{ sec}^{-1}$ .  $\pi^-$  yields from Ref. [47] were used to estimate pion rates, assuming the  $\pi^+$  yield is twice the  $\pi^-$  yield. In the trigger, cuts on the number of photoelectrons in the HTCC and on deposited energy in the EC are used.

sumed to be 11.0 GeV. The corresponding rates at  $L \sim 10^{35} \text{ cm}^{-2} \text{ s}^{-1}$  within the CLAS12 geometrical acceptance, are shown in bottom plot of Fig. 127. The electron rate integrated over all angles and over the energy range from the minimum threshold energy to the end point as a function of the minimum energy is shown by the red curve in Fig. 128. Assuming a minimum momentum cut of  $\sim 0.5$  GeV/c, the total electron rate will be of the order of 1.5 kHz. The main source of background physics triggers is high energy pion production. Pion rates were estimated using pion yields measured in the reaction  $ep \rightarrow \pi^- X$  with CLAS [47], and assuming the  $\pi^+$  yield to be two times higher than the  $\pi^-$  yield. The charged pion rate in CLAS12 was then estimated in a similar way used for electrons, using the simulated performance of the high threshold Cherenkov counter (HTCC) and elec-

tromagnetic calorimeters (EC), together with the CLAS12 geometrical acceptances. In Fig. 128 the pions trigger rate is shown with a blue curve. With a low EC threshold ( $\sim 0.5$  GeV), the pion rate is of the order of 0.3 kHz, resulting in a total trigger rate of *electron-like* particles of less than 2 kHz. We expect the CLAS12 multi-layer trigger system will be 100% efficient for *electron-like* triggers and will be able to reject the other unphysical triggers (accidentals) at the 50% level. With this assumption, we expect to have  $\sim 4$  kHz trigger rate for electroproduction events.

### 7.1.2 Quasi-real photoproduction trigger rate

The reactions of interest for meson spectroscopy have three or more particles in the final state. Most of the rate comes from reactions with multiple pion photoproduction. As shown in Fig. 129, the cross section of processes with three or more pions levels-out around  $100\mu\text{b}$  for photon energies  $> 3.5$  GeV. With a luminosity of  $10^{35}\text{cm}^{-2}\text{s}^{-1}$ , the inclusive electron scattering rate on the FT, in the energy range of interest ( $E_{e'}=0.5\text{-}4.5$  GeV) is  $R_{\text{good}}=6.7$  kHz<sup>¶</sup>. This is the hadronic rate useful to study meson spectroscopy. From simulations we estimated the CLAS12 geometrical acceptance for the dominant three particle final state is

$$\epsilon_{3\text{prongs}}(E_{e'} = 0.5 - 4.5\text{GeV}) \sim 20\%$$

and therefore the expected trigger rate from multi-prong events (three or more particles) in CLAS12 will be:  $R_{\text{good}} \times \epsilon_{3\text{prongs}} \sim 1.3$  kHz.

<sup>¶</sup>It should be noted that the equivalent real-photon flux for a typical photoproduction experiment (bremsstrahlung beam on a  $L_T=30$  cm long liquid hydrogen target) that would give the same hadronic rate is:

$$\begin{aligned} \Phi_\gamma &= \frac{R_{\text{Hadronic}}}{L_T \times \rho_{\text{LH2}} \times N_{Av} \times \sigma_{\text{Total}}(E_\gamma \sim 10\text{GeV})} = \\ &= \frac{6.7 \text{ kHz}}{1.3 \times 10^{10}} = 5 \times 10^7 \gamma/s \end{aligned}$$

where  $\rho_{\text{LH2}}=0.07$  g/cm<sup>3</sup>,  $N_{Av}=6 \cdot 10^{23}$  and  $\sigma_{\text{Total}}(E_\gamma \sim 10\text{GeV}) \sim 100\mu\text{b}$ . This value is similar to what the GLUEX experiment is expecting to run with [48].

On top of this, we should consider accidentals between hadronic events in CLAS12 and the total rate in the FT. The latter is given by two main contributions: the elastic radiative tail and the electromagnetic background. Both of them give no multi-particle events in CLAS12. The elastic radiative rate within the acceptance of the FT was estimated to be of  $R_{\text{FT-rad}} \sim 40$  kHz. As discussed in Sec. 2.7.7, the contribution of the electromagnetic background associated to the beam (Møller electrons and secondaries) is much higher than the total hadronic rate mentioned above. The overall electromagnetic background rate is of the order of 120 MHz but, assuming a threshold on the total energy deposited in the FT calorimeter of 500 MeV and limiting the maximum energy to 4.5 GeV we calculated  $R_{\text{FT-em}}=180$  kHz (see Sec. 2.7.7 for details). Since the optimization of the tungsten shield geometry is still in progress we are confident that  $R_{\text{FT-em}}$  can be further reduced. The suppression of the background outside the energy range of interest, requires the implementation of a trigger system, for both CLAS12 and the FT, capable of reconstructing clusters in the FT with thresholds on the minimum and maximum energy that will be developed for the experiment. To estimate the random coincidences between the FT and the CLAS12 we should consider the total hadron rate due to electroproduction. This is dominated by electron scattering below  $2.5^\circ$ , outside the FT coverage. From Ref. [49], the total electroproduction rate is equivalent to the photoproduction rate given by a bremsstrahlung beam at a luminosity approximately equal to 1/50 of the electron luminosity (multiplied by a factor that accounts for energy range). In our case this leads to

$$\begin{aligned} R_{\text{CLAS12}} &\sim \sigma_{\text{Total}}(E_\gamma \sim 10\text{GeV}) \times \\ &\times 3.6 \cdot 10^{33} \text{cm}^{-2}\text{s}^{-1} \times \\ &\times \epsilon_{3\text{prongs}}(E_{e'} = 0.5 - 10.0\text{GeV}) = \\ &\sim 36\text{kHz} \end{aligned} \tag{13}$$

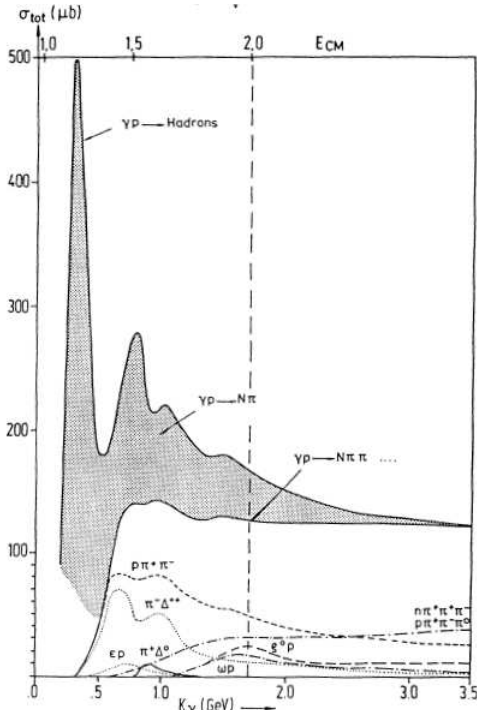


Figure 129: Total photoproduction cross section on proton as a function of photon energy, broken down into major final states which contribute.

where  $\epsilon_{3prongs}(E_{e'} = 0.5 - 10.0 \text{ GeV})$  was estimated to be of the order of 10% when averaged over the whole energy range. Considering the total rate in the forward tagger of  $\sim 220 \text{ kHz}$ , accidentals between CLAS12 and forward tagger in a coincidence window of 50 ns are expected to be in the order of  $R_{RND} \sim 1.0 \text{ kHz}$ , leading to a total rate ( $R_{good} + R_{RND}$ ) of coincidences between FT and CLAS12 of  $\sim 2.3 \text{ kHz}$ . Assuming, as in case of electron trigger, a CLAS12 trigger system selectivity for accidental triggers of 50%, the expected trigger rate for multi-prong events in CLAS12 from photoproduction events will be of the order of 4.6 kHz. This is a conservative estimate that can be refined by reducing rates in FT and CLAS12 and the time coincidence window between the two.

In summary, with a new, multi-level trigger system of CLAS12 and on the FT, electroproduction and quasi-real photoproduction experiments can be run together. The total

trigger rate, with 50% purity of accidentals in both electron and multi-prong triggers, will be  $< 10 \text{ kHz}$ , within limits of the CLAS12 DAQ.

## 7.2 Front-End for Fast Detectors

CLAS12 will have two calorimeters (EC and PCAL), two time-of-flight systems (TOF), two Čerenkov counters (LTCC and HTCC) and a forward tagger (FT). The number of channels per detector: EC - 1296, PCAL - 1152, TOF - 1080, LTCC - 216, HTCC - 48, CTOF - 100, FT - 600. The FT electronics will be JLab-designed flash ADCs in crates that are located on the Space Frame. A general schematic for the CLAS12 trigger is shown in Fig. 130. The 16-channel JLab-made Flash ADC (FADC) is still under development and was undergoing tests at the time of writing of this document. However, based on recent tests, CLAS12 can be equipped with 12-bit 250 MHz FADCs.

The FADCs are a significant part of the trigger system and will send prompt information to a Crate Trigger Processor (CTP) board installed in the same crate. The cluster information will include energy for every channel above threshold. A threshold will be applied to the energy sum of several consecutive hits. Information will be sent to the CTP over the back-plane serial bus every 16 ns. The CTP board is described in the Section 7.3.2, along with the energy summing algorithm.

## 7.3 CLAS12 Trigger

CLAS12 will have a two-level trigger system. The following sections contain an overview of the hardware-based Level 1 trigger components.

### 7.3.1 Trigger System Timing and Layout

Maximum trigger decision time is currently set to  $7 \mu\text{s}$  for Level 1, including about  $5 \mu\text{s}$  for the actual trigger processing and about

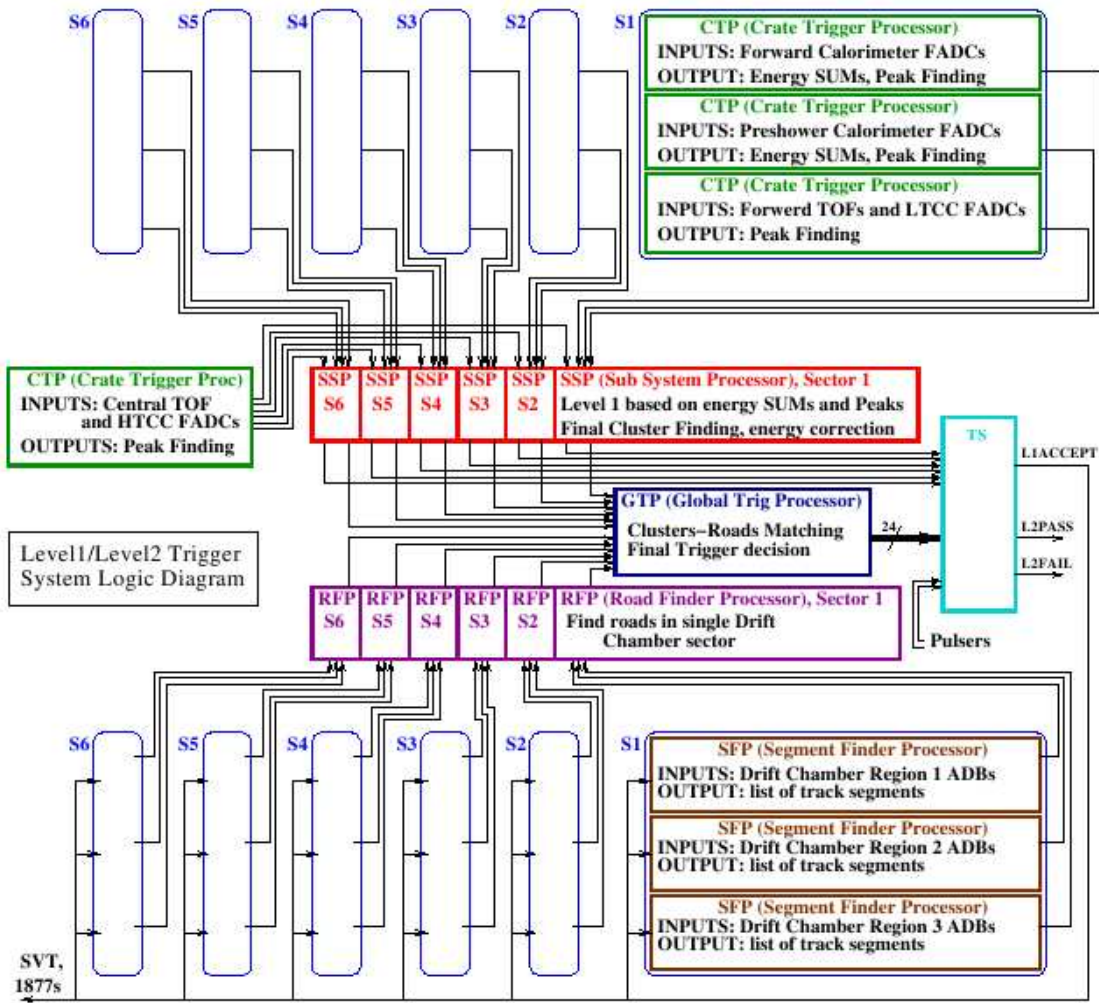


Figure 130: Generic scheme for the CLAS12 trigger system.

2  $\mu$ s for the signals propagation. All front end boards must assume 8  $\mu$ s for the trigger latency.

It is important to make sure that logically completed parts of the detector will not be wired to several FPGAs (field programmable gate arrays) inside CTP boards, which will make cluster reconstruction much more difficult. The current CTP board design contains two FPGAs collecting information from 8 FADC modules each: up to 16 FADC boards can be connected to a single CTP board. This layout will satisfy all possible Level 1 algorithms.

The timing scheme of the trigger system is shown in Fig. 131.

### 7.3.2 Level 1 Trigger

The Level 1 trigger system is based mostly on fast detectors equipped with FADCs. The first stage components of the trigger hardware are incorporated into the Data Acquisition elements (VXS crates), while the final decision is made in a specialized trigger crate containing Level 1 Routers (SSPs). The system is driven by a 16 ns global clock with internal FPGA 4 ns clock.

The VXS crates contain two trigger sys-

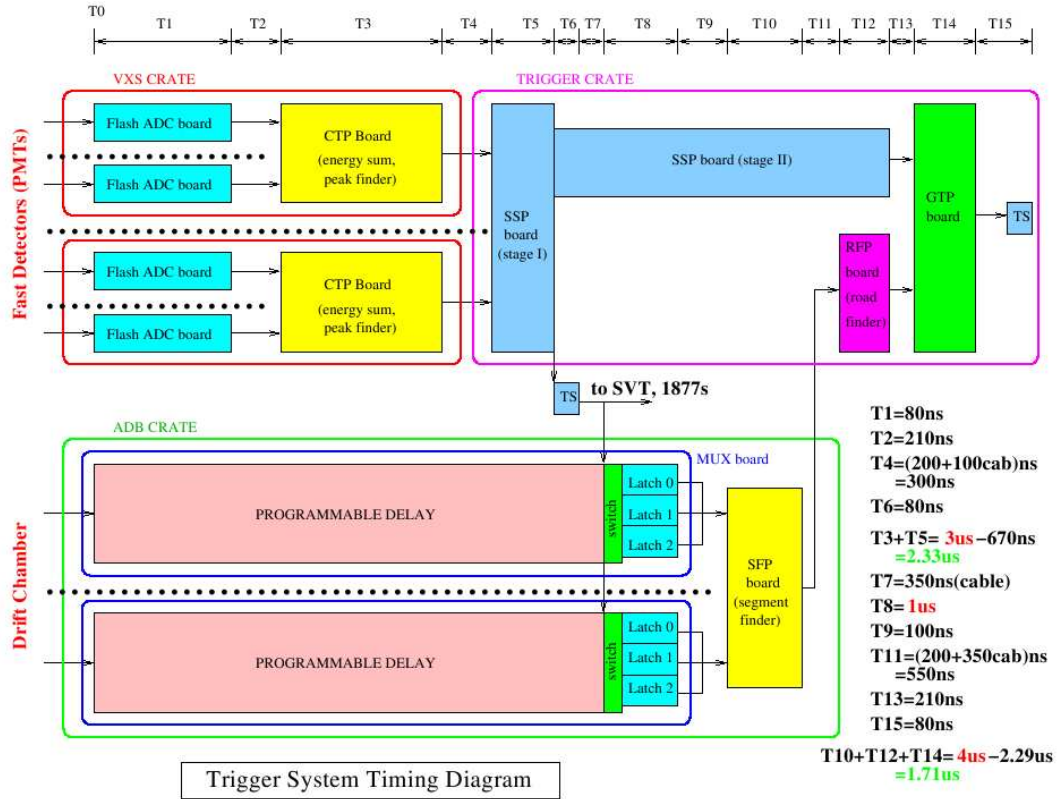


Figure 131: Level-1 and Level-2 trigger timing diagram for CLAS12.

tem components: processing units on the FADC processing (T1), data transfer over the VXS boards and Crate Trigger Processors (CTPs) boards collecting data from the Flash ADCs over fast serial lines. The CTB boards search for clusters in the electromagnetic calorimeters and other detectors, and send the results to the following stage of the trigger system. A sample signal processing algorithm running on a FADC board processing unit is shown in Fig. 132.

Racks with Trigger and DAQ electronics are located on Levels 0,1 and 2 on Forward Carriage and Levels 1 and 3 on Space Frame.

### 7.3.3 Level 1 Timing

The entire trigger system can be considered as a two-stage process.

The first stage is the Level 1 PMT-based trigger, which includes the FADC on-board

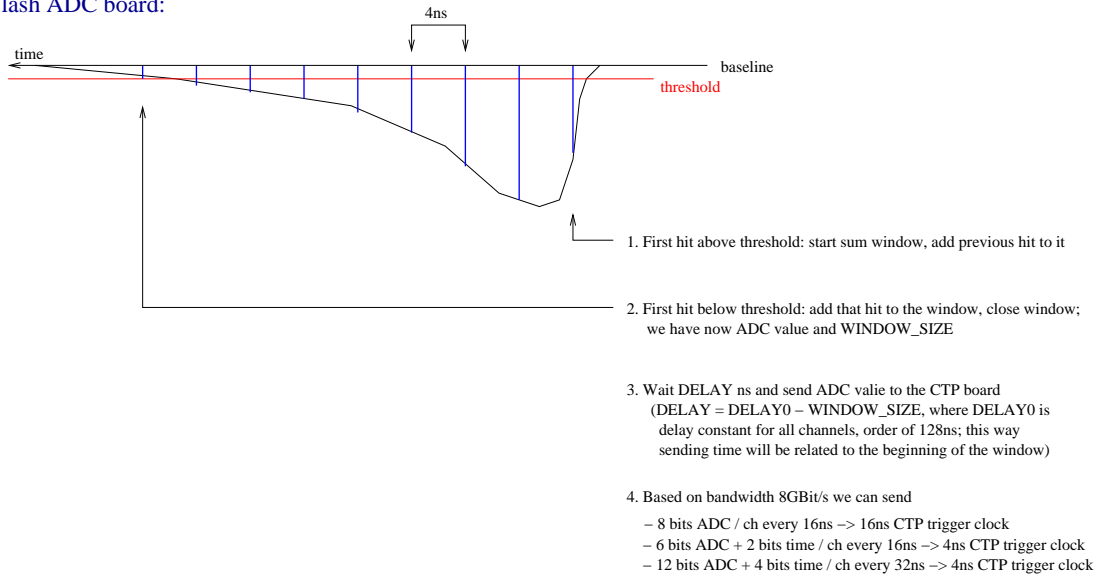
backplane serial bus (T2), cluster finding (T3), data transfer to the trigger crate (T4), sector-based Level 1 decision (T5), and data transfer to the following trigger stages. The T3 and T5 time intervals can be different for different run periods, so the programmable delay must be reprogrammed accordingly.

Stage two is the final Level 1 trigger processing stage in the sector-based Level 1 routers (track finding and inter-detector matching), and in the Event Processor (the entire CLAS12 trigger) (T11). The total trigger decision time must be less than  $7 \mu s$  to satisfy the front end electronics constrains.

### 7.4 Readout Controllers

Readout Controllers (ROCs) are installed in every FASTBUS, VME, VME64X, and VXS

### Flash ADC board:



### CTP board:

1. Does not have information about original sum window width
2. Expands every window up to the value (programmable) big enough to enforce coincidence between different channels
3. Every channel has programmable delay (4ns step) and readable scaler

Flash ADC board signal processing logic

Figure 132: Example of a signal processing algorithm for triggering on the FADC board.

crate. The ROCs are collecting data from the front-end boards, processing it and sending it to the Event Builder over the network. Currently we employ mvme6100 controllers with a prpmc880 or pmc280 co-processor modules. That configuration is fast enough to meet the CLAS12 requirements and more co-processor modules can be installed if necessary. By the time of CLAS12 startup, a new generation of ROCs (including multi-processor and multi-core units) will be available. First GE-made boards running CentOS Linux were tested and promising performance was observed.

## 7.5 Computing and Network

A Foundry BigIron RX-8 switch is currently used as the backbone of the DAQ system. The Event Builder, Event Recorder, and other critical DAQ components for CLAS are running on 4-CPU Opteron-based servers, and that configuration is sufficient for CLAS12 as well. ROCs are linked to the BigIron switch

through smaller switches with up to four GBit uplinks, new 10Gbit uplink switches will be installed. The CLAS data storage system (RAID5) is sufficient for up to a 150 MB/sec data rate.

All available equipment is good enough to satisfy the CLAS12 requirements, but most likely we will upgrade most of the components because of aging and maintenance considerations. The performance of the link to the JLab Computer Center tape storage must be increased up to at least 200 MB/s.

## 7.6 Forward Tagger Trigger

The Forward Tagger (FT) consists of three main subsystems:

1. The Forward Tagger electromagnetic calorimeter (332 channels)
2. The Forward Tagger hodoscope (232 channels)
3. The Forward Tracker (4k channels)

The FT calorimeter and FT hodoscope will participate in the trigger decision. The FT trigger has to identify charge particles with definite energy deposition in the FT calorimeter. The geometrical matching between the hodoscope counters and the cluster in the calorimeter will identify charged particles (electrons).

The FT trigger will select events with an electron in the FT and a multi-prong event in CLAS12. The multi-prong event may include both charged and neutral particles. The CLAS12 drift chamber trigger electronics will identify charged tracks and measure the charge and coordinates of the particles. The matching between the track and the counters in the TOF system will reduce the background rate. Neutral particles will be detected by the CLAS12 electromagnetic calorimeter and preshower calorimeter.

The final trigger decision will include an electron in the Forward Tagger and a programmable number of charged tracks or neutral particles in CLAS12.

### 7.6.1 Level 1 FT Trigger

The Level 1 FT trigger system will be done the same way as for the fast PMT-based detectors (see section 7.3.2). The first stage components of the trigger hardware are incorporated into the Data Acquisition elements (VXS crates), while the final decision is made in a specialized trigger crate containing Level 1 Routers (SSPs).

The VXS crates will contain two trigger system components: processing units on the FADC boards (Fig. 132) and CTP boards collecting data from the FADCs over fast serial lines. The CTP boards search for clusters in the FT calorimeter, and send the results to the next stage of the trigger system, where the match between the calorimeter and the hodoscope is done.

At the final stage, matching between the FT and other CLAS12 detectors will create a final trigger decision.

In the following we present the proposed configuration for the Level 1 Trigger devices, i.e. FADC and CTP, focusing on calorimeter requirements. The configuration is derived from the HPS experiment test run [50, 51] that took place at Jefferson Lab in spring 2012.

#### FT-Cal and FT-Hodo FADC Configuration

In the present production firmware FADC-1 the FADC board trigger works as follows: after power-up, software programming configuration, and synchronization the board is continuously sending a 16-bit sum value to the CTP through the high-speed gigabit serial interface. This sum value is the total sum of all sixteen front end ADC chips for every 4 ns sampling period. The high speed gigabit interface is currently capable of transferring 4 Gb/s. Fig. 133 shows a block diagram of the 16-bit sum process.

**FT-Cal CTP Configuration** The proposed FADC trigger processing algorithm, already used for the HPS experiment test run, is shown in fig. 134. Each FADC board in a VXS crate reports to the CTP 1 byte/channel every 32 ns, to meet the 4 Gb/s transfer bandwidth per board currently available. Five bits are used to report individual channels energy sum: they correspond to an energy resolution of  $\simeq 50$  MeV. The sum is performed only for samples above a programmable threshold. Last 3 bits are used to report the cross-threshold time within the 32 ns time window, with 4 ns resolution.

This firmware has already been implemented and tested for the HPS test run, and is currently available for use. At the time this document is being written there are efforts to further improve the trigger capabilities of the FADC board, in particular to increase the trigger energy resolution and to embed calibration constants for each channel inside the board.

The CTP will receive Gigabit serial data

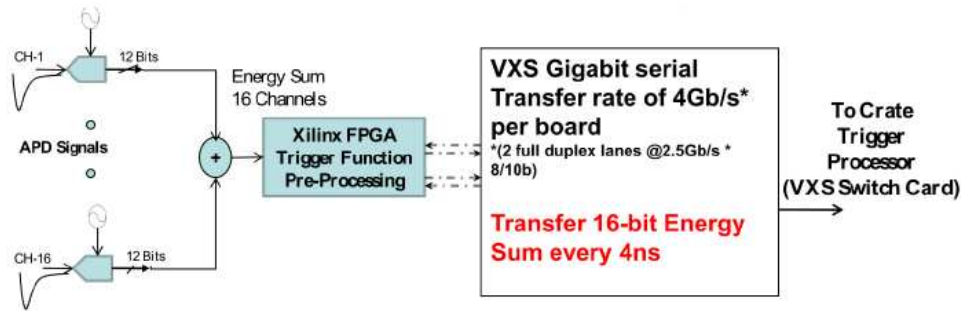


Figure 133: Scheme of the current JLab FADC firmware: the 16-bit “Board Sum” value is reported every 4 ns to CTP.

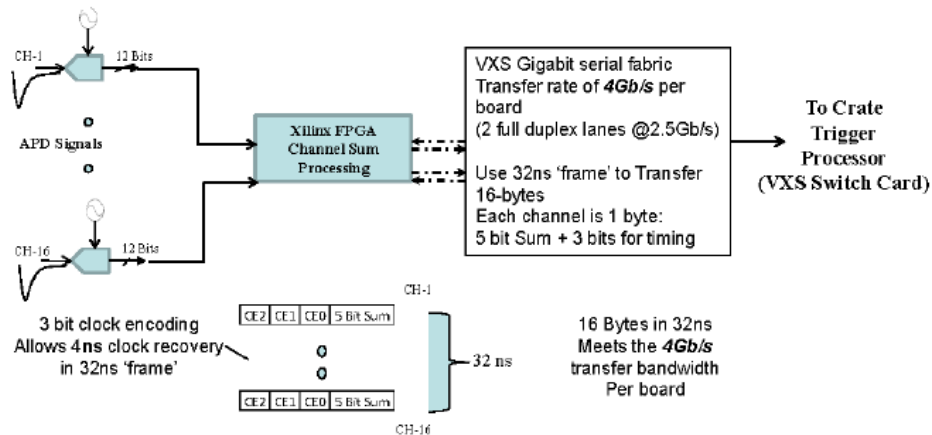


Figure 134: Scheme of the new JLab FADC firmware: individual channel sum and 4 ns resolution for signal threshold crossing are implemented.

streams from each of the sixteen FADCs modules in a VXS crate, in the new data channel-based format described in the previous paragraph (3 bits for timing and 5 bits for energy sum). Data will be received and processed on a frame by frame basis, each frame being 32 ns long.

An algorithm performing cluster-finding on 3x3 matrix of channels is currently available. Hits are added together if they occur within a programmable number of clock cycles. If the matrix energy is greater than a programmable threshold a cluster is found and its relevant information are reported to the above trigger level (time, energy, position, hit pattern).

This algorithm will be tested soon to match it with our experimental conditions.

**FT-Hodo CTP configuration** The CTP in the FT-Hodo VXS crate will search for matched hits in the two layers of the detector, and send relevant information to the above trigger level (time, energy, position).

### 7.6.2 Level 2 FT Trigger

Final trigger decision will be taken at the second trigger level, requiring for an electron in the Forward Tagger through the coincidence of the FT-Cal and the FT-Hodo, as well with a programmable number of charged tracks or neutral particles in CLAS12.

The coincidence algorithm, embedded inside SSPs, will be studied and implemented as soon as the first level trigger is developed.

### 7.7 FT fADC channel distribution

A VXS crate can host up to 16 FADCs, for a total of 256 channels. The FT-Cal has 332 independent channels, so 2 different crates must be used for the read-out. Due to the limited interconnection capabilities of the CTP boards, channels routed to different crates cannot be analyzed together during cluster finding. We are thus planning to divide the calorimeter in two-halves for readout, 176 channel each, as shown in fig. 135. The signal of the 14 channels on the borders (dark-coloured in the figure) will be split twice and sent to both crates. This requires one more FADC board, for a total of 12 per crate.

The FT-Hodo has 232 channels, requiring 15 FADC boards for readout. They can be hosted in a single crate, thus a single CTP can analyze signals from the whole detector.

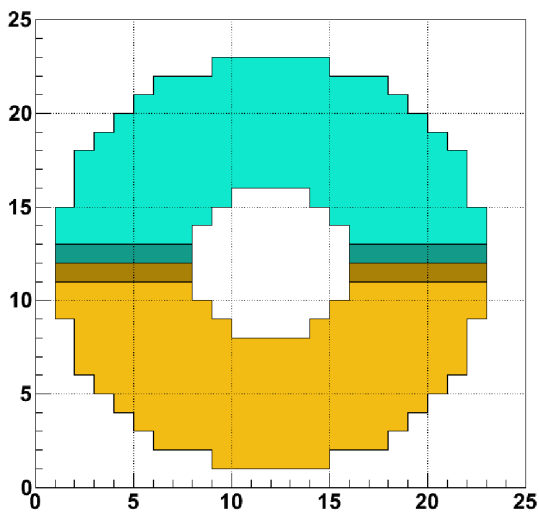


Figure 135: Calorimeter channel distribution: channels in the halves of the calorimeter are connected to the two VXS crates; dark-coloured channels are splitted and sent to both VXS crates.

## 8 FT Performance

### 8.1 GEANT4 simulations

Detailed simulations of the FT to understand kinematics, backgrounds and the detector response have been done with the GEANT4-based Monte Carlo code for CLAS12, GEMC [39]. The FT-Cal, FT-Hodo and FT-Trck geometries were realistically implemented in the simulation code, as discussed in Sec. 2.7 and 4.1.1. Fig. 136 shows a section of the FT and CLAS12 in the GEANT4 viewer. Both the active and passive elements were included to take into account all the materials crossed by particles before hitting the FT or the CLAS12 forward detector. For this reason, also the extension of the FT-Cal motherboard and the FT-Trck front-electronic crates, located in the shadow of the torus coils, were included in the implementation. The FT is shielded from Møller electrons produced by the interaction of the beam in the target by a tungsten cone covering polar angles up to  $2.45^\circ$ . The location and shape of the shield were chosen in order to minimize the radiation on the FT and on CLAS12, compatible with the most recent design of the CLAS12 beamline. This Møller shield is attached to the tungsten pipe, located at the center of the crystal assembly and connected to the main CLAS12 beampipe. The design of the shield will be finalized with further simulation studies.

The purpose of the simulations was to evaluate:

- the acceptance and resolution for the electron detection,
- the background rates on the FT and the related impact on the electron reconstruction,
- the CLAS12 drift chamber occupancy to verify the compatibility of the FT with the CLAS12 operation at full luminosity.

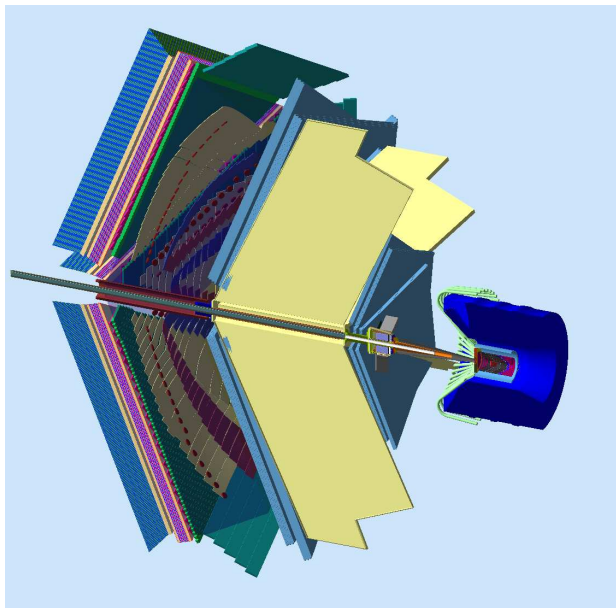


Figure 136: GEANT4 implementation of the Forward Tagger in CLAS12. The Forward Tagger is located between the forward drift chambers in light blue and the central detector.

The results of these studies are described in the next subsections.

#### 8.1.1 Acceptance

The GEMC simulations were first used to understand the electron kinematics and the FT acceptance. For this purpose electrons with momentum from 0.05 to 5 GeV and polar angle from  $1^\circ$  to  $35^\circ$  were generated at the target location. The trajectory of the electrons is affected by the 5-Tesla solenoid field, which induces a rotation of the particle around the beamline because of its non-zero transverse momentum component. This results in a significant shift of the azimuthal angle  $\phi$  of the track, while the polar angle  $\theta$  remains almost unchanged, except for very low momenta. This feature does not affect significantly the overall acceptance of the FT in the kinematics of interest, while it provides a mean to reconstruct the particle trajectory using the two tracking layers described in Sec. 4. The over-

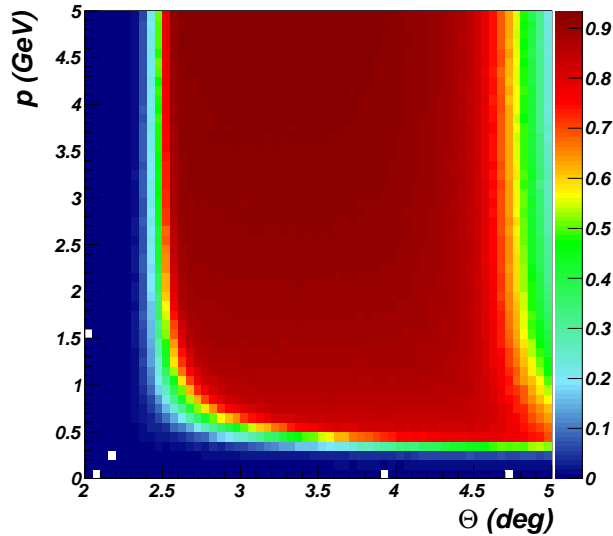


Figure 137: GEMC simulation results. FT electron detection efficiency as a function of momentum and angle. The efficiency is high and uniform throughout the kinematic range of interest (momentum: 0.5 – 4.5 GeV,  $\theta$ : 2.5° – 4.5°) except for electrons with both low momentum and small angles that are bent out of the detector acceptance by the solenoidal field.

all acceptance is shown in Fig. 137: the ratio of electrons absorbed in the FT calorimeter over the generated ones is shown as a function of the electron momentum and polar angle. Here an electron is considered as detected by the calorimeter if the reconstructed energy is within 10% of the generated one. The acceptance is very high and uniform throughout the region of interest, with average value well above 90%. A small loss of acceptance is found for electrons with small momenta and angles that are bent out of the acceptance of the FT by the CLAS12 solenoid field.

### 8.1.2 Energy resolution

The final energy resolution estimated for the FT is shown in Fig. 138. This was obtained assuming a 10 MeV energy threshold on the single crystals and running the cluster reconstruction algorithm developed for the FT-Cal

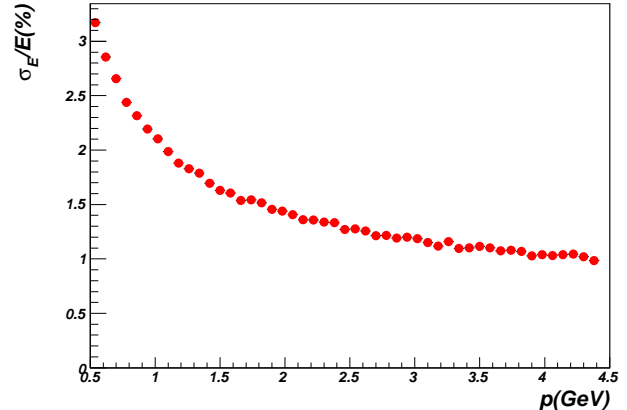


Figure 138: GEMC simulation results. Expected energy resolution for the FT, based of full GEANT4 simulations.

reconstruction.

### 8.1.3 Spatial resolution

As mentioned above, the 5 T solenoidal field induces to the particle a rotation. The top panels of Fig. 139 show the difference between the azimuthal angle (top-left) and polar angle (top-right) of the electron tracks at the two tracking planes as a function of the momentum. The size of the  $\phi$  rotation directly depends on the momentum and only marginally on the polar angle. By measuring this rotation it is therefore possible to infer the electron momentum as well as reconstruct the vertex angles. Assuming a spatial resolution of the tracker of 200  $\mu\text{m}$  and the presence of air between the two tracking planes, the angular resolution estimated from these simulation is of  $\sim 2.8$  degrees in  $\phi$  and about 1.7% in  $\theta$ .

## 8.2 Count-rate and occupancy

### 8.2.1 CLAS12 DC occupancy

One of the limiting factors for the operation of CLAS12 at high luminosity is the Drift Chambers (DC) occupancy. In the CLAS12 configuration without the Forward Tagger, the

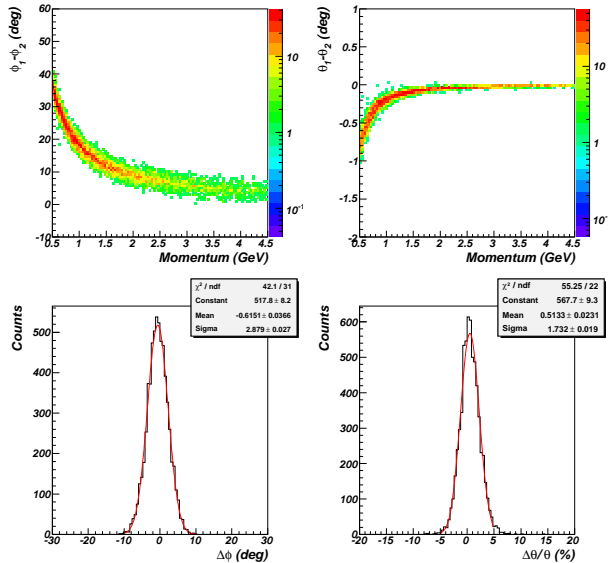


Figure 139: GEMC simulation results. Top: difference between the azimuthal and polar angles measured at two tracking planes as a function of the particle momentum. Bottom: resolution on the reconstruction of the particle vertex angles estimated from the simulation assuming  $200 \mu\text{m}$  spatial resolution of the tracker and the presence of air in between the tracking planes.

DC occupancy is expected to be of the order of 1-2%, as estimated from GEANT3 simulations [53]. This value was obtained by inserting a Møller shield made of aluminum and tungsten and covering angles up to about 4 degrees. This shield is not compatible with the operation of the Forward Tagger. Therefore, we performed a dedicated study to evaluate the DC occupancy with the FT, optimizing the geometries of the FT mechanical structure and of the Møller shield. The interaction of the beam with the target was simulated generating electrons upstream to the interaction region, within a 250 ns window corresponding to the integration time of the DC readout. The secondaries that are produced were tracked throughout the CLAS12 volume and the rates of the different detector components were computed. The resulting DC occupancy for the nominal luminosity of  $10^{35}$

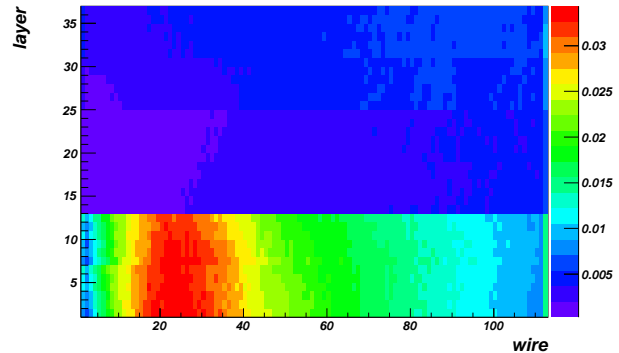


Figure 140: Drift Chamber occupancies at  $10^{35} \text{cm}^{-2}\text{s}^{-1}$  luminosity as a function of wire and layer number. The maximum occupancy value of about 2% is found in Region 1 while occupancies in Region 2 and 3 are less than 1%. These values are comparable to what estimated in the standard CLAS12 configuration without the FT and are within acceptable values.

$\text{cm}^{-2}\text{s}^{-1}$  is shown in Fig. 140. The measured rates are higher in the first two superlayers of Region 1, since the background is dominated by low energy particles coming from the target region and the Møller shield. These secondaries are easily stopped by a small amounts of material, and therefore rates drop in Region 2 and 3. DC occupancy is always below 2.5% and therefore within acceptable values. It is worth to mention that, implementing the geometry of the standard CLAS12 shield in GEMC, we are able to reproduce the same results obtained with GEANT3 simulations.

### 8.3 Benchmark studies

The effect of the FT performance on the electron detection in combination with the expected CLAS12 reconstruction of hadrons has been studied on some selected channels (benchmark reactions) representative of the MesonEx experimental program.

The simulations were based on the CLAS12 Fast Monte Carlo (FASTMC) [54], which uses parametrization of the detector acceptance and resolution for different particle types. The

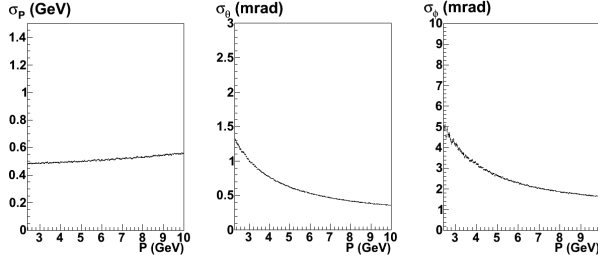


Figure 141: FASTMC resolutions for  $e^-$  at  $\theta = 15^\circ$ . The curves are based on GEANT4 simulation of the CLAS12 tracking system and reconstruction by the SOCRAT package [55, 20].

parametrization of angular resolutions were updated to agree with the most recent Monte Carlo tracking results [20, 55] and are shown in Fig. 141.

The acceptance for the tagger was assumed to be 100% in the range  $0.5 < E_{e'} < 4.5$  GeV and  $2.5^\circ < \theta_{e'} < 4.5^\circ$ . The angular resolution was determined from GEMC simulation studies, detailed in Sec. 4, assuming a spatial resolution for the tracking detector of  $200 \mu\text{m}$ . The resulting angular resolutions used were,  $\sigma_\theta = (0.017 \cdot \theta)$  and  $\sigma_\phi = 2.8^\circ$ . The energy resolution of the FT was parametrized for three different assumptions on the calorimeter structure:

1. the existing CLAS-IC  $\text{PbWO}_4$  calorimeter [24]
  - $\sigma_P = \sqrt{0.02^2 + 0.03^2 P + 0.024^2 P^2}$  GeV,
2. the proposed PANDA-EMC  $\text{PbWO}_4$  calorimeter [23]
  - $\sigma_P = \sqrt{0.02^2 P + 0.01 P^2}$  GeV,
3. a poorer resolution sampling calorimeter or equivalent
  - $\sigma_P = 0.2\sqrt{P}$  GeV.

Different reactions were studied using reasonable assumptions on productions mechanisms. Events were generated via the Monte Carlo

technique, projected onto the detector to determine acceptances and the 4-vectors smeared according to the above parameterizations.

In the following section we described the results obtained for two specific reactions:

- $\gamma p \rightarrow n\pi^+\pi^+\pi^-$ ,
- $\gamma p \rightarrow pK^+K^-\pi^0$ .

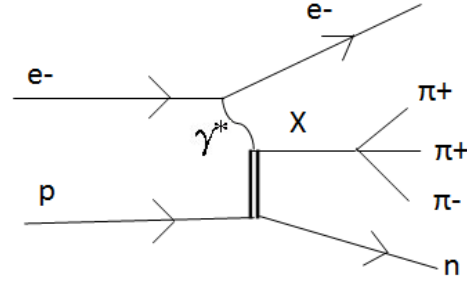


Figure 142: Feynman diagram of the reaction  $\gamma p \rightarrow n\pi^+\pi^+\pi^-$ .

### 8.3.1 The reaction $\gamma p \rightarrow n\pi^+\pi^+\pi^-$

The  $3\pi$  decay mode is one of the channels where evidence for the exotic  $\pi_1(1600)$  was reported. The controversy raised from the contradictory findings of different experiments makes further investigation of this final state highly desirable.

The  $\gamma p \rightarrow n\pi^+\pi^+\pi^-$  reaction can be easily accessed in the CLAS12 experimental setup by detecting the three charged pions in the forward part of the CLAS12 detector. The exclusivity of the reaction can be ensured by using the FT to determine the energy of the initial state photon and then applying the missing mass technique to select events with a missing neutron. To show that amplitude analysis is possible with CLAS12, a detailed Monte Carlo simulation and PWA are performed for this channel.

Initially, events were generated with a flat  $3\pi$  invariant mass and exponential  $t$  channel

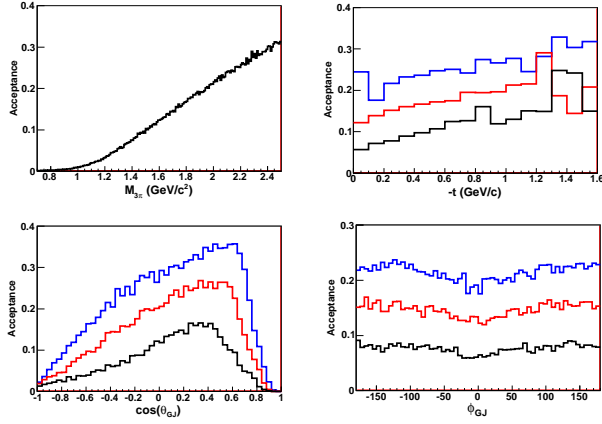


Figure 143: Acceptances for the  $\pi^+\pi^+\pi^-n$  final state and half CLAS12 field setting. Top left the  $3\pi$  invariant mass  $M_{3\pi}$ , right the momentum transfer  $t$ , bottom left,  $\cos\theta_{GJ}$  and right,  $\phi_{GJ}$ . For the latter 3 plots the black, red and blue lines correspond to  $M_{3\pi} = 1.4, 1.7$  and  $2.0$  ( $\text{GeV}/c^2$ ) respectively.

distribution,  $\frac{d\sigma}{dt} \propto e^{-5|t|}$ . The response of the CLAS12 and FT system to this channel was then analyzed after reconstruction with FASTMC. For this reaction, important kinematic dependencies of acceptance are the invariant mass of the  $3\pi$  system, corresponding to the resonance mass, the momentum transfer  $t$  and the angles of the isobar (e.g.  $\rho$ ) in the meson resonance decay. These are the variables that the production mechanism may depend from. The angles are commonly defined in the meson rest frame with the  $z$ -axis along the negative photon momentum and the  $y$ -axis defined as  $\underline{n} \times \underline{z}$ , where  $\underline{n}$  is the neutron direction. These are known as the Godfried-Jackson angles  $\theta_{GJ}, \phi_{GJ}$ . The acceptances for these 4 quantities are shown in Fig. 143 for the CLAS12 half field setting and Fig. 144 for the full field setting. Clearly the overall acceptance depends strongly on  $M_{3\pi}$  and the three other variables are shown for fixed  $M_{3\pi} = 1.4, 1.7$  and  $2.0$  ( $\text{GeV}/c^2$ ). Although the overall magnitude changes for the 3 masses, the shape of the other acceptances is similar for each. For the full field the acceptance is significantly poorer at low

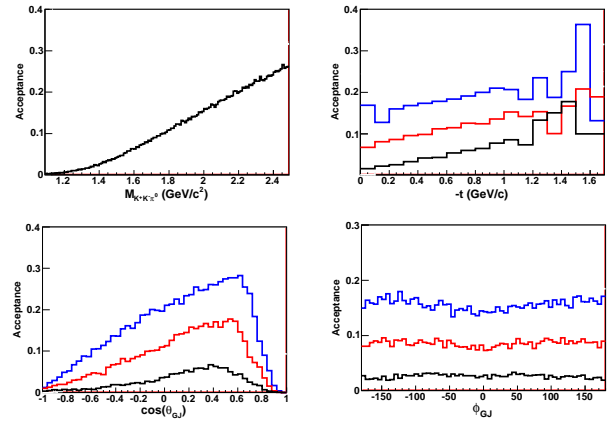


Figure 144: Acceptances for the  $\pi^+\pi^+\pi^-n$  final state and full CLAS12 field setting. Top left the  $3\pi$  invariant mass  $M_{3\pi}$ , right the momentum transfer  $t$ , bottom left,  $\cos\theta_{GJ}$  and right,  $\phi_{GJ}$ . For the latter 3 plots the black, red and blue lines correspond to  $M_{3\pi} = 1.4, 1.7$  and  $2.0$  ( $\text{GeV}/c^2$ ) respectively.

$M_{3\pi}$ , approximately a factor 5 at  $M_{3\pi} = 1.4$  and 2 at  $M_{3\pi} = 1.7$ . Nevertheless, the angular coverage is reasonable for  $\theta_{GJ}$  and almost flat for  $\phi_{GJ}$ , which is qualitatively good for a PWA.

Next, the exclusivity of the final state selection was tested by simulating the main possible background channel  $\gamma p \rightarrow n\pi^+\pi^+\pi^-\pi^0$ , which just required an additional  $\pi^0$  in the generator. In this case it is possible for the CLAS12 detector to miss both of the  $\pi^0$  decay photons, so only the 3 charged pions are reconstructed and this final state must be rejected by kinematics. Figure 145, shows the missing mass spectra of the 3 pions for the different models of the FT energy resolution described earlier. The plots only contain events with  $M_{3\pi} < 2.5$  ( $\text{GeV}/c^2$ ) since the background is lower above this mass. The  $3\pi$  and  $4\pi$  reactions were assumed to have the same cross sections for this test. For the  $4\pi$  events two cases are shown, with and without analyzing the  $\pi^0$  decay photons, to show the potential suppression from kinematics alone. It is clear from the plots that the two  $\text{PbWO}_4$  calorimeters offer substantial improvement in

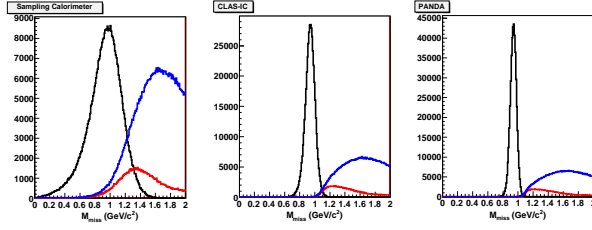


Figure 145: Missing mass of the detected  $3\pi$  system for generated  $3\pi$  events in black, generated  $4\pi$  events with 3 charged  $\pi$  detected, in blue and in red the same but with an additional cut on zero  $\pi^0$  decay photons detected. The left plot is for the sampling calorimeter model, middle, the CLAS-IC and right the expected PANDA calorimeter energy resolution.

final state selection compared to a sampling calorimeter. The PANDA calorimeter resolution gives near perfect rejection with the  $4\pi$  background amounting to just 0.03% within  $2\sigma$  of the neutron peak, while the CLAS-IC gives 0.7%. The sampling calorimeter by comparison contains almost 30%  $4\pi$  events in the  $2\sigma$  range. This analysis strongly supports the use of a homogeneous calorimeter with scintillating crystals comparable or superior to  $\text{PbWO}_4$  for the FT and that such a detector would allow identification of almost background free  $3\pi$  final states.

### 8.3.2 The reactions $\gamma p \rightarrow pK^+K^-\pi^0$ and $\gamma p \rightarrow nK^+K^-\pi^+$

Quasi-real photoproduction is likely to be one of the more promising mechanisms for the production of exotic mesons with hidden strangeness due to the relatively large  $s\bar{s}$  content of the photon. Photons are also expected to be efficient in the production of spin-1 hybrids. The first attempts to explore existing data from CLAS showed that the multiparticle reactions as

$$\gamma p \rightarrow (\phi\pi^0)p, \quad \phi \rightarrow K^+K^-, \quad \pi^0 \rightarrow \gamma\gamma \quad (14)$$

$$\gamma p \rightarrow (\phi\pi^+)n, \quad \phi \rightarrow K^+K^- \quad (15)$$

can be investigated [56].

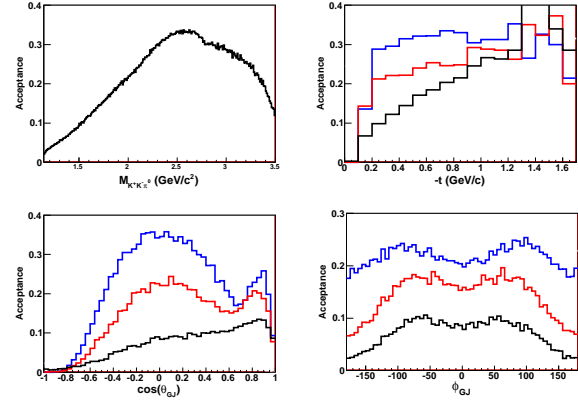


Figure 146: Acceptances for the  $K^+K^-\pi^0p$  final state, with the  $K^-$  reconstructed. Top left the  $K^+K^-\pi^0$  invariant mass  $M_{K^+K^-\pi^0}$ , right the momentum transfer  $t$ , bottom left,  $\cos\theta_{GJ}$  and right,  $\phi_{GJ}$ . For the latter 3 plots the black, red and blue lines correspond to  $M_{K^+K^-\pi^0} = 1.4, 1.7$  and  $2.0$  ( $\text{GeV}/c^2$ ) respectively.

The CLAS12 spectrometer has excellent momentum and angular resolution and particle identification. These features are extremely important for the mass determination and background reduction. The acceptance and resolution for resonances decaying to  $\phi\pi^0$  was studied assuming the resonance to be produced and decay via the reaction  $\gamma p \rightarrow Xp \rightarrow \phi\pi^0p \rightarrow K^+K^-\gamma\gamma p$ . Again the resonance  $X$  was produced with a  $t$  distribution,  $\frac{d\sigma}{dt} \propto e^{-5|t|}$ . In this case, the  $K^-$  from the decay of the  $\phi$  meson is mainly produced at very forward angle, i.e. typically below 15 degrees in the lab with an overall detection efficiency of about 2% due to the inbending of negative particles in the toroidal field. The detection of this particle leads therefore to a very strong reduction of the overall acceptance. A more efficient identification of this final state is achieved by detecting the proton, the  $K^+$ , the  $\pi^0$  via its decay to two photons and selecting the  $K^-$  in missing mass. The dependence of the acceptance on the mass of the  $\phi\pi$  system  $M_{K^+K^-\pi^0}$ ,  $t$  distribution and resonant decay angles  $\theta_{GJ}$  and  $\phi_{GJ}$  are shown in Fig. 146 for the half field setting for

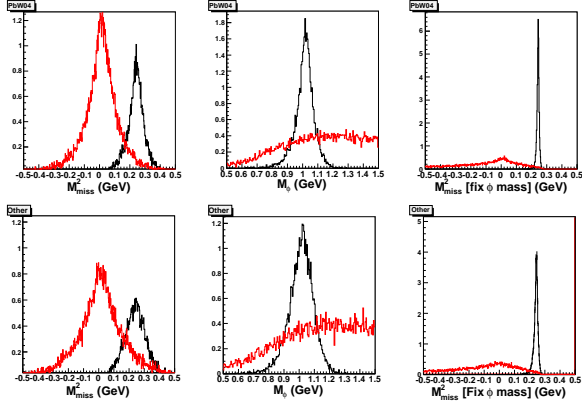


Figure 147: Reconstructed masses from the  $pK^+\gamma\gamma$  final state for the CLAS-IC tagger (top) and the lowest resolution tagger (bottom). In all plots, the black line shows the final state of interest, while the red line is for a phase space  $\gamma p \rightarrow K^+\pi^0\pi^-p$  reaction. The left plot shows the missing mass ( $\sim K^-$ ), the middle the reconstructed  $\phi$  mass and the right plot the missing mass having fixed the reconstructed  $\phi$  mass to 1.020 GeV.

CLAS12. They are similar to those obtained for the  $3\pi$  analysis and so the conclusion discussed in the next Section about the feasibility of PWA can be extended to this reaction as well. There is little effect on these acceptances for full magnetic field as the  $K^-$  is not detected in CLAS12.

Figure 147 shows the reconstructed masses from the  $pK^+\gamma\gamma$  final state. Also shown is a phase space  $\gamma p \rightarrow K^+\pi^0\pi^-p$  background. The missing masses have widths of 0.054 and 0.093 GeV for the CLAS-IC and low-resolution tagger respectively. The resolution is the same for the reconstructed  $\phi$  mass. Again, the capability to determine the photon energy with a good resolution is crucial to be able to study this reaction channel with a sizable efficiency and a good signal to background ratio.

#### 8.4 GEANT4 simulations of the reaction $\gamma p \rightarrow nX \rightarrow n\pi^+\pi^+\pi^-$

Similar acceptance and resolution studies were repeated with full GEANT simulations of the

$\gamma p \rightarrow nX \rightarrow n\pi^+\pi^+\pi^-$  reaction. The final state was generated using the approach described in Sec. 8.3.1. The four-vectors of the final state particles were saved in LUND format and fed to the CLAS12 simulation software, GEMC. Simulated events were then reconstructed using dedicated algorithms to reconstruct the electron in the FT and the SOCRAT tracking code [57] to determine the momenta and angles of three charged pions in CLAS12. The electron reconstruction in the FT was performed requiring matching hits in the FT-Trk, FT-Hodo and FT-Cal. First signals in the tracker were analyzed to identify electron hit candidates. Matching between hits in the two tracking planes were required to suppress noise and improve the spatial resolution. The resulting hits were then matched to clusters in the calorimeter, by imposing cuts on the relative transverse distance. The calorimeter energy information was used to determine the vertex angles of the electron track at the vertex from the tracking hit position, by reswimming in the solenoid field. Finally a matching hit in the hodoscope planes was requested to ensure the particle to be an electron. The exclusivity of the reaction was tested by determining the missing mass of the detected electron and pions. For simplicity, the study was limited to events where the three pions are reconstructed in the CLAS12 forward detector and only one cluster is measured in the FT calorimeter.

Two quantities are relevant for this study:

- **Acceptance**

The acceptances as a function of the X meson mass obtained using the fast Monte Carlo and the full GEANT4 simulation based on GEMC and Socrat were compared (Fig. 148). Despite the differences between the two curves, results show that around 2 GeV/c, which is where exotic mesons are predicted, acceptance well above 15% also in the case of the full simulations. The fastMC curve is above the dots obtained with

Gemc+Socrat as the later one is taking into account more realistic resolutions, particle propagation and reconstruction.

- **Missing mass reconstruction**

The missing mass of the detected electron and pions was evaluated for each event assuming a X-meson mass of 2.4 GeV/c. Fig. 149 shows the distribution of  $(M_X - M_N)$ , being  $M_N$  the neutron mass. The resolution determined from a Gaussian fit of the peak is of 31 MeV, which is consistent with the resolution evaluated from the fastMC studies and is considered to be sufficient to distinguish  $3\pi$  events from  $4\pi$  events.

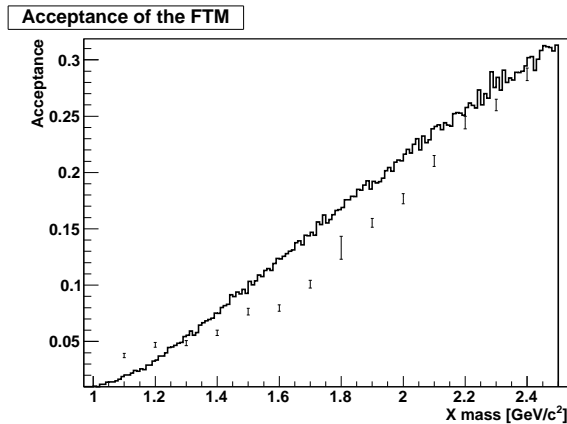


Figure 148: Acceptance for the  $3\pi$  final state obtained with fast Monte Carlo simulations (black curve) and Gemc+Socrat (dots).

In conclusion, the different tests showed the consistency of the results obtained with full GEANT4 simulations with the predictions made from fast Monte Carlo simulations. The study of the  $\gamma p \rightarrow n\pi^+\pi^+\pi^-$  reaction has shown the possibility of reconstructing  $3\pi$  events using CLAS12 software as well as the algorithms specifically developed for the FT. In addition, the momentum and angle resolution of FT and CLAS12 for  $3\pi$  events allows to use the missing mass technique to reduce background coming from other reactions.

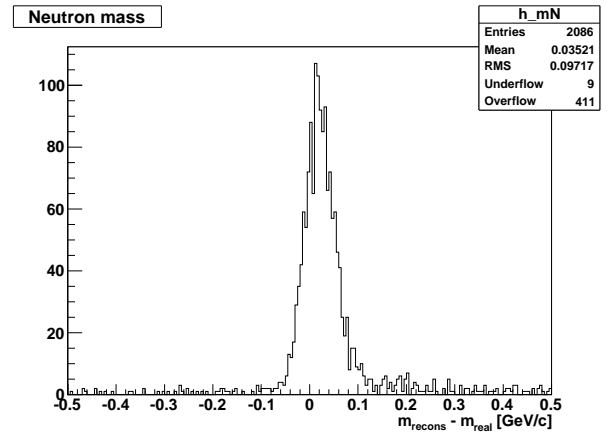


Figure 149: Missing mass spectrum when determined by Gemc+Socrat for a X meson of 2.4 GeV/c.

#### 8.4.1 Conclusions

The results of the study on benchmark reactions presented in the previous sections has clearly shown that the possibility of inferring the energy of the quasi-real photon from measuring the scattered low angle electron gives significant advantages for the study of exclusive multi-particle final states. First of all, the complete determination of the initial state provided by the FT makes it possible to use the missing mass technique to ensure the exclusivity of the reaction. Without such information, a full measurement of the final state particles would be necessary, resulting in acceptances of the order of 1% or below for many of the studied reactions. To fully exploit the missing mass technique, a good energy resolution for the tagger, as planned in the current design, is desirable. In cases where full detection of the final state is possible, the determination of the initial state allows to apply further constraints to suppress backgrounds coming from other reactions and extract small cross section signals.

## References

- [1] K. Nakamura et al. (Particle Data Group), J. Phys. G **37**, 075021 (2010) .
- [2] R. L. Jaffe, K. Johnson, Phys. Lett. **B60**, 201 (1976).
- [3] D. Horn and J. Mandula, Phys. Rev. D **17**, 898 (1978).
- [4] T. Barnes, F. E. Close, F. de Viron and J. Weyers, Nucl. Phys. B **224**, 241 (1983).
- [5] N. Isgur, R. Kokoski, J. E. Paton, Phys. Rev. Lett. **54**, 869 (1985).
- [6] N. Isgur, J. E. Paton, Phys. Rev. **D31**, 2910 (1985).
- [7] P. Guo, A. P. Szczepaniak, G. Galatà, A. Vassallo and E. Santopinto, Phys. Rev. D **78** (2008) 056003.
- [8] J. J. Dudek, R. G. Edwards, M. J. Pearson *et al.*, Phys. Rev. Lett. **103**, 262001 (2009).
- [9] J. J. Dudek, R. G. Edwards, M. J. Pearson *et al.*, Phys. Rev. **D82**, 034508 (2010).
- [10] M. Battaglieri *et al.* [CLAS Collaboration], E12-11-005:*Hadron Spectroscopy with Low  $Q^2$  electron-scattering in CLAS12*.
- [11] A. Afanasev and P. R. Page, Phys. Rev. **A57**, 6771 (1998).
- [12] A. Szczepaniak and M. Swat, Phys. Lett. **B516**, 72 (2001).
- [13] N. Dombey, Rev. Mod. Phys. **41**, 236 (1969).
- [14] M. Atkinson *et al.*, Z. Phys. **C27**, 233 (1985).
- [15] E. S. Ageev *et al.* [COMPASS Collaboration], Phys. Lett. **B**, 633 (2005).
- [16] S. Chekanov *et al.* [ZEUS Collaboration], Nucl. Phys. B **627**, 3 (2002).
- [17] B. Andrieu *et al.*, *Test beam results of the tungsten/quartz-fibre calorimeter for the luminosity measurement in H1, Proc. of the IX Int. Conf. on Calorimetry in Particle Physics*, CALOR2000, Annecy Oct. 2000, Frascati Physics Series (2001).
- [18] M. Atkinson *et al.*, Nucl. Phys. **B231**, 1 (1984).
- [19] B. A. Mecking *et al.* [CLAS Collaboration], Nucl. Instrum. Meth. A **503** (2003) 513.
- [20] CLAS12 Technical Design Report.
- [21] CMS Electromagnetic Calorimeter, <http://cms.web.cern.ch/cms/Detector/ECAL/index.html>.
- [22] D. C. Zhou *et al.* (ALICE Collaboration), J. Phys. G **34** (2007) 719.
- [23] PANDA Collaboration, *Technical Design Report for PANDA Electromagnetic Calorimeter (EMC)*, arXiv:0810.1216.
- [24] I. Bedlinskiy *et al.*, "An Inner Calorimeter for CLAS/DVCS experiments", unpublished.
- [25] S. Janssen *et al.*, Nuclear Science Symposium, 1999 Conference Record, 1999 IEEE
- [26] S.J. Alsvaag *et al.*, IEEE Transactions on Nuclear Science, Vol. 42, no.4 (1995)
- [27] S. Stepanyan *et al.*, CLAS Note 2009-019; S. Stepanyan *et al.*, 2008 IEEE nuclear Science Symposium and Medical imaging Conference.
- [28] I. Akushevich, H. Bottcher and D. Ryckbosch, arXiv:hep-ph/9906408.
- [29] R. Djilkibaev *et al.* 'Lead-Tungstate Scintillator Studies for a Fast Low-Energy Calorimeter' JINST 5 P01003 (2010)
- [30] E. Auffray *et al.*, "Performance of ACCOS, an Automatic Crystal quality Control System for the PWO crystals of the

- CMS calorimeter. NIM A 456 (2011), 325-341
- [31] CMS Collaboration, *The electromagnetic calorimeter technical design report*, CERN/LHCC 97-33, CMT TDR 4, 15/12/1997
- [32] D. Renker, *Status of the avalanche photodiodes for the CMS Electromagnetic Calorimeter*, Annecy, 2000, Prepared for the 9th International Conference on Calorimetry in Particle Physics.
- [33] F. Cavallari, Nucl. Phys. B (Proc. Suppl.) **61B** (1998) 449-455.
- [34] EPICS system: [www.aps.anl.gov/epics](http://www.aps.anl.gov/epics)
- [35] V.A. Batarin, et al., Nucl. Instr. and Meth. A 540 (2005) 131 (e-Print ArXiv physics/0410133).
- [36] V.A. Batarin, et al., Nucl. Instr. and Meth. A 512 (2003) 484 (e-Print ArXiv hep-ex/0210011).
- [37] V.A. Batarin, et al., Nucl. Instr. and Meth. A 550 (2005) 543 (e-Print ArXiv physics/0504085).
- [38] A.M.Blik, et al., Instruments and Experimental techniques, Vol 46, No 6, 2003, pp 753-757.
- [39] M. Ungaro, CLAS12 GEANT-4 simulation package GEMC, [http://clasweb.jlab.org/wiki/index.php/CLAS12\\_Software](http://clasweb.jlab.org/wiki/index.php/CLAS12_Software).
- [40] B. Buonomo, G. Mazzitelli and P. Valente, IEEE Trans. Nucl. Sci. **52** (2005) 824.
- [41] A.D.Bross et al., *Int conf on calorimeter in HEP*, Fermi National Lab, 1990.
- [42] Radiation damage in wavelength shifting Fibres, Atlas internal note, 12 Feb 1998.
- [43] M.J. Varada et al., NIM A **453**225, (2000).
- [44] PEEK specs: TBC.
- [45] M. Sargsyan, CLAS-NOTE 90-007 (1990).
- [46] S. Stepanyan et al., E-07-009: *Meson spectroscopy in the Coherent Production on  $^4\text{He}$  with CLAS*, [http://www.jlab.org/exp\\_prog/proposals/07/PR-07-009.pdf](http://www.jlab.org/exp_prog/proposals/07/PR-07-009.pdf).
- [47] M. Mestayer, SLAC Eng.Note 72 (1977).
- [48] The GlueX Collaboration, *The GlueX Experiment in Hall-D*, <http://argus.phys.uregina.ca/cgi-bin/public/DocDB/ShowDocument?docid=1545>; The GlueX Collaboration, *Mapping the Spectrum of Light Quark Mesons and Gluonic Excitations with Linearly Polarized Photons*, <http://argus.phys.uregina.ca/cgi-bin/public/DocDB/ShowDocument?docid=1226>.
- [49] Y.S. Tsai, Rev. Mod. Phys. **46**, 815 (1974).
- [50] HPS Collaboration, *A Proposal to Search for Massive Photons at Jefferson Laboratory*, 1/12/2010.
- [51] HPS Collaboration, *Trigger Application for the Heavy Photon Search Test Run*, 6/2/2012.
- [52] JLab Fast Electronics Group, *Firmware for FADC250 Ver2 ADC FPGA*
- [53] A. Vlassov, *private communication*.
- [54] M. Mestayer, *private communication*.
- [55] S. Procureur, *private communication*. See also [http://www.jlab.org/~procureur/CLAS12/2008-10-30\\_CollabMeeting.ppt](http://www.jlab.org/~procureur/CLAS12/2008-10-30_CollabMeeting.ppt)
- [56] V. Kubarovsky,  *$\phi\pi$  Photoproduction and Search for Exotic Meson with CLAS*, CLAS-ANALYSIS Note 2000-001.
- [57] S. Procureur, *private communication*.